μSR and Susceptibility Studies of the Normal State of Unconventional Superconductors

μSR and Susceptibility Studies of the Normal State of Unconventional Superconductors

By

Gregory John MacDougall, B.Sc.

A Thesis

Submitted to the School of Graduate Studies

in Partial Fulfilment of the Requirements

for the Degree

Doctor of Philosophy of Science

McMaster University

DOCTOR OF PHILOSOPHY OF SCIENCE (2008) McMaster University

(Department of Physics and Astronomy) Hamilton, Ontario

TITLE: μSR and Susceptibility Studies of the Normal State of Unconventional Superconductors

AUTHOR: Gregory MacDougall, B.Sc.

SUPERVISOR: Graeme M. Luke

NUMBER OF PAGES: xx, 156

Abstract

The following treatise is a collection of three experimental reports, detailing measurements made over the last several years on the magnetic properties of specific correlated electron systems. Each of these systems is an unconventional superconductor at low temperatures, but in each the metallic state from which the superconductivity condenses is poorly understood. The experiments presented will focus on temperatures greater than the superconducting transition temperature, and in particular on magnetic properties of the normal state, which are thought to be important.

Original work is contained in Chapters 3, 4 and 5.

Chapter 3 describes our search for the presence of time-reversal symmetry breaking in the pseudo-gap state of $La_{2-x}Sr_xCuO_4$ with zero-field μSR, and is largely based on previously published data. Additional data on the related systems $La_{1.875}Ba_{0.125}CuO_4$ and $HgBa_2CuO_{4+\delta}$ are also presented. Based on this data, we put strict upper limits on any time-reversal symmetry breaking field which can be associated with the pseudo-gap, and show that the current interpretation of recent neutron scattering results in the literature cannot be correct.

Chapter 4 summarizes our explorations of overdoped $La_{2-x}Sr_xCuO_4$ in applied magnetic field with transverse-field μSR. We see an unconventional broadening of the local magnetic field distribution in response to applied field, and discuss possible interpretations. This chapter has also been prepared for publication.

Chapter 5 describes measurements of the non-linear magnetic susceptibility of URu_2Si_2 as a function of temperature and hydrostatic pressure. By examining the temperature dependence, we draw conclusions about the existence of the anti-ferromagnetism and 'hidden order' at each pressure, and construct a preliminary pressure-temperature phase diagram.

Acknowledgements

Many individuals have contributed my success, and I would be remiss if I did not take a moment to thank them.

Graeme Luke has not only been my supervisor, but also a mentor and friend. I am greatly indebted to him for his continual guidance on both a professional and personal level. I continue to think of his example as I strive to be a better scientist, husband, father and person. Likewise, I am appreciative of Sally, Nigel and Philip Luke for opening their home and hearts to me and my family on more than one occasion, and providing support during times of great uncertainty in our lives.

On the beamline, I benefited from not only Graeme's guidance, but that of Tomo Uemura, who taught and advised me as though I were his own student. His knowledge of and passion for science never ceased to amaze me. Back at McMaster, I was fortunate to have the counsel of Bruce Gaulin, Takashi Imai, Hanna Dabkowska and Anton Dabkowski at various times over the years.

Of course, as much was learned from my peers through discussions, debates and fist-shaking rants during various experiments. For this, and for making long shifts and strange hours more tolerable, I thank Chris Wiebe, Peter Russo, Andrei Savici, Jose Rodriguez, Adam Aczel, Jeremy Carlo and Travis Williams. In addition, these individuals and grad students John-Paul Castellan, Pat Clancy, Jacob Ruff, Andrew Jelovic and Kate Ross have alternately provided me with focus and distraction over the years, creating a culture which has defined graduate school for me more than anything else. May the spirit of Smashie live on.

My parents, Robert and Carol MacDougall, have instilled in me a desire to learn and ability to think for myself. They and my entire family have been more than

supportive of my wildly impractical academic pursuits, and I consider myself lucky to have them in my life.

My greatest and most heartfelt thanks go to my wife and daughter. Heather, my gorgeous and loving wife, has my enduring gratitude for keeping me sane. Her love and support have been a source of constant strength; without her, I would have long ago gone into a self-destructive tailspin. My daughter, Gwendolyn, gave me perspective which I didn't know I was missing, and has become my largest motivation to succeed. I love you both.

Co-Authorship

All of the projects discussed in this thesis are collaborative efforts.

In Chapters 3 and 4, measurements were performed on single crystals of $La_{2-x}Sr_xCuO_4$, which were grown by S. Wakimoto at the University of Toronto and T. Ito at AIST in Tsukuba, Japan. Chapter 3 also contains data on crystals of $HgBa_2CuO_{4+\delta}$ and $La_{2-x}Ba_xCuO_4$, which were grown by the group of M. Greven at Stanford University and G. Gu of Brookhaven National Laboratories, respectively. Sample alignment and characterization were performed by the respective sample growers.

μSR experiments were performed at TRIUMF in Vancouver, BC by the research groups of Y.J. Uemura and G.M. Luke, over a period of four years. Participants include A.A. Aczel, S.-J. Kim, J. Rodriguez, C.R. Wiebe, G.M. Luke, J.P. Carlo, P.L. Russo, A.T. Savici, Y.J. Uemura, and myself. SQUID magnetization data in Chapter 4 was taken at McMaster University by myself.

The crystal in Chapter 5 was grown by J.D. Garrett, and aligned and cut by me. SQUID magnetization measurements in this chapter were performed at McMaster University mostly by myself. Measurements that required the use of a high-pressure piston clamp cell were performed with the assistance of T. Goko of TRIUMF.

All of the data analysis, simulations and writing herein is the result of my own work, performed under the guidance of G.M. Luke.

For Heather and Gwendolyn

Table of Contents

List of Figures

List of Tables

Chapter 1

Introduction to the Materials

1.1 Outline of the Thesis

Superconductors form a class of materials which have been a subject of intense study for the last 100 years, due to their counter-intuitive properties and their potential for technological applications[22]. In the last 30 years, much of this research has revolved around forms of superconductivity which deviate from the microscopic picture put forth by Bardeen, Cooper and Schrieffer[23], where electrons form zero angular momentum pairs through a retarded phonon interaction. In particular, there has been a concentrated effort to understand superconductors with unconventional pairing mechanisms, co-existing magnetic order and high transition temperatures. Two of the largest classes of materials in this regard are the heavy fermion superconductors, discovered in 1979[24], and the cuprate superconductors, discovered in 1986[25].

Unfortunately, in each case, deep understanding of the superconducting state has been hampered by a poor understanding of the high temperature metallic state. The heavy fermion materials are characterized by strong hy-

bridization between local f-electrons and a Fermi sea of s-electrons with highly renormalized carrier masses. The cuprates are characterized by strong electron-electron repulsion, which results in highly correlated behaviour. In both groups, magnetism is thought to play a major role in determining material properties, perhaps facilitating superconductivity itself by acting as a "glue" which binds charge carriers.

The following thesis comprises three separate studies of magnetism in the metallic state of unconventional superconductors. Chapter 3 describes a search for time-reversal symmetry breaking in the so-called pseudo-gap state of the cuprate systems, $La_{2-x}Sr_xCuO_4$, $La_{1.875}Ba_{0.125}CuO_4$ and $HgBa_2CuO_{4+\delta}$ with muon spin rotation (μSR). Chapter 4 describes a study of the local magnetic field response of overdoped $La_{2-x}Sr_xCuO_4$, and conclusions drawn thereof. Chapter 5 describes a study of the linear and non-linear magnetic susceptibility of the heavy fermion superconductor, URu_2Si_2, as a function of hydrostatic pressure. Chapter 1 sets the context of these experiments by providing a very brief description of classical metals and superconductors, and contrasts this with a select review of the cuprates and URu_2Si_2, placing particular emphasis on the problems which I will be discussing in later chapters. Chapter 2 provides a concise description of the experimental methods and apparatus that I used in these studies.

1.2 Conventional Superconductivity

A superconductor is a material which undergoes a phase transition at some critical temperature, T_c, to a state which has zero resistivity and perfect dia-

magnetism. Discovered in 1911 in elemental mercury[26], a comprehensive microscopic theory did not emerge until the mid-1950's, with the work of Bardeen, Cooper and Schrieffer (BCS)[27, 23]. Conventional superconductors are those materials which are well-described by this work, and the closely related work that followed in the ensuing decade.

BCS showed that a free-electron metal is unstable against an arbitrarily weak attractive interaction between charge carriers. As a result, carriers form bound pairs, known as Cooper pairs[27], and condense into a coherent ground state. Perfect conductivity and diamagnetism are a direct result of this coherent state. BCS theory also predicts a gap in the low-lying single-particle excitation spectrum, which they showed is related to T_c through

$$\Delta(T = 0K) = 1.76 k_B T_c, \tag{1.1}$$

where k_B is Boltzmann's constant. This gap corresponds to the energy required to break a Cooper pair, and results in an exponential suppression of thermodynamic quantities at temperatures below T_c. In the original form of the theory, the pairs have zero angular momentum, and the gap is isotropic in **k**-space. In analogy to atomic orbital theory, this is referred to as 's-wave' superconductivity.

The origin of the attractive interaction was suggested by BCS to be the result of a virtual phonon exchange between electrons, as was implied by the observation that T_c varies with the isotope mass[28, 29]. This was later put on more solid footing by the work of Eliashberg[30], and was quickly accepted to be correct.

Careful consideration of BCS and Eliashberg theories led to a stunning agreement between theory and experiment for a wide range of superconducting materials. However, there are now many materials which satisfy the definition of superconductivity, but are not well described within this classical picture. The most often cited reasons for declaring a superconductor 'unconventional' are anisotropic gap functions and non-phonon pairing mechanisms. The most well-known examples of each are the high-temperature cuprates superconductors and the heavy fermion superconductors.

1.3 Conventional Metals

The standard theory for describing metals is Landau's Fermi liquid theory[31, 32, 33]. Developed in the 1950's as a phenomenological description of particle-particle interactions in ^{3}He, it was later generalized to interacting electrons[34, 35, 36], and found to apply to a wide range of metallic systems.

Landau considered a group of interacting electrons and compared it to the non-interacting case. He argued through phase space considerations that it is consistent to treat arbitrarily strong particle-particle interactions perturbatively, as long as the final state is adiabatically connected to the non-interacting system. He showed in this case that there is a one-to-one mapping near the Fermi surface between the energy levels of the interacting and free electron systems. Thus, the low-temperature properties of the interacting system are determined by single-particle, fermionic excitations, just as in the free electron case. That is, he showed that, often, *electron-electron interactions do not fundamentally alter the microscopic picture in metals.* The main caveat

is that the fermionic excitations are no longer those of electrons, but rather of composite objects called 'quasi-particles', which can roughly be pictured as free particles combined with the 'wake' they cause by motorboating through an interacting Fermi sea.

As a result of this analysis, many of the formulas derived for free electrons at low temperatures remain valid, with only slight modifications to account for renormalized particle masses and moments:

$$C_V = \frac{1}{3}\pi^2 D(\epsilon_F) k_B^2 T \propto T \tag{1.2}$$

$$\rho = \frac{m^*}{ne^2\tau} \propto T^2 \tag{1.3}$$

$$\kappa = \frac{\pi^2 n k_B^2 \tau T}{3m^*} \propto T \tag{1.4}$$

$$R_H = -\frac{1}{ne} = \text{const} \tag{1.5}$$

$$\chi = g^{*2}\mu_B^2 D(\epsilon_F) = \text{const} \tag{1.6}$$

In the above equations, $C_V, \rho, \kappa, R_H \text{and} \chi$ denote specific heat, resistivity, thermal conductivity, Hall coefficient and magnetic susceptibility, respectively. $D(\epsilon_F)$ is the density-of-states at the Fermi energy, n is the carrier density, and m^*, g^* and τ denote the effective mass, effective moment and scattering lifetime of the quasi-particles.

The temperature dependences seen in Eq. 1.2-1.6 are considered the hallmarks of a Fermi-liquid, and 'non-Fermi-liquid' behaviour is often defined as a violation of these equations.

Combining Eq. 1.3 and Eq. 1.4 gives

$$\frac{\kappa\rho}{T} = \frac{\pi^2}{3}(\frac{k_B}{e})^2 = 2.45 \times 10^{-8} W \cdot \Omega / K^2, \tag{1.7}$$

which is known as the Weidemann-Franz equation. This equation reflects the fact that the low-lying excitations which carry heat are associated with charge-carrying particles, and is considered a test of Fermi-liquid theory in its own right.

A central feature of Fermi liquid theory is that it works for *arbitrarily strong* particle-particle interactions, as long as the system is adiabatically connected to the free electron ground state. Thus, violations of the above equations evince a *fundamentally new* ground state, and likely indicate that interesting physics is at play. Examples include superconductivity and charge density-wave order, both of which are understood in terms of Fermi surface instabilities. A localization transition due to strong electron-electron repulsion is central to Mott insulating physics[37], which is very pertinent to the cuprates. Non-Fermi-liquid behaviour is also one of the key predictions of quantum critical theory, and is often taken as the first indication that a system is in proximity to a quantum critical point[38]. This idea pervades cuprate and heavy fermion research.

1.4 The Cuprates

1.4.1 Phenomenology

The cuprate superconductors were discovered by Bednorz and Muller in 1986 as part of a concentrated effort to explore the low temperature properties of transition metal oxides with perovskite structures[25]. Before this time, the record for the highest superconducting transition temperature was held by Nb_3Ge at T_c=23.3K[39, 40]. This record was broken when Bednorz and Muller discovered superconductivity in powders of $La_{2-x}Ba_xCuO_4$ with T_c=35K.

This discovery was followed quickly by the discovery of several related superconductors with even higher transition temperatures, up to the current record of 138K[41]. This kick-started a major movement in the condensed matter community to understand transition metal oxides and, more generally, correlated electron systems. Bednorz and Muller won the Nobel Prize for their efforts in 1987.

Fig. 1.1 shows the crystal structures for three well-known families of cuprate superconductors. Central to all of these structures (and every cuprate superconductor) are quasi-two-dimensional planes of copper and oxygen, sketched in Fig. 1.2. Though band theory predicts that these materials should be metals[42], strong electron-electron repulsion localizes the electrons on the copper site, creating a Mott insulator[37]. A second order virtual hopping term in the Hamiltonian favours antiferromagnetic exchange[43], and long range antiferromagnetic order is observed[44]. This is indicated by the arrows in Fig. 1.2. When a hole is introduced into the planes by cation or oxygen doping, it occu-

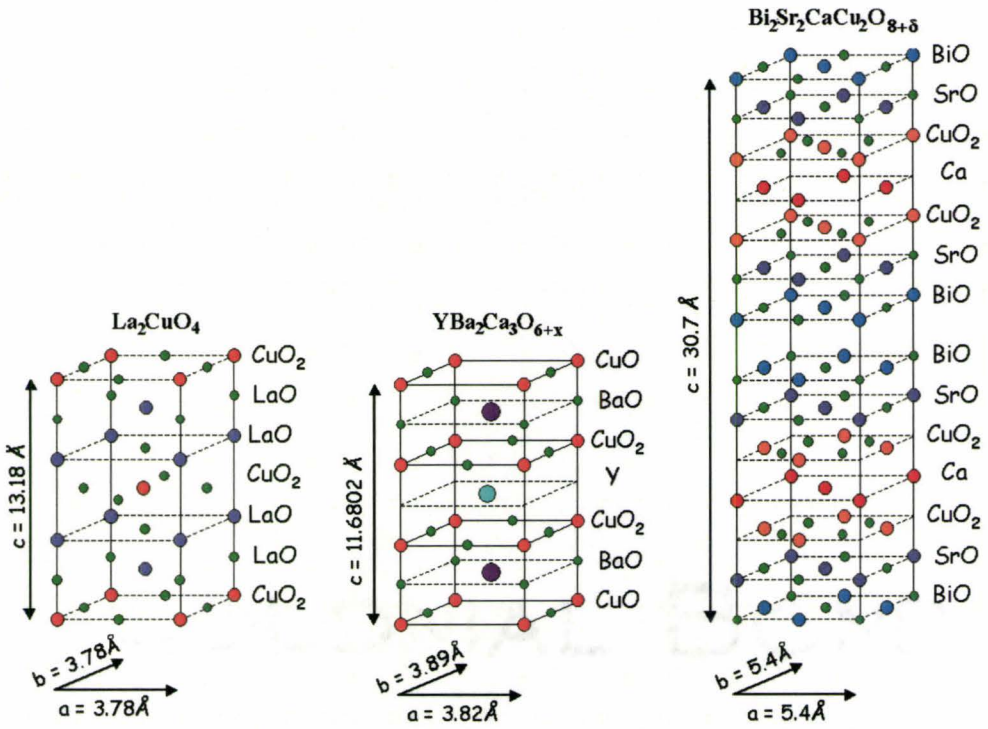

Figure 1.1: Crystal structures for three of the most widely studied cuprate systems. Courtesy of J.E. Hoffman.

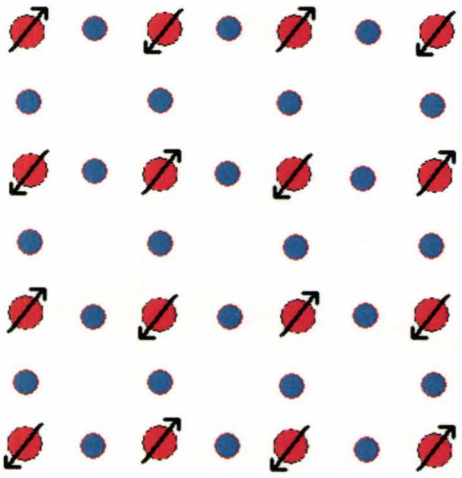

Figure 1.2: A cartoon of the copper-oxide planes in the cuprates. Copper is shown in red, and oxygen in blue. Arrows indicate the orientation of the copper spins in the parent antiferromagnetic state.

pies a singlet band formed by the hybridization of the O $2p_x$ and $2p_y$ orbitals with the Cu $3d_{x^2-y^2}$ orbital, and simulates the removal of a spin from a copper site[45].

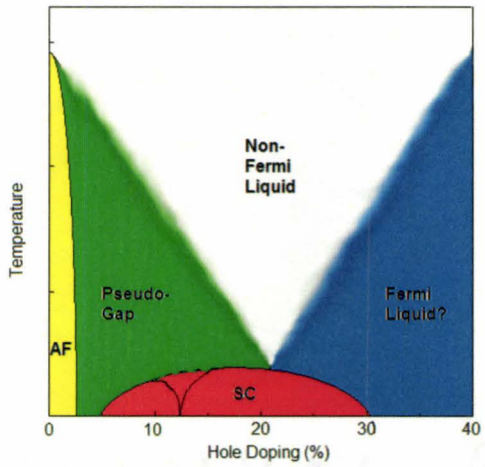

Figure 1.3: The generic phase diagram for the high-temperature cuprate superconductors.

The phenomenology of the cuprates is reviewed in many places[46, 1, 47]. In Fig. 1.3, I have drawn a version of the standard cuprate phase diagram, based on $La_{2-x}(Sr, Ba)_xCuO_4$, with carrier concentration on the x-axis and temperature on the y-axis. As holes are added, the parent antiferromagnetism is quickly destroyed, and the system eventually enters an unconventional superconducting state at low temperatures. The superconducting transition temperature, T_c, reaches a maximum near x=0.15, which is referred to as 'optimal doping'. Regions to the left and right of optimal doping are referred to as the 'underdoped' and 'overdoped' portions of the phase diagram, respectively.

The state from which superconductivity condenses at optimal doping has several properties which contradict conventional Fermi-liquid theory, and is

alternately referred to as a 'strange metal', a 'marginal Fermi-liquid', or simply a 'non-Fermi-liquid'. The most commonly cited examples of non-Fermi-liquid behaviour are the linear temperature dependence of resistivity and the temperature-dependent Hall coefficient[48, 49, 50], although magnetic properties are also unusual[51].

As one approaches the Mott insulating parent compound from the strange metal state, correlation effects manifest themselves more strongly, and one enters the so-called 'pseudo-gap' state. Experimental studies of the pseudo-gap are extensive and interpretations are contentious. This subject is discussed in more detail in Section 1.4.3, and our experimental results in this region of the phase diagram are presented in Chapter 3.

On the overdoped side of the phase diagram, it is widely believed that the cuprates act more like conventional Fermi-liquid metals. Although there is some evidence to support this point of view, there has been a general paucity of studies on overdoped materials due to the absence of high-quality crystals. The overdoped cuprates are discussed in more detail in Section 1.4.4, and our experimental results in this region of the phase diagram are presented in Chapter 4.

There now exist dozens of known cuprate families. However, due to various factors, a handful are more widely studied than the rest. In this manuscript, discussion will be limited to the monolayer compounds $La_{2-x}Sr_xCuO_4$ (LSCO), $La_{2-x}Ba_xCuO_4$ (LBCO), $HgBa_2CuO_{4+\delta}$ (Hg-1201) and $Tl_2Ba_2CuO_{6+\delta}$ (Tl-1201) and the bi-layer compounds $YBa_2Cu_3O_{6+x}$ (YBCO) and $Bi_2Sr_2CaCu_2O_{8+\delta}$ (Bi-2212).

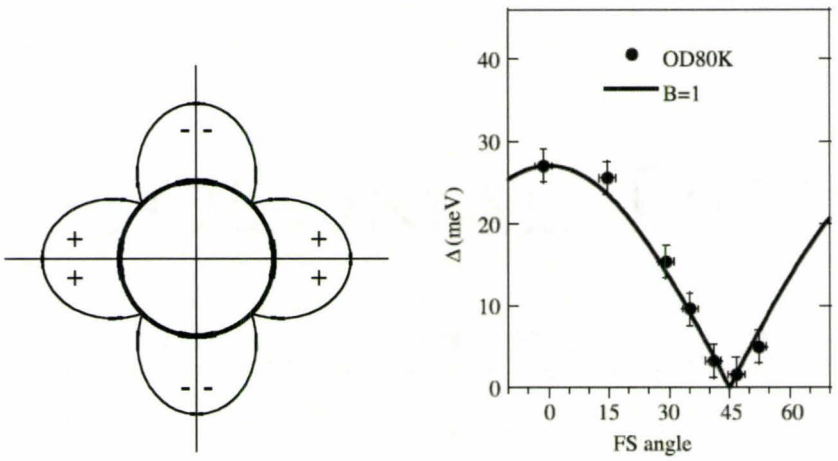

(a) (b)

Figure 1.4: (a)Sketch of a d-wave superconducting gap on a circular Fermi surface. (b)The angular dependence of the gap in Bi-2212 by ARPES. From [1].

1.4.2 Superconductivity

Central to the cuprates, and the driving factor behind the initial research on these compounds, is the high-T_c superconductivity which exists at moderate dopings. Although many aspects of the superconducting state can be described by a modified form of BCS theory[46], there are also several unconventional features of note.

The first and most remarkable feature is the anisotropy of the superconducting gap. In contrast to the isotropic s-wave gap originally predicted by BCS, pairing in the cuprates has a 'd-wave' gap, given by

$$\Delta(\mathbf{k}) = \Delta_0[\cos(k_x) - \cos(k_y)], \tag{1.8}$$

where $\mathbf{k}$ denotes wavevector. A gap of this kind has two line nodes, and thus low-lying quasi-particle excitations. This pairing function was predicted by several early theories of the cuprates[52, 53, 54, 55], and the existence

of low-lying quasi-particles was famously confirmed by penetration depth[56] and nuclear magnetic resonance (NMR) spin-lattice relaxation rate[57] measurements. The correct angular dependence of the gap was soon verified by angle-resolved photo-emission spectroscopy (ARPES)[58, 59, 60, 61], and phase sensitive tunneling experiments definitively settled the debate shortly thereafter[62, 63, 64]. Fig. 1.4 shows a sketch of a d-wave gap on a circular Fermi surface and the angular dependence of the actual gap as measured by ARPES.

Secondly, upper critical field measurements[65] imply unusually small superconducting coherence lengths- on the order of 10-30Å rather than 100-1000Å for the elemental superconductors. This can be interpreted as a decreased 'size' of Cooper pairs in the superfluid, and this idea has been discussed extensively in the context of BEC-BCS crossover[66]. More generally though, this means that the superconducting order parameter can change dramatically over lengthscales of a few unit cells, and these systems lend themselves naturally to atomic-scale heterogeneity. Heterogeneity in the cuprates is discussed further in Chapter 4.

Also of note is the magnitude of the transition temperatures themselves. At the time of the cuprates' discovery, it was conventional wisdom that the phonon mechanism for mediating superconductivity could create T_c's no higher than $30K$[67]. Although this belief was called into question with the discovery of superconductivity in MgB_2, which had a T_c of $39K$[68], it is still generally believed that a novel pairing mechanism is needed to explain T_c's on the order of $100K$ or higher, as seen in many cuprate systems. Fueling debate about the

pairing mechanism in these materials is the linear variation of T_c with both superfluid density[69] and the commensurability of magnetic fluctuations[70], known as the Uemura and Yamada relations, respectively. Magnetism, and in particular stripe order[71], is strongly suspected as a possible pairing mechanism. However, it is generally agreed that this debate can only be settled once a comprehensive theory of the normal state is formed.

1.4.3 Underdoped Studies and the Pseudo-Gap

The majority of studies on the cuprates have concentrated on the properties of the underdoped materials, and have been discussed in terms of a 'pseudo-gap'. Pseudo-gap is a term that has been coined to describe a collection of experimental anomalies that occur in the underdoped materials below some temperature, $T^* > T_c$[72, 73, 3]. Though strict interpretation of these anomalies is controversial and a matter of intense debate, most can be associated with a suppression in the low-energy quasi-particle density of states, and the term 'pseudo-gap' is designed to emphasize this idea.

Experimentally, the pseudo-gap was first discovered by NMR measurements of YBCO. In 1989, several NMR groups reported a decrease in spin-lattice relaxation rate below T^*[74, 75, 76], implying a suppression of antiferromagnetic fluctuations at low temperatures. Shortly thereafter, a decrease of the spin-susceptibility at comparable temperatures was observed by NMR Knight shift measurements in YBCO[77] and bulk susceptibility measurements in LSCO[51]. Such behaviour is expected from samples undergoing a transition into a superconducting state due to the formation of Cooper pairs, and

the idea of a spin-gap due to (phase-incoherent) pair formation above T_c was put forth immediately[75].

The spin-gap has since been seen in a variety of materials, both from the experiments mentioned above[78, 79, 80, 81, 82, 83, 84, 85, 86, 87, 88, 89, 90, 91] and from neutron scattering, where a suppression of low energy dynamics about the antiferromagnetic zone center is observed in the normal state of underdoped materials[92, 93, 94, 95, 96, 97], but not overdoped materials[98].

The pseudo-gap also affects charge degrees of freedom. Electrical resistivity exhibits a downturn from linear T behaviour at T^* when the current runs parallel to the copper-oxide planes, and a sharp upturn below T^* when the current runs perpendicular to the planes[99, 100, 101, 102, 103, 104, 105, 106, 107, 108]. Consistently, a gap-like suppression is seen in the low frequency $\hat{\mathbf{c}}$-axis optical conductivity[109, 110, 111, 112, 113, 114, 102], whereas planar optical conductivity shows a narrowing of the zero-frequency Drude peak[115, 116, 117, 118, 102, 119]. These observations are most frequently interpreted as a gap in the scattering rate of quasi-particles due to the spin-gap, but also as a true gap in the quasi-particle density-of-states. Delicate specific heat measurements observe a suppression of the quasi-particle contribution in underdoped YBCO, and by comparison to the bulk magnetic susceptibility reveal that the charge and spin density-of-states are equally weighted[120, 121, 122, 123, 124, 125].

A gap in the single-particle spectrum is measured directly by spectroscopic probes. Scanning tunneling spectroscopy (STS) observes a partial suppression of low-lying single-particle excitations below some critical bias voltage

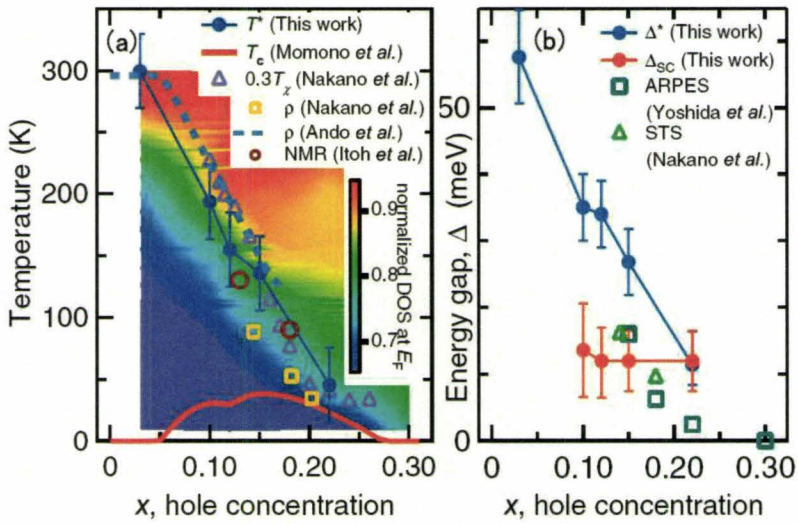

Figure 1.5: Estimates of the pseudo-gap temperature and gap size in LSCO from resistivity, NMR, bulk susceptibility, STS and ARPES. Both T^* and Δ decrease with increasing carrier concentration. From [2].

(representing a gap energy), but without the sharp coherence peaks about the critical voltage that are seen in superconductors[126, 127, 128, 129, 130]. Interestingly, where superconductivity is suppressed, pseudo-gap signatures remain and non-dispersive charge order is seen to emerge[131, 132, 133, 134, 135]. Photo-emission spectroscopy also reports a quasi-particle gap above T_c in a variety of materials, which is highly anisotropic and roughly (but not perfectly) reflects the angular dependence of the superconducting gap[136, 137, 138, 139, 140, 141, 142, 143, 144, 145, 146, 147, 2].

Both of these probes (along with optical conductivity) indicate that the magnitude of the quasi-particle gap is temperature independent, with the spectral weight at low energies 'filling in' as T approaches T^* from below, rather than the gap closing. In addition, both probes see the size of the gap sharply increase as the carrier concentration is decreased. All probes generally

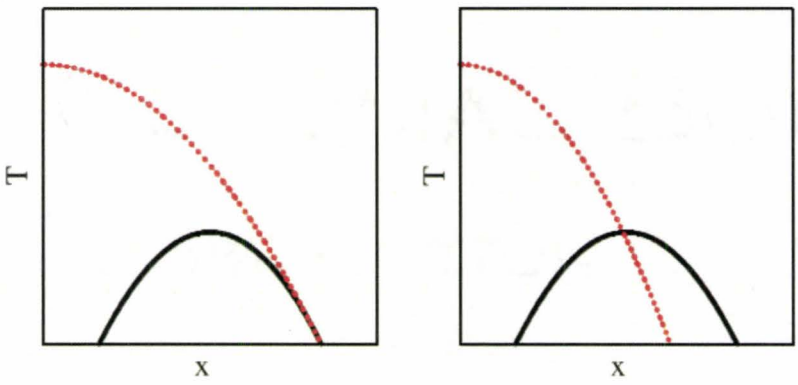

Figure 1.6: (top)A summary on the two most commonly predicted phase diagrams for the cuprates. From [3].

agree that T^* increases with decreasing doping as well, consistent with the standard phase diagram presented in Fig. 1.3, although the details regarding how the line of pseudo-gap transitions intersects the superconducting dome are still considered controversial. These observations are summarized in Fig. 1.5, taken from Ref. [2], where several experimental estimates of the pseudo-gap temperature and the size of the gap in LSCO are displayed.

Among the many debates surrounding this topic are whether there are one or multiple energy scales associated with the pseudo-gap transition, and whether the pseudo-gap and superconducting gaps are distinct. (Fig. 1.5 obviously supports the idea of separate gaps.) More generally, there is no consensus on the microscopic picture that is to be associated with the above experiments, and interpretations widely vary. To date, models of the pseudo-gap have generally predicted one of two cuprate phase diagrams, summarized in Fig. 1.6.

The first and most widely touted phase diagram is that shown in the left panel of Fig. 1.6, where the superconducting dome is entirely contained within

the pseudo-gap state. This picture is predicted by models which consider the pseudo-gap to be a precursor state to the superconductivity at lower temperatures. One example is the 'pre-formed pairs' model, where T^* is the temperature at which Cooper pairs form, but superconductivity is suppressed on the underdoped side of the phase diagram due to a lack of phase coherence[148, 71, 149]. Other examples include spin-charge separation models, where T^* and T_c represent the successive gapping of spin and charge degrees of freedom, respectively[150, 151, 152]. Proponents of these models note the similarities between the superconducting gap and pseudo-gap energies, and point to studies which apparently indicate the merging of the two temperature scales on the overdoped side of the phase diagram.

Supporters of the second phase diagram are themselves separated into two camps. The first camp contends that the pseudo-gap 'transition' is not a transition at all in the thermodynamic sense, but rather represents an energy scale at which a particular term in the Hamiltonian becomes relevant. The prime example of this is the Nearly Antiferromagnetic Fermi Liquid model, where the pseudo-gap represents the energy scale of antiferromagnetic fluctuations, which disappear at a critical point inside the superconducting dome[153, 154, 155, 156, 157, 158]. Proponents of this scenario emphasize that the pseudo-gap always presents itself as a gradual change of local properties rather than a sharp transition, and hold up a number of studies which show pseudo-gap energies apparently going to zero at the same critical doping.

The remaining theories also support the second phase diagram, but treat the pseudo-gap as a real thermodynamic transition into a novel ordered state,

with superconductivity as a direct result of quantum critical fluctuations. The prime example of such models are the current ordering models of Chakravarty[159] and Varma[160, 161, 162, 163, 164], where spontaneous currents flow in set patterns within the copper-oxide planes in the underdoped materials at low temperatures. Proponents point to studies which apparently verify predictions of the theories, such as the appearance of time-reversal symmetry breaking at T^*. Chapter 3 of this thesis deals specifically with the theory of Varma, and an expanded discussion of this topic is presented at the beginning of that chapter.

1.4.4 Overdoped Studies

In virtually every theory of the pseudo-gap, the unconventional properties are either a direct or indirect by-product of proximity to the parent Mott-insulating state. As such, it is reasonable to expect that as one dopes into the overdoped region of the phase diagram, Mott physics will be less important and the cuprates will act as canonical Fermi-liquids. This is the view taken by most of the community. Yet, large single crystals in this doping range have only emerged in recent years[165, 166], and virtually all studies of these samples range show some form of unconventional behaviour.

Evidence for Fermi-liquid behaviour comes mostly from transport measurements. Several groups have noted an evolution of the temperature dependence of resistivity from linear to super-linear as one dopes above optimal doping[4, 167, 168, 169, 170, 171], although only one study has reported the expected T^2 dependence (Eq. 1.3)[172]. Thermal conductivity measurements[170, 172] obey the Wiedemann-Franz law (Eq. 1.7), and verify

the BCS prediction for T_c (Eq.1.1). ARPES notes the emergence of a quasiparticle coherence peak in the photo-current[173, 174], and angular magnetoresistance oscillations have been observed in one compound[175], which implies the existence of a Fermi surface.

It has been noted[176], however, that even strong interactions cannot explain a deviation from T^2 resistivity from a Fermi liquid perspective, and in the one system where T^2 resistivity has been observed[172], the coefficient of the quadratic term shows an unusual enhancement when compared to the linear term in the heat capacity. Moreover, the optical conductivity has unusual frequency dependence[99, 114], and the Hall constant is seen to be temperature dependent[177, 169, 178, 179] and of the wrong sign to be compatible with ARPES results[144].

Magnetic properties are more overtly non-Fermi-liquid-like. In contrast to temperature independent Pauli paramagnetism (Eq. 1.6), bulk susceptibility measurements on overdoped powders routinely reveal the existence of a Curie-like term, leading many to infer local moment formation[4, 180, 90, 181, 19]. This is shown in Fig. 1.7(a) for several samples of naturally overdoped Tl-2201. In LSCO, the doping evolution of this term has been carefully investigated, and it is seen to emerge gradually from slight overdoping[180, 90, 19]. This indicates that the Curie-like susceptibility is intrinsic rather than extrinsic in origin.

In the superconducting state, μSR sees a decrease in superfluid density with increased carrier concentration, contrary to expectations[5, 182, 183]. Similarly, low-field bulk susceptibility sees a shrinking Meissner fraction with in-

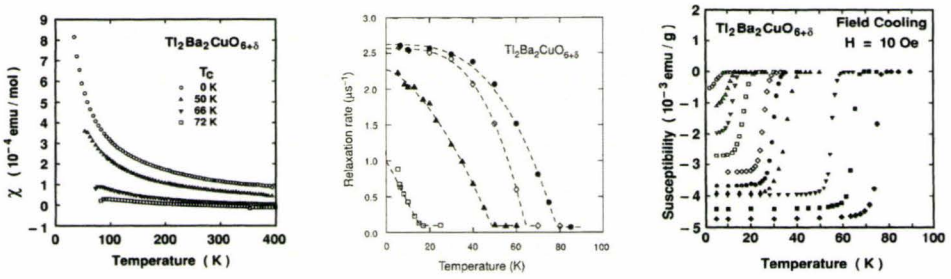

(a) (b) (c)

Figure 1.7: Various experimental data on naturally overdoped Tl-2201 as a function of doping, including (a)the emergence of a Curie term in the bulk susceptibility[4], (b)the decrease in superfluid density[5] and (c)the shrinking Meissner fraction[4].

creased doping[4, 184]. These results have been taken as evidence for real space phase separation into superconducting and non-superconducting regions[5, 185, 186]. Subsequent optical conductivity[187, 114], magnetization[188], and neutron scattering[165, 19] studies have come to the same conclusion through indirect arguments. Specific heat measurements on LSCO reveal a linear temperature term which grows with doping[65], and have been interpreted as direct evidence for substantial numbers of unpaired charge carriers co-existing with superconductivity.

At the very least, these features imply extensive heterogeneity in the overdoped region, and, in combination with the Curie-like magnetization and various theoretical considerations, have even lead some theorists to postulate a first-order quantum phase transition to a ferromagnetic ground state on the overdoped edge of the superconducting dome[176]. Chapter 4 probes the magnetic properties of overdoped LSCO approaching this putative quantum crit-

ical point, and comments specifically on the presence of heterogeneity in this region of the phase diagram.

1.5 URu_2Si_2

1.5.1 Introduction to Heavy Fermions

The heavy fermions are metals characterized by quasi-particle effective masses which are as much as 1000 times larger than the bare electron mass. Though there are notable exceptions[189], most are intermetallics which contain both localized 4f or 5f-electron orbitals and delocalized (s/p)-electron orbitals at the Fermi energy. The physics of these systems is largely set by a complex coupling between the two bands, and is reviewed in many places[190, 191, 192, 193]. The largest effect of this inter-band coupling is the Kondo-like screening of the f-electron moments by the conduction electrons at temperatures below a coherence temperature, T_0.

In addition to enhanced quasi-particle masses, heavy fermion metals and related compounds regularly display non-Fermi-liquid behaviour[194, 195, 196]. As with the cuprates, this behaviour is often attributed to a nearby magnetically ordered state (and thus a QCP), and is discussed in terms of a poorly-understood competition between Kondo-like screening of local moments and itinerant electron mediated (i.e. RKKY) exchange interactions[197, 198, 199]. Indeed, many heavy fermion compounds are seen to order at low temperatures,

often with strongly renormalized moments ($<0.1\mu_B$)[200, 201, 202, 203, 204] and unusual magnetic correlations at finite $\mathbf{q}$[202, 205, 203, 206, 207].

The original impetus for this field was the discovery of superconductivity in $CeCu_2Si_2$[24], which was followed quickly by that in UBe_{13}[208] and UPt_3[209]. The strong role of magnetism in these systems raised the likelihood of an unconventional pairing mechanism. Since then, multiple heavy fermion materials have revealed signatures of unconventional superconductivity, including multiple superconducting phase transitions[210, 211, 212, 213], time-reversal-symmetry-breaking[214, 215, 216] and power-law temperature dependences of various thermodynamic quantities[217, 218, 219, 220, 212]. The interplay between superconductivity and magnetic order is complex and has been studied extensively[221].

1.5.2 URu_2Si_2 and Hidden Order

URu_2Si_2 is a moderately heavy fermion metal, with $T_0 \sim 80K$ and $m^* \sim 50m_e$. Its crystal structure is tetragonal, and shown in Fig. 1.8. As with other heavy fermion materials, large paramagnetic moments are seen at high temperatures, and are screened below T_0. At the same temperature, a large linear term in the specific heat develops. URu_2Si_2 first attracted attention when it was suggested that the superconducting ground state (T_c=1.5K) co-existed with long-range antiferromagnetism, and thus might be unconventional[222]. The superconducting state indeed has many unconventional properties[223], but the majority of studies have instead focussed on the metallic state from

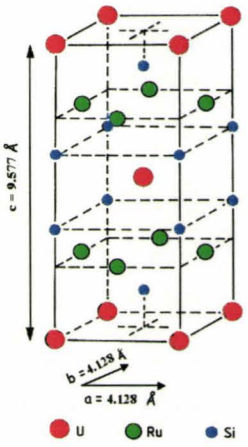

Figure 1.8: The unit cell of URu_2Si_2, adapted from [6].

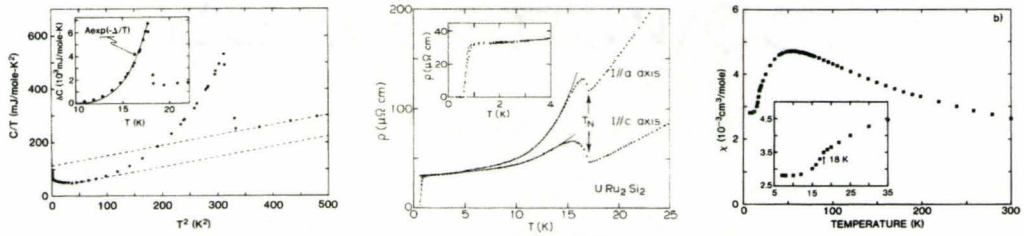

(a) (b) (c)

Figure 1.9: Anomalies associated with the hidden order state in URu_2Si_2 from (a)specific heat[7], (b)resistivity[8], and (c)magnetic susceptibility[7].

which superconductivity condenses - what is now referred to as the 'hidden order' state.

The origin of this term lies in the second order phase transition at $T_{H.O.}$=17.5K, as revealed by a large lambda-like anomaly in the specific heat[224, 222, 7]. Associated with this transition are anomalies in resisitivity[8, 7], thermal expansion[225], thermal conductivity[226, 227] and both linear[224, 7] and non-linear[228, 21] magnetic susceptibility. Some of these results are shown in Fig. 1.9.

This transition was originally thought to be associated with collinear antiferromagnetic order[222], but subsequent neutron[202, 203, 6] and magnetic X-ray[229] scattering experiments measured a local moment of 0.02-0.04μ_B, which is over an order of magnitude too small to explain the specific heat anomaly[230]. Thus, the antiferromagnetism is now considered to be secondary to a yet unknown primary order parameter.

In the years since, there have been dozens of studies, both experimental and theoretical, which have attempted to determine the nature of this hidden order state. At this point, very little has been settled. However, it is very likely that the hidden order parameter is associated with some form of magnetism. Both NMR[231] and μSR[232] have reported an order-parameter-like increase in inhomogeneous relaxation rate below $T_{H.O.}$, which is isotropic and too small to be associated with antiferromagnetic moments. Neutron scattering reveals that the magnetic excitation spectrum becomes gapped at finite, incommensurate wavevectors at $T_{H.O.}$[233, 203, 234, 235], and a recent report shows that the gapping of these excitations is sufficient to explain the specific heat anomaly[235].

Theoretical proposals for the order parameter are numerous, and include spin nematics[236], orbital antiferromagnetism[237, 238], helicity order[163], quadrupolar order[239, 240, 241], octupolar order[242], triplet spin correlators[243, 244] and various forms of spin-density wave or antiferromagnetism with highly renormalized g-factors[245, 246, 247, 248]. There is no experimental evidence to definitively support any one of these proposals.

1.5.3 Applied Pressure and Antiferromagnetism

Part of the effort to understand the hidden order state is to determine its relation to the secondary antiferromagnetism. This effort, as explained below, is intricately tied to a proper determination of the pressure-temperature phase diagram.

URu_2Si_2 undergoes a first order phase transition with pressure to a collinear antiferromagetic state, which has the same symmetry as the small moment antiferromagnetism (SMAF), but a $0.3\mu_B$ moment. The transition was first observed by neutron scattering as a rapid increase in scattering intensity at the antiferromagnetic zone centre[249]. NMR[250, 251] and μSR[252, 253, 254] later showed that the increased scattering intensity was due to a rapid increase in the volume occupied by the antiferromagnetic order, without appreciably changing the size of the ordered moment. This naturally led to the interpretation that the SMAF observed in ambient pressure was merely a series of droplets of the high pressure phase in a tiny ($\sim$ 1%) volume[255], perhaps due to internal strain around stacking faults inside the crystal structure. Consistent with this interpretation are the observations that the large moment antiferrogmagnetism (LMAF) is also induced by uniaxial strain[256, 10], and samples mounted in a way that encourages strain show order in a larger volume fraction than others which are not[257, 254].

Detractors of this idea note the long magnetic correlation length reported by X-ray scattering[229] and the qualitatively different temperature dependence of the transitions in the SMAF and LMAF phase[258, 9]. These individuals favour a model where both hidden order and antiferromagnetism

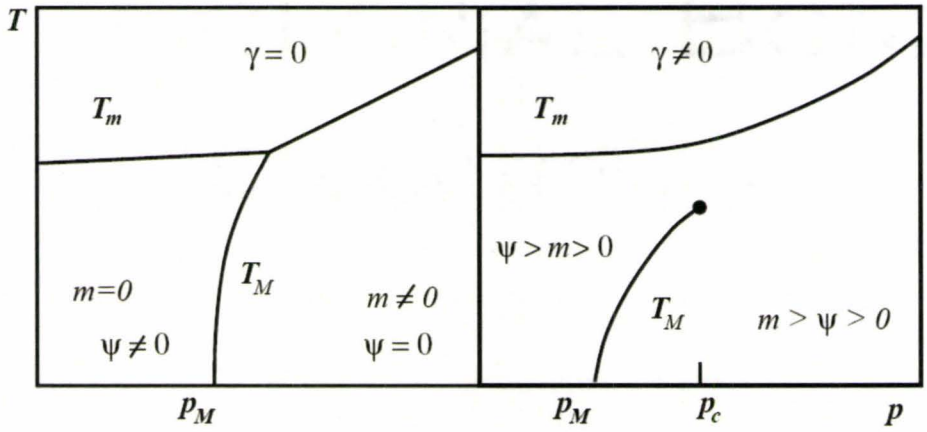

Figure 1.10: Competing P-T phase diagrams derived from Eq. 1.9. From [9].

are homogeneous and co-exist, perhaps with the SMAF being induced by the development of the primary order parameter (See, for example, Ref. [248]).

Both of these scenarios can be described in the context of a phenomenological two order parameter model[259]. In such a model, the free energy is given by

$$F = \alpha_1\psi^2 + \alpha_2 m^2 + 2\gamma\psi m + \beta_1\psi^4 + \beta_2 m^4 + 2\beta_i\psi^2 m^2, \qquad (1.9)$$

where ψ is the hidden order parameter and m is the size of the antiferromagnetic moment. The difference between the two pictures above is the presence or absence of the linear coupling term in Eq. 1.9, which leads to qualitatively different pressure-temperature phase diagrams for the system. This is demonstrated in Fig. 1.10.

In the case where $\gamma = 0$, the two order parameters are mutually exclusive. At lower pressures, the system is entirely in the hidden order state with no (intrinsic) antiferromagnetism. At higher pressures, the system is entirely in the antiferromagnetic state with no hidden order. The line of transitions

between the two states merges with the upper transition line at a bi-critical point. At this bi-critical point, the upper transition exhibits a kink.

If $\gamma \neq 0$, then the line of transitions terminates at a critical end point. The two order parameters co-exist at all pressures, and the SMAF state continuously evolves into the LMAF state as one travels around this end point. In this scenario, Eq. 1.9 also predicts an inflection point in the field dependence of the antiferromagnetic Bragg peak intensity[259].

As the linear coupling term in Eq. 1.9 can only exist for two order parameters which belong to the same irreducible symmetry class, there has been tremendous interest in determining which of the two pictures described above is correct. In particular, if it can be definitively shown that $\gamma \neq 0$, then the viable theories of the hidden order state would be limited to those that break time-reversal symmetry.

A neutron scattering experiment saw the predicted inflection point with field, providing strong evidence that $\gamma \neq 0$[260]. The same group later produced a phase diagram, shown in Fig. 1.11(b), which they claim supports the existence of a critical end point, since the lines of transitions do not merge[258, 9]. On the other hand, phase diagrams from a competing neutron scattering group[256, 261, 10], thermal expansion[262, 263] and local probes[251, 253] seem more reminiscent of $\gamma = 0$. One of these is shown in Fig. 1.11(a). In further support of this picture is the observation of a kink in $T_{H.O.}$(P)[264] from resistivity studies, suggestive of a bi-critical point.

Aside from the fundamental disagreement regarding the critical end point, the above studies have given a rather large range of values (300-700MPa) for

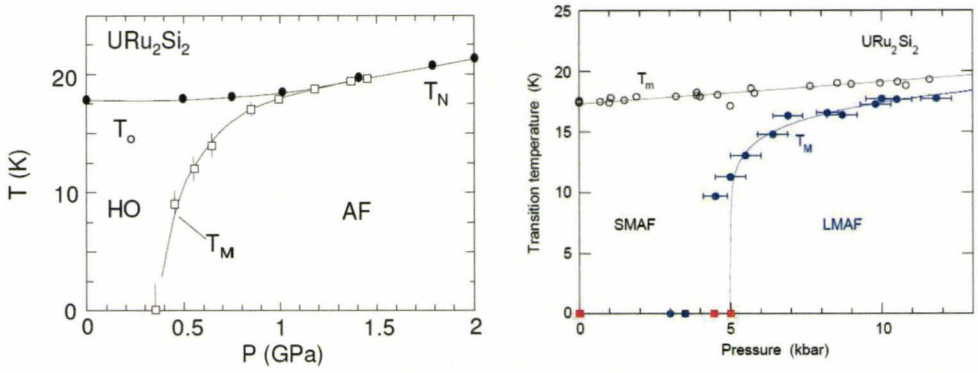

(a) (b)

Figure 1.11: Competing phase diagrams from separate neutron scattering experiments (Refs. [10] and [9], respectively).

the critical pressure. Both sample size[261] and pressure medium[9] have been shown to affect this value, presumably due to the role of uniaxial strain in the large pressure cells typically used for neutron scattering research. It should also be noted that, with the exception of the thermal expansion studies, none of the above studies used a single probe and a single sample to determine the temperatures of the various phase transitions. In Chapter 5, I address these issues by developing a technique to map out the URu_2Si_2 pressure-temperature phase diagram via non-linear susceptibility measurements.

Chapter 2

Experimental Methods

2.1 μSR

2.1.1 Introduction

μSR is any one of a wide variety of experiments which use the parity violating decay of the muon to explore condensed matter systems. This is a broad definition which includes studies of quantum diffusion, chemistry, semiconductor physics and surface physics. However, this thesis will discuss μSR primarily as a tool to study local magnetism.

Depending on the context, μSR can stand for muon spin rotation, relaxation, resonance or research. The acronym is designed to draw attention to the similarities between μSR and other resonance probes, such as NMR and ESR. Like these techniques, μSR is a real-space probe of magnetism, which gains information about the local field environment by monitoring the evolution of probe magnetic moments. Unlike NMR and ESR, which polarize the spins of host atoms with strong magnetic fields, μSR injects spin-polarized muons into

the sample of interest as a *foreign* probe of magnetism. Also, instead of using rf-fields to gather information, a μSR experimenter collects products from the decay of the probe itself.

There are advantages and disadvantages to this technique. The main advantage is the extreme sensitivity of the muon, which regularly detects internal fields weaker than $0.1G$, and has been used to examine crystals as small as 2mm^3. In addition, μSR is sensitive to a unique range of magnetic fluctuation rates, and, as a foreign probe, can be used to study any system, regardless of the constituent atoms or material properties. The main disadvantages are the complexity and size of the measurement apparatus and the possibility of perturbation effects associated with the presence of the muon charge.

Below, I offer a concise explanation of μSR, specifically as it applies to the work presented in this thesis. For a more in-depth discussion, I refer the reader to one of several volumes which have been written on the subject[15, 265, 266, 13].

2.1.2 Muon Production and Decay

A muon is a spin-$\frac{1}{2}$ lepton with a rest mass of m_μ=207m_e, a mean lifetime of τ_μ=2.197μs, and a gyromagnetic ratio of $\gamma_\mu = 2\pi\times135.54\ \frac{MHz}{T}$. Muons come in two varieties: negatively and positively charged. The positive muon (actually an anti-muon), denoted μ^+, has a charge of $+e$, and can be thought of as a light proton in condensed matter systems. Likewise, the negative muon is denoted μ^- and has a charge of $-e$. Negative muons tend to undergo capture by positively charged nuclei in solids, and in the process lose much of their

polarization. They act like $Z-1$ impurities as they fall into an s-orbital essentially within the nucleus, and so are a less passive probe to study the intrinsic properties of the system. Consequently, magnetic μSR measurements are largely (always, in this thesis) performed using positive muons.

Large scale muon production requires the use of medium energy particle accelerators. There are currently four facilities in the world which regularly produce muons for condensed matter purposes. All of the μSR data presented in this thesis were taken with surface muons produced at the TRIUMF in Vancouver, B.C., Canada, and the description below reflects methods used by this institution.

The first step in creating positive surface muons is bombarding targets of low-Z materials, such as carbon or beryllium, with a continuous beam of $\sim 500 MeV$ protons. Collisions between the protons and light nuclei create light mesons called pions through a series of processes[266]:

$$p + p \rightarrow p + n + \pi^+, \tag{2.1}$$

$$p + n \rightarrow n + n + \pi^+ \tag{2.2}$$

$$\text{and} \quad p + n \rightarrow p + p + \pi^-, \tag{2.3}$$

where p, n and π denote protons, neutrons and pions, respectively.

Pions quickly diffuse to the surface of the production target, and undergo a weak decay after τ_π=26.03ns according to[266]

$$\pi^+ \rightarrow \mu^+ + \nu_\mu \tag{2.4}$$

$$\text{and} \quad \pi^- \rightarrow \mu^- + \bar{\nu_\mu}, \tag{2.5}$$

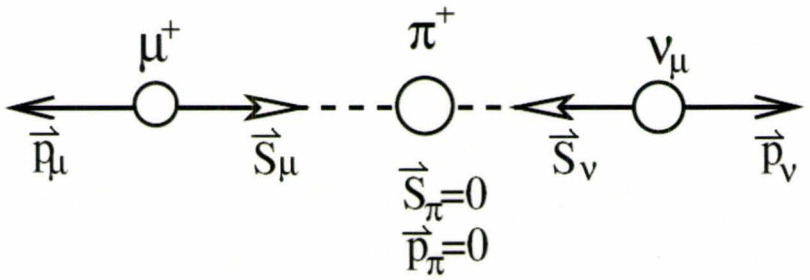

Figure 2.1: The decay of the pion into a muon and muon neutrino. From [11].

where μ, ν_μ and $\bar{\nu_\mu}$ denote muons, muon neutrinos and muon anti-neutrinos, respectively.

In the rest frame of the pion, weak decays can only create neutrinos with spin opposite to their momenta direction - a fact known as "weak violation of parity". As demonstrated in Fig. 2.1, parity violation, together with conservation of momentum and angular momentum, ensures that every muon created via pion decay will have its spin anti-parallel to its momentum. Through the decay of stationary surface pions, TRIUMF creates nearly 100% spin-polarized μ^+ beams with kinetic energy $4.119 MeV$ and momentum 29.79 MeV/c. The (charged) muon beams are then focussed and directed with arrangements of solenoid magnets and muons are implanted one-at-a-time into a sample of interest. Before entering the sample, the muons are passed through a region of crossed electric and magnetic fields (i.e. a 'Wien filter'), which simultaneously cleans the beam of unwanted positrons and rotates the muon spins to the desired orientation.

Inside the sample, muons lose kinetic energy through a series of non-destructive thermalization processes, and come to rest at typical depths of $\sim 0.1 - 0.3mm$ on a time-scale of $< 1ns$. The thermalization processes are

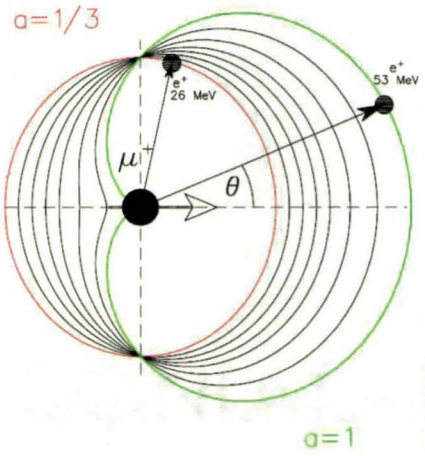

Figure 2.2: The angular probability distribution guiding positron emission from a muon decay. From [12].

Coulombic in nature, and so the spin polarization of the muons remains intact. The spin degrees of freedom of the muon then evolve in the magnetic environment of the sample, as described in the next section. The muon itself undergoes a parity-violating decay according to[266]

$$\mu^+ \rightarrow e^+ + \nu_e + \bar{\nu_\mu}, \tag{2.6}$$

where e^+ denotes a positron.

Again as a result of weak violation of parity, the positron in Eq. 2.6 is emitted *preferentially* in the direction of the muon spin at the time of decay. Specifically, the probability that a positron is emitted at an angle θ from the muon spin direction is given by[266]

$$W(\theta) = 1 + a(\epsilon)\cos\theta, \tag{2.7}$$

where a(ϵ) is known as the 'asymmetry factor' and increases monotonically with the kinetic energy of the positron, ϵ. This function is drawn in Fig. 2.2

for several different positron energies. Experimentalists detect these positrons with plastic scintillation detectors (called 'counters', for obvious reasons), which are largely insensitive to energy. The experimental asymmetry is a complicated integral of $a(\epsilon)$ over energy, the distribution of positron velocities and the solid angle of the positron counters, and thus is generally treated as a fit parameter during data analysis.

Information about the *ensemble average* of the muon spin is obtained by detecting many (~1 - 30 million) decay positrons and noting the momentum direction of each, along with the time of the muon decay. Specifics about extracting and interpreting this information are laid out below.

2.1.3 ZF-μSR

Fig. 2.3 shows a typical experimental geometry for a zero-field μSR (ZF-μSR) measurement. In this setup, a muon enters with its spin anti-parallel to its momentum direction. A thin plastic scintillation counter registers its presence and starts a clock. The muon comes to rest at a crystallographically unique location with a local field, $\mathbf{H_{loc}}$. In a semi-classical picture, the muon spin precesses around the axis of $\mathbf{H_{loc}}$ with a frequency $\omega=\gamma_\mu H_{loc}$. The z-component of the muon spin then evolves according to[13]

$$S_z(t) = \cos^2\theta + \sin^2\theta\cos(\gamma_\mu H_{loc} t), \tag{2.8}$$

where $\hat{\mathbf{z}}$ is the axis of initial spin polarization, and $\cos\theta=\dfrac{\mathbf{H_{loc}}\cdot\hat{\mathbf{z}}}{H_{loc}}$.

After a mean lifetime of ~2.197μs, the muon decays according to Eq. 2.6, and a positron is emitted according to Eq. 2.7. Since the positron counters do

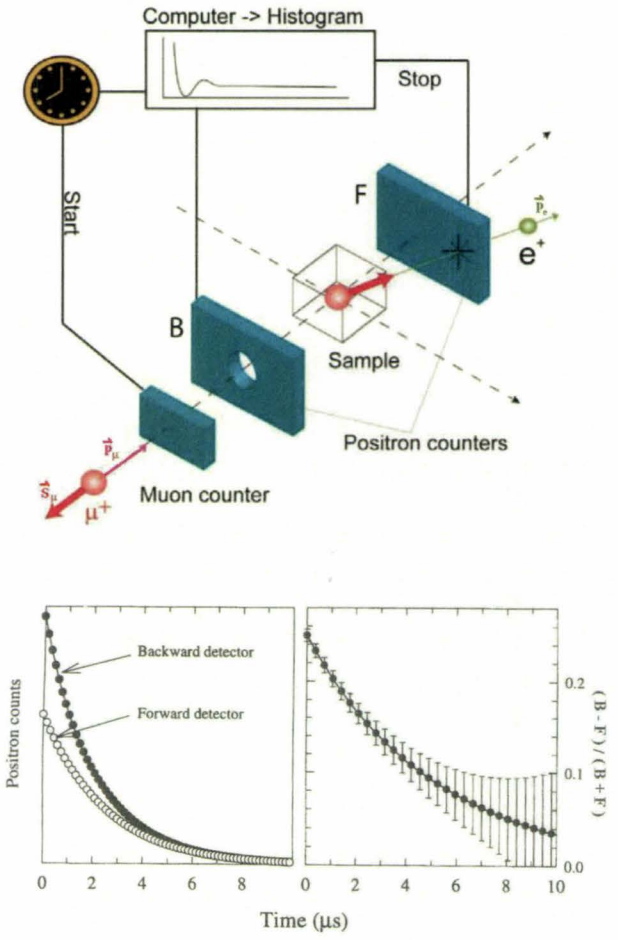

Figure 2.3: A typical ZF-μSR experimental geometry[12], and simulated raw data from such a geometry[13].

not typically cover a 4π solid angle, the decay positron is not always detected. A counter hit stops the clock and is recorded as a good event. If the positron misses, or if a second muon enters the apparatus before the positron is emitted, the event is dismissed and the clock is reset. Usually counters are arranged in diametrically opposite pairs in order to maximize signal size and simplify analysis. One counter is also usually in the direction of the initial muon spin polarization, as this is the direction where the most positrons will be emitted. However, neither of these conditions are strictly required.

For the geometry shown in Fig. 2.3, the number of hits in the backward (B) and forward (F) positron counters is[13]

$$N_{B,F}(t) = N_0(B_{B,F} + e^{-t/\tau_\mu}[1 \pm A_{B,F}\mathcal{P}_z(t)]), \tag{2.9}$$

where the '+' sign is used for the backward counter, and the '-' sign is used for the forward counter. Here, $A_{B,F}$ is the intrinsic detector asymmetry, N_0 is a normalization factor, and $B_{B,F}$ is the time-independent background of the counter, which can be measured. The exponential term in Eq. 2.9 reflects the finite lifetime of the muon. $\mathcal{P}_z(t)$ is the ensemble average of the muon spin polarization along the $\hat{\mathbf{z}}$-axis.

Time histograms from these counters are usually combined to define the 'μSR asymmetry function'[13]:

$$A_z(t) = \frac{(N_B(t) - B_B) - \alpha(N_F(t) - B_F)}{(N_B(t) - B_B) + \alpha(N_F(t) - B_F)} \propto \mathcal{P}_z(t), \tag{2.10}$$

where α is included to account for differences in counter efficiency, and is typically measured separately using a small calibration field.

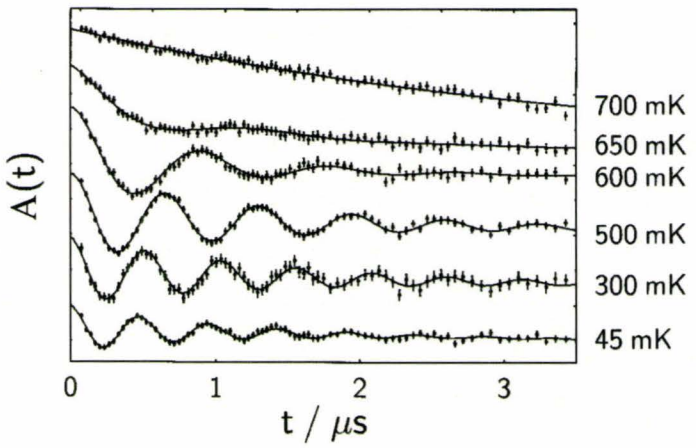

Figure 2.4: Experimental ZF-μSR spectra of p-NPNN entering a long-range ordered state. From [14].

For a static magnetic system, $\mathcal{P}_z(t)$ is obtained by weighting Eq. 2.8 with the local distribution of magnetic fields at the muon site:

$$\mathcal{P}_z(t) = \int\int\int S_z(t)P(H_x)P(H_y)P(H_z)dH_x dH_y dH_z. \qquad (2.11)$$

The local magnetic field distribution contains information about the presence, distribution and evolution of magnetic order as a function of any one of a number of experimental parameters, and in practice, this is the quantity in which a μSR experimenter is interested. Hence, it is informative to explore the consequences of Eq. 2.11 for several cases of interest.

In the presence of ideal long-range magnetic order, the field distribution will be given by one (or a finite number of) Dirac delta function(s). Eq. 2.11 then reduces to a cosine plus a constant, reflecting the coherent precession of the portion of the muon spins perpendicular to the local field direction. Thus, ZF-μSR is a powerful, **k**-integrated detector of magnetic order. This is demon-

strated in Fig. 2.4, which displays the μSR spectra for the organic ferromagnet, p-NPNN, as temperature is lowered through its ordering transition[14].

In any real system, there is always a range of local magnetic fields due to nuclear dipoles, glassy spin order, varying size of ordered moments, domain structures or a variety of other reasons. In such a case, muons at inequivalent sites will precess at slightly different frequencies, and the μSR signal will begin to de-phase.

The simplest case to consider is an isotropic Gaussian distribution of fields about $\mathbf{H}$=0, given by

$$P(H_i) = \frac{\gamma_\mu}{\sqrt{2\pi}\Delta} \times \exp(-\gamma_\mu^2 H_i^2/2\Delta^2), \tag{2.12}$$

where $i \in \{x, y, z\}$. Then, Eq. 2.11 will result in[13]

$$\mathcal{P}_z(t) = \frac{1}{3} + \frac{2}{3}(1 - \Delta^2 t^2)\exp(-\frac{1}{2}\Delta^2 t^2). \tag{2.13}$$

This is known as the Gaussian Kubo-Toyabe formula, and is observed empirically to provide a good description of dense systems of randomly oriented moments, as is the case for nuclear dipole moments and the frozen state of dense spin glasses. The constant term corresponds to the fraction of random local fields which point along the initial muon polarisation direction, and is commonly referred to as the '$\frac{1}{3}$-tail'. For $\Delta \cdot t \ll 1$, Eq. 2.13 reduces to a simple Gaussian relaxation. Gaussians are indistinguishable from low frequency cosines for early times.

An isotropic Lorentzian distribution of fields given by

$$P(H_i) = \frac{\gamma_\mu}{\pi} \times \frac{a}{a^2 + \gamma_\mu^2 H_i^2} \tag{2.14}$$

will result in[13]

$$\mathcal{P}_z(t) = \frac{1}{3} + \frac{2}{3}(1 - at)\exp(-at). \tag{2.15}$$

This is known as the Lorentzian Kubo-Toyabe formula, and is observed empirically to provide a good description of dilute moment systems, such as dilute-alloy spin glasses. For $a \cdot t \ll 1$, Eq. 2.15 reduces to simple exponential relaxation.

More generally, one can always use Eq. 2.11 to associate the measured μSR asymmetry function with a particular distribution of local fields at the muon site, which in turn can be used to model the local magnetic system.

2.1.4 Dynamic Relaxation and LF-μSR

The above description of μSR asymmetry was limited to static distributions of fields, where coherent precession is seen when the *average* field is non-zero, and a decay in signal amplitude is seen when the field distribution has some *width*. That is, for the static case, a decay of the μSR asymmetry results from incoherent precession of muons experiencing slightly different local fields. However, the same effect can be achieved if the local field is fluctuating, and thus decohering the muon precession by arbitrarily changing the speed and axis of rotation.

A useful way of quantifying this effect is with the "strong-collision approximation". In this model, one assumes that the local fields change in a discontinuous and uncorrelated manner with some average frequency, ν. The

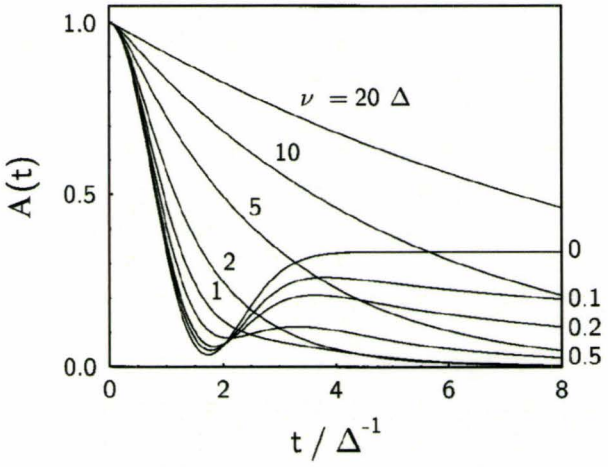

Figure 2.5: Polarization function for a Gaussian distribution of fields, fluctuating at a rate, ν. From [15].

probability of a muon experiencing the same local field for an amount of time, t, is said to be

$$P(t) \propto \exp(-\nu t). \tag{2.16}$$

Eventually, the local field discontinuously jumps, at which point a new local field is chosen from some distribution $P(\mathbf{H})$.

One can show[13] that this leads to the formula

$$\begin{aligned}\mathcal{P}_z(t,\nu) = e^{\nu t} \times [\mathcal{P}_z(t,0) + \nu \int_0^t \mathcal{P}_z(t_1,0)\mathcal{P}_z(t-t_1,0)dt_1 \\ + \nu^2 \int_0^t \int_0^{t_1} \mathcal{P}_z(t_1,0)\mathcal{P}_z(t_2-t_1,0)\mathcal{P}_z(t-t_2,0)dt_1 dt_2 + \cdots],\end{aligned} \tag{2.17}$$

where $\mathcal{P}_z(t,\nu)$ is the polarization function due to a field distribution fluctuating with average frequency, ν.

The case where $\mathcal{P}_z(t,0)$ is given by Eq. 2.13 is well-studied. Analytical forms exist only for the limiting cases, but Fig. 2.5 shows numerical solutions of Eq. 2.17 for increasing values of ν.

In the 'slow fluctuation limit', where $\nu/\Delta \ll 1$, these curves are very nearly Eq. 2.13, but with an additional exponential component to the relaxation. Specifically, the constant tail of the Kubo-Toyabe function is now seen to decay according to[13]

$$\mathcal{P}_z(t,\nu) = \frac{1}{3}\exp\left(-\frac{2\nu t}{3}\right). \tag{2.18}$$

That is, the long-time relaxation is exponential, and depends only on the fluctuation rate.

In the 'narrowing limit', where $\nu/\Delta \gg 1$, the polarization function is dramatically different from Eq. 2.13. Specifically, it is given by[13]

$$\mathcal{P}_z(t,\nu) = \exp\left(-\frac{2\Delta^2 t}{\nu}\right). \tag{2.19}$$

That is, the relaxation is purely exponential over the entire time range, with a rate that varies with Δ^2 rather than Δ.

The simplest way to differentiate between static and dynamic relaxation mechanisms is to apply a magnetic field along the initial muon spin direction in Fig. 2.3, and observe the effect this has on the μSR spectrum. This is what is referred to as a longitudinal-field μSR (LF-μSR) experiment.

Static relaxation functions are strongly affected by longitudinal fields. Again, consider the case of a Gaussian field distribution. In the presence of an applied field of strength H_L along the $\hat{\mathbf{z}}$-axis, Eq. 2.13 is generalized to[13]

$$\begin{aligned}\mathcal{P}_z(t,\nu) = 1 - \left(\frac{2\Delta^2}{\gamma_\mu^2 H_L^2}\right)\left[1 - e^{-\Delta^2 t^2/2}\cos(\gamma_\mu H_L)\right] \\ + \left(\frac{2\Delta^4}{\gamma_\mu^3 H_L^3}\right)\int_0^t e^{-\Delta^2\tau^2/2}\sin(\gamma_\mu H_L \tau)d\tau,\end{aligned} \tag{2.20}$$

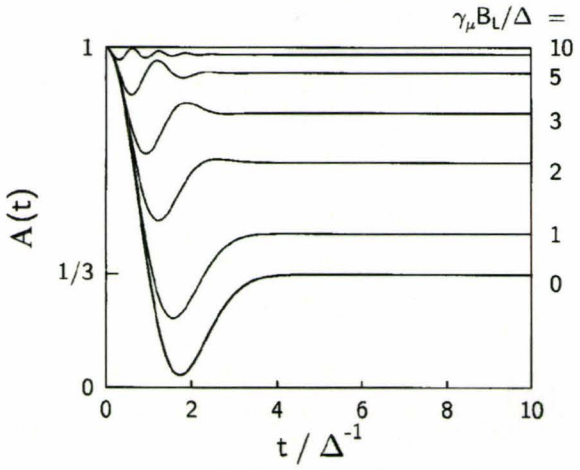

Figure 2.6: Decoupling of the Gaussian Kubo-Toyabe function with increasing LF. From [15].

which is plotted in Fig. 2.6. Of note is the size of the long-time non-relaxing tail of these curves, which quickly and unmistakably grows with field. This effect is referred to as 'decoupling', and reflects the fact that the vector sum of the applied field and dipolar fields is increasingly parallel to the initial muon spin direction.

In contrast, relaxation functions which are dominated by dynamic processes are less sensitive to the presence of applied fields. For example, in the narrowing limit of the strong collision model, Eq. 2.19 becomes[13]

$$\mathcal{P}_z(t,\nu) = \exp\left[-\frac{2\Delta^2\nu t}{\gamma_\mu^2 H_L^2 + \nu^2}\right], \tag{2.21}$$

in the presence of an applied longitudinal field. For typical applied fields and solids, $\gamma_\mu H_L$ is much smaller than ν, and has little effect on Eq. 2.21.

Fig. 2.7 shows data taken on a powder of MnSi at several temperatures in zero-field, and in the presence of a small applied longitudinal field. At high temperatures, the asymmetry has a classic Gaussian Kubo-Toyabe lineshape,

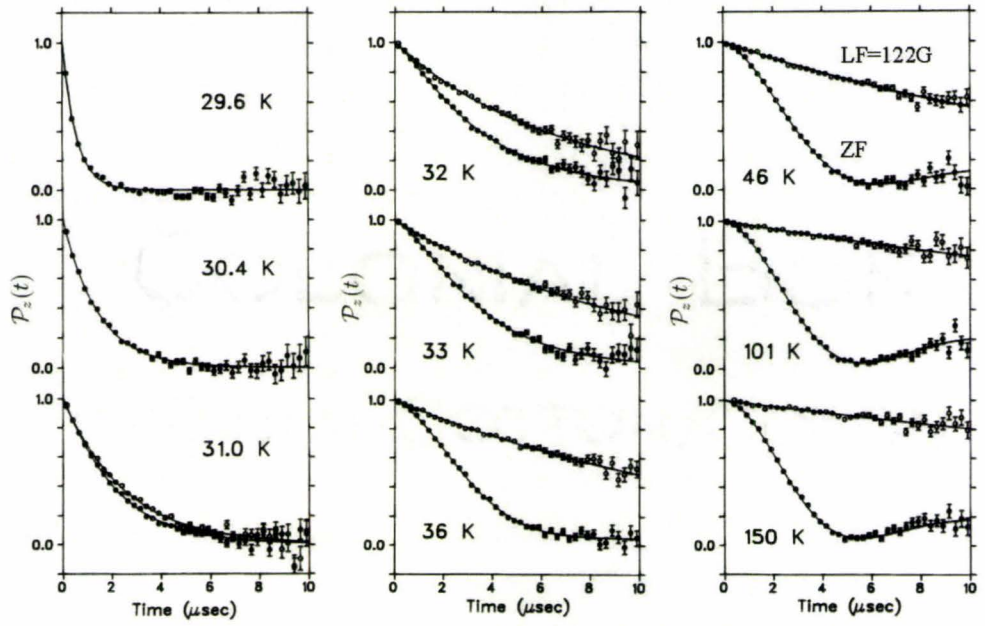

Figure 2.7: Experimental μSR spectra from MnSi at various temperatures in ZF and LF=122G. From [16].

indicative of a static Gaussian distribution of fields. Accordingly, the spectrum is quickly decoupled by the small longitudinal field. At low temperatures, the asymmetry function is relaxed primarily through interaction with critical dynamics above an ordering transition at T_c=29.5K. At these temperatures, the longitudinal field has little to no effect.

2.1.5 TF-μSR

A typical transverse-field μSR (TF-μSR) geometry is shown in Fig. 2.8. Here, the initial spin polarization direction is first rotated 90° by crossed electric and magnetic fields, which also serve to act as a velocity selector. A magnetic field is applied along the beam direction, transverse to the muon spin direction, and positrons are counted in four counters in the plane perpendic-

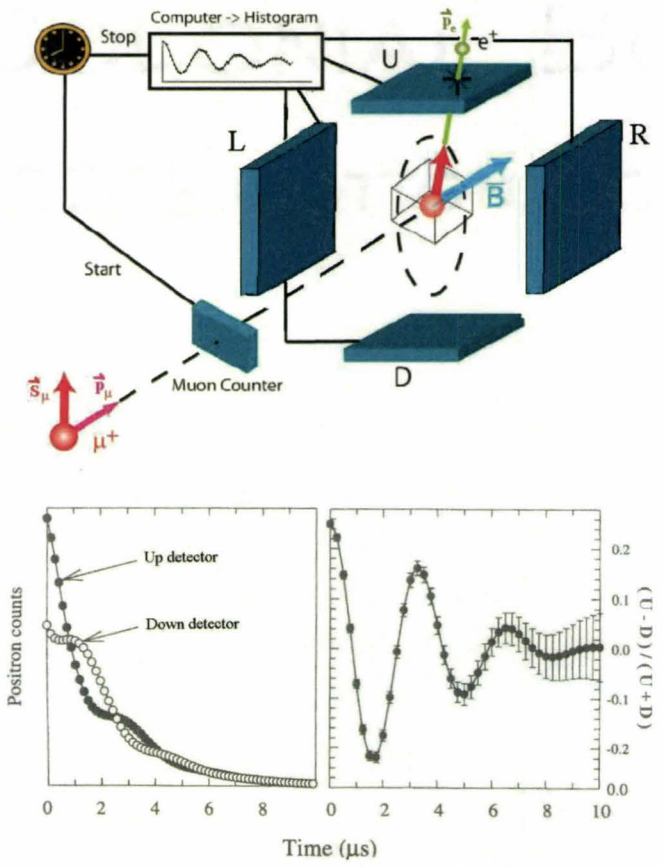

Figure 2.8: A typical TF-μSR experimental geometry (adapted from [12]), and simulated raw data from such a geometry[13].

ular to this axis. As the muon spin will precess predominately around $\hat{\mathbf{z}}$, each of these counters detects a similar number of positrons. Two equivalent μSR asymmetry functions, $A_x(t)$ and $A_y(t)$, are defined in analogy with Eq. 2.10 for opposing pairs of counters, and are fit simultaneously.* For simplicity, the following discussion will only include mention of $A_x(t)$.

Interpretation of TF-μSR data is somewhat simpler than in ZF or LF-μSR. Typical applied fields (>1kG) are much larger than the fields due to the sample. In this case, the local magnetic field will be very nearly perpendicular to the muon spin direction at every muon site, and to a very good approximation, the $\hat{\mathbf{x}}$-direction analogue of Eq. 2.11 reduces to

$$\mathcal{P}_x(t) \propto \int P(H_z)\cos(\gamma_\mu H_z t)dH_z. \tag{2.22}$$

That is, the TF-μSR asymmetry ($\propto \mathcal{P}_x$(t)) is *proportional to the cosine Fourier transform of the distribution of local magnetic fields in the* $\hat{\mathbf{z}}$*-direction*, for a static magnetic system.

For example, a Gaussian distribution of local fields given by

$$P(H_z) = \frac{\gamma_\mu}{\sqrt{2\pi}\Delta} \times \exp(-\gamma_\mu^2(H_z - H_T)^2/2\Delta^2) \tag{2.23}$$

leads to a Gaussian relaxation of signal intensity:

$$\mathcal{P}_x(t) = \cos(\gamma_\mu H_T t) \times \exp(-\frac{1}{2}\Delta^2 t^2), \tag{2.24}$$

* Note: In order to increase fit efficiency and facilitate easy visualization of the data, fits are usually performed with a 'Rotating Reference Frame' analysis. This involves combining $A_x(t)$ and $A_y(t)$ to form two new asymmetry functions, in a way which is effectively rotating the positron counters with respect to the laboratory frame at a frequency close to the muon precession frequency. For a detailed and enlightening discussion of this topic, see Ref. [267].

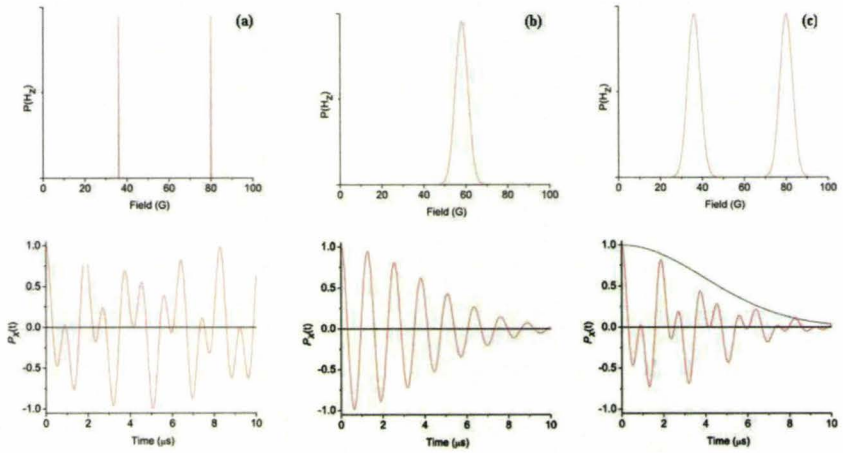

Figure 2.9: (Top)The local field distributions expected for (a)an antiferromagnet, (b)a collection of randomly oriented nuclear dipoles and (c)a combination of the two. (Bottom)The respective TF-μSR spectra derived from the above distributions.

where H_T is the applied transverse field. This is now the appropriate function to describe a system of randomly oriented dipoles.

In contrast, long-range magnetic order manifests itself primarily as a *shift* of the carrier frequency from $\gamma_\mu \cdot H_T$, with little associated relaxation. An ideal, cell-doubling antiferromagnetic state will have a distribution of fields given by

$$P(H_z) = \frac{1}{2}\delta(H_z - H_T - H_{AF}) + \frac{1}{2}\delta(H_z - H_T + H_{AF}), \tag{2.25}$$

where H_{AF} is the contribution to the local field from the ordered moments. According to Eq. 2.22, this leads to

$$\mathcal{P}_x(t) = \frac{1}{2}\cos(\gamma_\mu(H_T - H_{AF})t) + \frac{1}{2}\cos(\gamma_\mu(H_T + H_{AF})t). \tag{2.26}$$

For a real material, ordered moments co-exist with nuclear dipoles and small amounts of disorder, which serve to broaden the local field distribu-

tion. In this case, the appropriate distribution function is a *convolution* of Eqs. 2.25 and 2.23. By the convolution rule of Fourier transforms, the appropriate polarization function is then the *product* of Eq. 2.26 and 2.24. This is demonstrated in Fig. 2.9. By the same token, the appropriate polarization function to describe multiple relaxation mechanisms is the product of the individual polarization functions.

As in the ZF case, magnetic fluctuations also have the potential to relax the TF-μSR signal. For the Gaussian distribution of Eq. 2.23 in the strong collision approximation, the TF signal will decay approximately according to the Abragam formula[268]:

$$\mathcal{P}_x(t,\nu) = \exp\left[-\frac{\Delta^2}{\nu^2} \times e^{-\nu t} - 1 + \nu t\right]. \tag{2.27}$$

For $\nu \gg \Delta$, the relaxation function in TF is the same as that in LF. This is the μSR counterpart to the NMR principle known as 'the equivalence of $1/T_1$ and $1/T_2$ in the narrowing limit'.

2.2 Magnetization

2.2.1 Linear and Non-Linear Magnetic Susceptibility

Magnetization, **M**, is defined as the magnetic moment per unit volume produced by a sample, usually in response to an applied magnetic field, **H**. This quantity contains information about the spin and orbital angular momentum degrees of freedom in an electronic system, and is often studied as a function of

temperature and field to gain insight into condensed matter systems[269, 270]. In particular, sharp features in $\mathbf{M}(\mathbf{H},\mathrm{T})$ are taken as signs of phase transitions.

As magnetization is an odd function of the magnetic field, a Taylor expansion of M in powers of H gives:

$$M(H,T) = \chi_1(T) \cdot H + \frac{\chi_3(T)}{3!} \cdot H^3 + ... = \sum_{n=1}^{\infty} \frac{\chi_{2n-1}(T)}{(2n-1)!} \cdot H^n, \qquad (2.28)$$

where the $2n-1^{th}$ order magnetic susceptibility, χ_{2n-1}, is defined as the $2n-1^{th}$ derivative of M. For simplicity, I have also taken $\mathbf{M}||\mathbf{H}$.

The largest and most often studied term in Eq. 2.28 is the linear term. Several well-known formulas exist to describe $\chi_1(T)$ in specific situations. Canonical Fermi liquids are described by the temperature independent Pauli susceptibility (Eq. 1.6). Local moment systems are described by the Curie-Weiss formula:

$$\chi_1(T) = \frac{C}{T-\Theta}, \qquad (2.29)$$

where C is the Curie constant ($\propto$ moment^2) and Θ is the Weiss constant ($\propto$ magnetic exchange). Although, it should be stated explicitly that neither of these temperature dependences can be uniquely interpreted. In general, χ_1(T) can take on a variety of forms as the system being explored becomes more complex.

In low fields, the cubic and higher terms in Eq. 2.28 are often ignored to a first approximation. However, these terms contain information about the crystal field levels and multipolar interactions in magnetic systems, and can be as useful as the linear susceptibility. For example, the cubic susceptibility, $\chi_3(T)$, of rare earth intermetallic and heavy fermion compounds have been

studied in this context in the past[271, 272, 21, 273]. Chapter 5 largely deals with this quantity.

2.2.2 The SQUID Magnetometer

All susceptibility data presented in this thesis were taken on a Quantum Design MPMS SQUID magnetometer. A schematic of the basic design is shown in Fig. 2.10. The instrument consists of a stepper motor which translates the sample of interest through a set of pickup coils, which are inductively coupled to an rf-Superconducting QUantum Interference Device (SQUID). This outputs a characteristic AC voltage curve from which one can extract the net magnetic moment of the sample, as described below. The system is also equipped with a liquid-He flow control system, with which one can control temperature in the range $1.7K$-$300K$, and a superconducting solenoid, which can apply uniform magnetic fields up to $5.5T$.

The heart of the instrument is the rf-SQUID. An rf-SQUID is a loop of superconducting material interrupted with a single Josephson junction. As described elsewhere[22], an LC tank circuit inductively coupled to an rf-SQUID provides an output voltage (for a given input current), which sensitively depends on the magnetic flux enclosed by the superconducting loop. Thus, a simple magnetometer can be constructed by inductively coupling a single 'pickup loop' of superconducting material to an rf-SQUID, and comparing the voltage output of the tank circuit with the sample inside and outside of this loop. In theory, an rf-SQUID can detect fields as small as $10^{-15}T$ with this design.

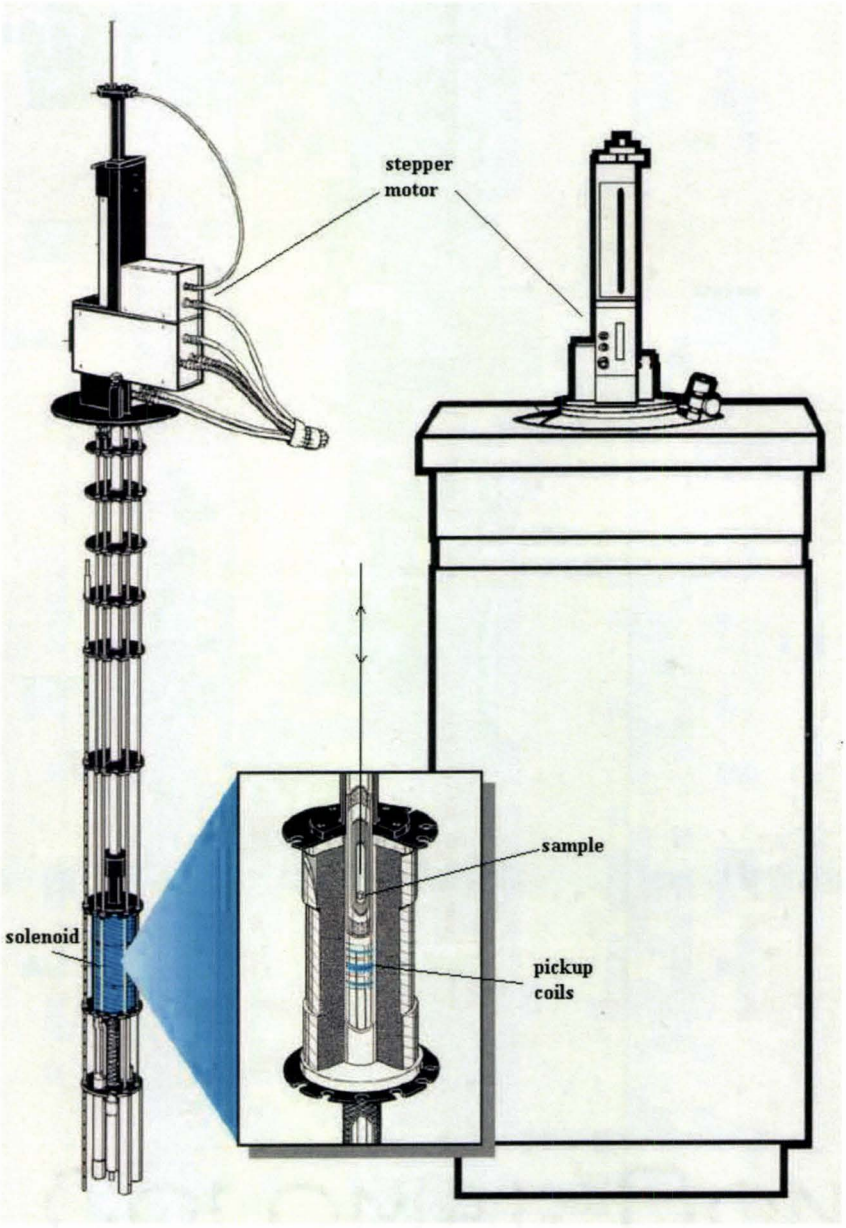

Figure 2.10: A schematic of Quantum Design MPMS SQUID magnetometer (adapted from [17]).

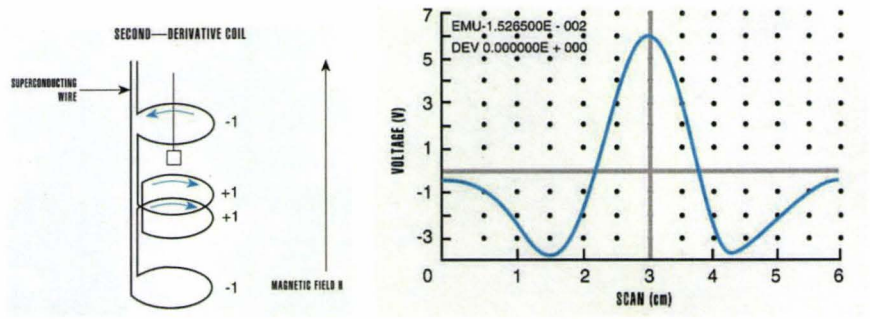

(a) (b)

Figure 2.11: (a)Diagram of the second differential gradiometer coil in the Quantum Design MPMS magnetometer, and (b)the output voltage expected from moving a sample linearly through these coils. From [17].

In actuality, the pickup circuit is more complicated than just a single loop. The MPMS uses a second differential gradiometer, as shown in Fig. 2.11(a). This system uses four identical coils, with the two centre coils wound oppositely to the others. As a result, neither uniform fields nor fields which vary linearly in space create a signal in the SQUID. This greatly reduces the background signal due to noise and linear drift in the applied field. Linearly stepping a point-like sample through the gradiometer results in a voltage versus position curve like the one shown in Fig. 2.11(b). The difference between the maximum and minimum voltage is proportional to the net moment, and the magnetization of the sample is extracted from a linear regression fit to the voltage versus position curve.

2.3 High-Pressure Apparatus

In addition to field and temperature, magnetic systems are increasingly being investigated as a function of applied pressure. Pressure can vary rel-

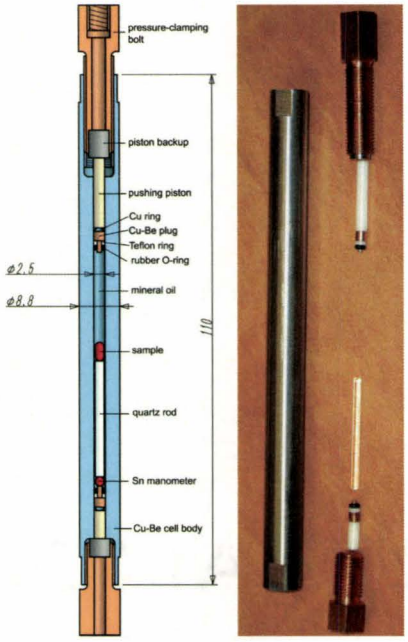

(a) (b)

Figure 2.12: (a)Schematic of a clamp pressure cell, designed for use in a commercial SQUID magnetometer. (b)Photograph of the same cell. (Courtesy of Tatsuo Goko.)

ative positions of atoms in a solid, resulting in changes of the magnitude or sign of various exchange constants and the level of hybridization between different electron species. This often results in a quantum critical transition into a fundamentally new magnetic ground state. Examples include pressure induced superconductivity in UCe_2Ge_2[274], destruction of long-range ferromagnetism in UGe_2[275] and the occurrence of long-range antiferromagnetism in URu_2Si_2[249].

2.3.1 Piston Clamp Cells

The most common method of applying pressure to crystals is the piston clamp cell. The basic concept of this device is simple. A sample of interest is mounted in a closed space inside a rigid cell body. This space is filled with a pressure-carrying medium with small compressibility, usually some form of mineral oil. One end of the closed space consists of a piston, the position of which can be adjusted by the experimenter. Moving the piston decreases the volume of the interior space, which increases the hydrostatic pressure of the fluid containing the sample.

Fig. 2.12 shows a schematic and photograph of the piston clamp cell used in Chapter 5 of this thesis, which was designed by Tatsuo Goko of TRIUMF. The cell body is machined from a single piece of a Cu-Be alloy. The alloy was chosen for its hardness and lack of strong magnetic properties. The enclosed space is formed with the use of two Cu-Be plugs. Three sets of deforming seals are used (rubber, Teflon, copper), each designed to cover a different pressure range. One of the Cu-Be plugs is backed with a tungsten-carbide 'pushing piston'. The crystal to be studied is mounted on a quartz rod in the centre of the cell.

Pressure is applied by coupling to the pushing piston with a hydrostatic press, and screwing the clamping bolt in place once the piston is at the desired position. A rough estimate of the pressure inside the cell is obtained by monitoring the oil pressure of the hydrostatic press and multiplying by a ratio of areas and calibration factors to account for the effect of temperature. A more precise measure of pressure is obtained by monitoring the superconducting transition temperature of a piece of high-purity tin, which is inside the

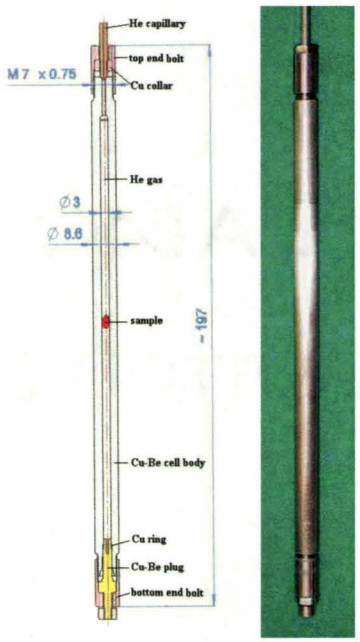

(a) (b)

Figure 2.13: (a)Schematic of a helium pressure cell, designed for use in a commercial SQUID magnetometer. (b)Photograph of the same cell.

enclosed volume, but well-removed from the sample location. The maximum pressure obtainable by this cell is 1.5GPa.

A similar, but not identical design is described in more detail in Ref. [276].

2.3.2 Helium Cells

An alternate approach is to use helium as a pressure medium. A schematic and photograph of a GC10/3 Unipress Gas Pressure Cell is shown in Fig. 2.13. A long, uniform cell body with a 3mm bore is machined out of a Cu-Be alloy. The sample of interest is suspended in the middle of the bore through the use of a Kapton straw. The bottom end of the cell is stopped by a Cu-Be plug

with a Cu crushing ring, and held in place by the bottom end bolt. The top end bolt is a feedthrough coupling to a capillary with a 0.3mm diameter bore. This capillary is connected to a volume of helium gas, which is pressurized with a piston assembly outside the measurement apparatus.

Fig. 2.14 is a photograph of a U11 Unipress Gas Compressor assembly, which is used in conjunction with the cell described above. It consists of a closed volume of oil which is coupled to a volume of helium gas (including that in the sample cell) through a series of pistons. A compressor pump can create oil pressures of up to 70MPa. By selectively opening valves, this oil pressure is used to drive three pistons of different radius, thereby decreasing the volume and increasing the pressure of the helium gas. This method can create pressures of up to 1.5GPa, although the sample cell described above is limited to working pressures of 700MPa due to the thinness of the cell walls. A resistive Mn pressure gauge is attached to the output capillary of the compressor to actively measure pressure during the measurement.

There are several advantages to this apparatus over a conventional clamp pressure cell. The first is a greatly reduced (though not absent) uniaxial component to the pressure tensor. This is due to the fact that the cohesive force for solid helium is a relatively weak van-der-Waals force, and thus helium cannot support much shear stress. Secondly, the piston position in the compressor assembly is not locked into place, but determined by an equilibrium condition between the gas and oil. Therefore, the pressure in the gas is actively maintained and does not change with temperature. Lastly, one can change

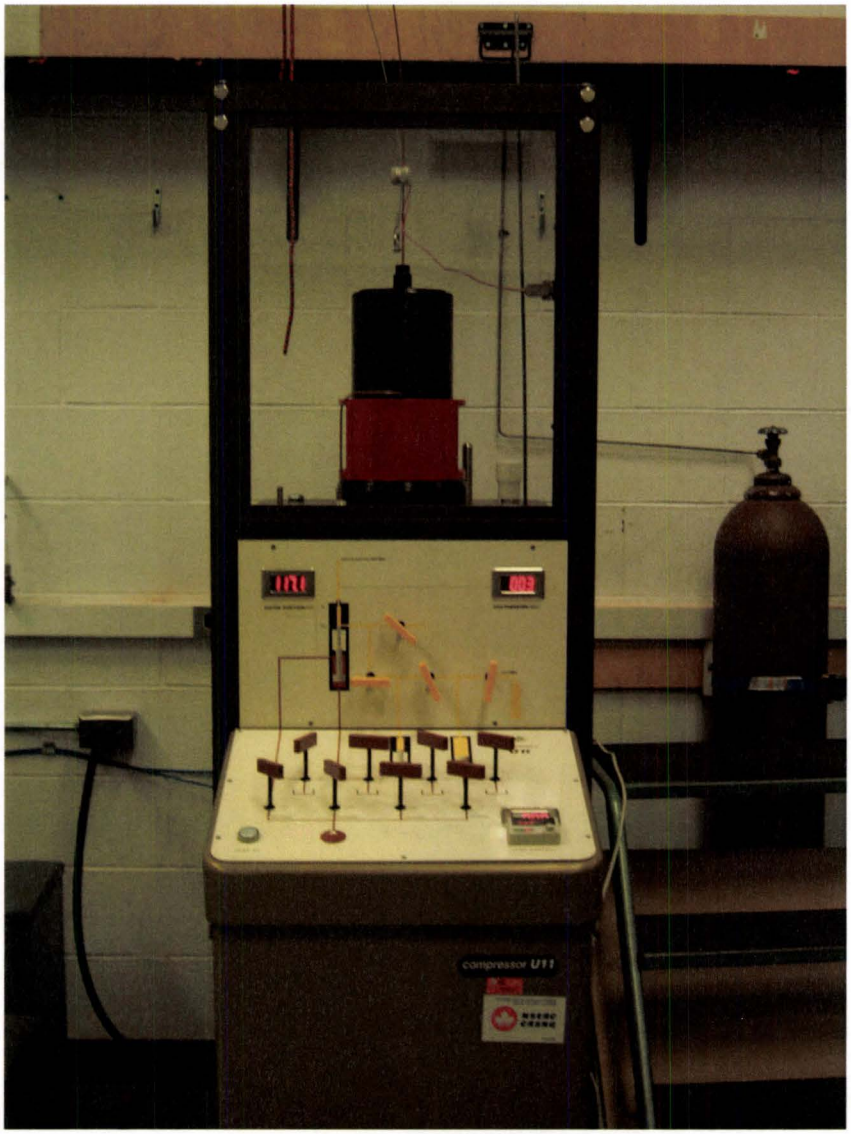

Figure 2.14: The Unipress gas compressor used to pressurize the helium pressure cell.

pressures in situ and at any temperature greater than the (finite pressure) helium melting temperature. This greatly speeds the measurement process.

The main disadvantage of this technique is a smaller range of allowed pressures, with the maximum pressure of a helium cell being approximately half that of the equivalent piston clamp cell.

Chapter 3

The Search for Time-Reversal Symmetry Breaking in the Pseudo-Gap State of Cuprate Systems

Although not reproduced verbatim, this chapter incorporates the article "Absence of broken time-reversal symmetry in the pseudogap state of the high temperature $La_{2-x}Sr_xCuO_4$ superconductor from muon-spin-relaxation measurements", which has been published in Physical Review Letters (Physical Review Letters, Volume 101, 017001, 2008)*. Figures 3.1, 3.2, 3.4 and 3.6 are reproduced from said article with permission. An extension of the original work to two related compounds, $HgBa_2CuO_{4+\delta}$ and $La_{1.875}Ba_{0.125}CuO_4$, is included as an addendum.

* ©(2008)The American Physical Society

Absence of broken time-reversal symmetry in the pseudogap state of the high temperature $La_{2-x}Sr_xCuO_4$ superconductor from muon-spin-relaxation measurements

G. J. MacDougall,[1] A.A. Aczel,[1] J.P. Carlo,[2] T. Ito,[2] J. Rodriguez,[1] P.L. Russo,[2,3] Y.J. Uemura,[2] S. Wakimoto,[4] and G.M. Luke[1,5]

[1] *Department of Physics and Astronomy, McMaster University, Hamilton, ON, Canada, L8S-4N3*

[2] *Department of Physics, Columbia University, New York, NY, USA, 10027*

[3] *TRIUMF, Vancouver, British Columbia, Canada, V6T 2A3*

[4] *Quantum Beam Science Directorate, Japan Atomic Energy Agency, Tokai, Ibaraki, Japan 319-1195*

[5] *Canadian Institute for Advanced Research, Toronto, Ontario, Canada, M5G 1Z8*

Abstract

We have performed zero-field μSR measurements on single crystals of $La_{2-x}Sr_xCuO_4$ to search for spontaneous currents in the pseudo-gap state. By comparing measurements on materials across the phase diagram, we put strict upper limits on any possible time-reversal symmetry breaking fields that could be associated with the pseudo-gap. Comparison between experimental limits and the proposed circulating current states effectively eliminates the possibility that such states exist in this family of materials.

More limited data sets on single crystals of $HgBa_2CuO_{4+\delta}$ and $La_{2-x}Ba_xCuO_4$ are also presented, and discussed in the same context.

3.1 Introduction

The nature of the pseudo-gap and its relation to superconductivity are among the largest outstanding problems in cuprate research. To date, many theories of the pseudo-gap have been put forth and debated, but experiments have not definitively elevated one above the rest[72, 73, 3].

One theory which has been receiving particular attention of late is the 'circulating current' picture of Varma[160, 161, 162, 163, 164]. In this proposal, the pseudo-gap temperature, T^*, represents a real phase transition temperature to a novel ordered state, which is characterized by spontaneous currents flowing in specific patterns in the copper-oxide planes. This line of phase transitions terminates in a quantum critical point (QCP) inside the superconducting dome, and the resulting quantum fluctuations are ostensibly responsible for both the superconductivity and the non-Fermi-liquid-like behavior at optimal doping.

Theoretical work on this proposal has been extensive, and the model reproduces many features of the cuprate phase diagram. However, the experimental situation is much less conclusive, largely due to the difficulty in coupling to the proposed order parameter. To date, the main experimental case for this picture rests on two sets of experiments, both hotly contested.

The first is the apparent observation of dichroism in the ARPES spectrum of $Bi_2Sr_2CaCu_2O_{8+\delta}$ (Bi-2212)[277]. Kaminski et al. measured the difference in the induced photocurrent when thin films of Bi-2212 were bombarded with left and right circularly polarized light. They saw a difference in the absolute intensity of these currents at temperatures below a critical temperature in un-

derdoped samples and associated this with the pseudo-gap transition. Such dichroism is indicative of a time reversal symmetry breaking (TRSB) field in the pseudo-gap state: a key prediction of the circulating current theory. By varying the propagation direction of the incident light and detector position, they were able to explore the symmetry of the ARPES matrix, and thus the underlying TRSB state. The symmetry of the dichroism was not consistent with original predictions, but an alternate current pattern was quickly proposed that could explain the data[162]. This pattern is displayed in Fig. 3.1.

However, the above experiment was criticized[278] for failing to account for the super-lattice structural distortions, which are widely acknowledged to exist in this material and are evinced explicitly by X-ray studies[279]. The dichroism claimed above was an extremely small effect ($\sim$3%), and requires precise alignment of the experimental apparatus relative to the crystallographic unit cell. A later experiment on using single crystal without super-lattice distortions and an apparatus with fewer moving parts saw no such effect[280].

More recent results have come from spin-polarized neutron scattering. This technique involves polarizing the spin of incident neutrons, and selectively counting scattered neutrons which have had their spins flipped, indicating a magnetic (as opposed to nuclear) scattering event. A spin-polarized neutron scattering group reported seeing commensurate magnetic peaks arising near the pseudo-gap temperature in several samples of $YBa_2Cu_3O_{6+x}$ (YBCO)[281]. These results have since been reproduced by other groups using crystals of YBCO[282] and also $HgBa_2CuO_{4+\delta}$ (Hg-1201)[18]. The locations of the peaks in reciprocal space were consistent with the above current pattern inferred

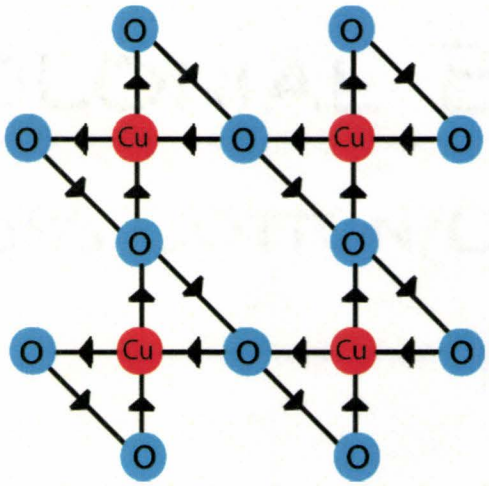

Figure 3.1: The orbital current pattern in the CuO_2 plane, inferred from ARPES and neutron scattering data.

from the ARPES data, and the authors of these papers clearly favour this interpretation.

However, the authors have also been careful to note that relatively few magnetic peaks have been measured, and have given further examples of spin arrangements which could alternatively explain the data[281, 283]. Furthermore, the observed orientation of the local dipole moments was $\sim 45^{\circ}$ from the $\hat{\mathbf{c}}$-axis, and inconsistent with in-plane currents. Originally interpreted as a manifestation of small distortions of the copper-oxide planes, this explanation did not work for Hg-1201, which has no such distortions, and it was necessary to postulate a co-existing spin order to reconcile this fact with the theory[284].

Given these concerns, it is evident that clarifying experiments are needed before drawing any general conclusions. Muon spin rotation (μSR) is in an especially good position to illuminate the situation. It can readily detect the TRSB fields that would necessarily accompany the proposed current order. It

probes local properties of the bulk, making it largely insensitive to impurity and surface effects which might confuse interpretation. In addition, its sensitivity to TRSB fields as small as $0.5G$ has been repeatedly demonstrated in other superconducting materials[214, 215, 285, 216] as well as in a long list of weak magnetic systems. The effect would be even more pronounced in the present scenario, as muons would precess coherently in the long-range ordered state, should it exist.

In an attempt to address the outstanding questions regarding circulating current order in the cuprates, we have performed zero-field μSR (ZF-μSR) on several single crystals of $La_{2-x}Sr_xCuO_4$ (LSCO), both inside and outside of the pseudo-gap regime. LSCO was chosen because its pseudo-gap has been well mapped out[2], and high quality single crystals exist with a wide range of carrier concentrations. This afforded us the ability to compare pseudo-gap and non-pseudo-gap materials directly by varying the amount of Sr in the system, and avoided the ambiguity involved in defining the pseudo-gap temperature. In this way, we are able to effectively eliminate the possibility that the previously discussed circulating current state exists in LSCO.

3.2 Experimental Details

Three crystals were grown via the travelling solvent floating zone method, with x=0.13 (T^* $\sim$150K), x=0.19 (T^* $\sim$75K) and x=0.30 (T^*=0K), where the values of T^* are those reported by recent ARPES studies[2]. Samples were cut into $\sim$1mm thick plates with the large face perpendicular to the $\hat{\mathbf{c}}$-axis. The crystals were grown by T. Ito of AIST at Tsukuba and S. Wakimoto of

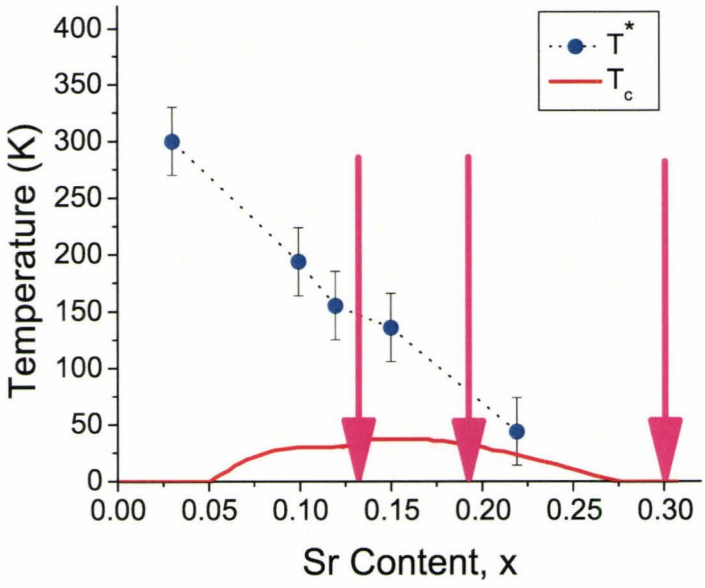

Figure 3.2: The experimental phase diagram of $La_{2-x}Sr_xCuO_4$. Data is taken from Ref. [2]. The purple arrows indicate the dopings and temperature range explored in the current study.

the University of Toronto. Both the growth conditions and sample properties are described in more detail elsewhere[20, 165].

ZF-μSR spectra were taken in a He-flow cryostat on the M20 beamline at TRIUMF, in Vancouver, Canada. Background fields were constrained to be less than $\sim 50mG$ using three sets of orthogonal Helmholtz coils. The apparatus and crystals used allowed us to explore the region of the phase diagram indicated by the arrows in Fig. 3.2, crossing the pseudo-gap transition line along both the temperature and doping axes.

As described in Chapter 2 of this thesis, ZF-μSR consists of implanting muons one at a time, and allowing the muon spins to evolve in the presence of the local internal field. Muons then decay with a mean lifetime $\tau_\mu = 2.2\mu s^{-1}$,

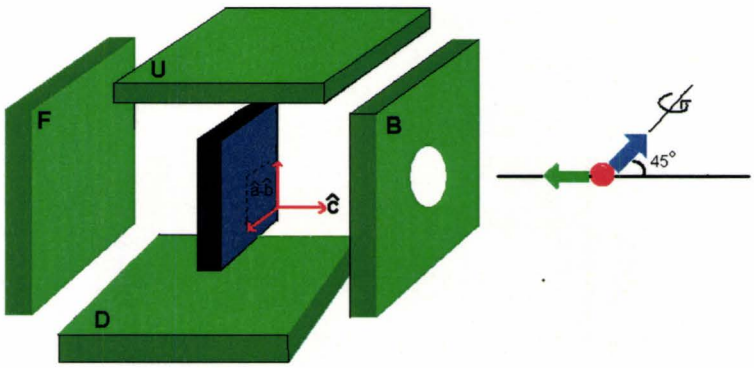

Figure 3.3: A schematic demonstrating the relative orientation of the initial spin polarization, positron detectors and crystalline axes for this experiment.

and emit a positron preferentially along the instantaneous spin direction at the time of decay. Time spectra are then constructed by measuring positron counts in sets of diametrically opposed counters. In contrast to the usual procedure, the muons in this study were inserted with their spins initially polarized $\sim$45° from the beam axis ($\|\hat{\mathbf{c}}$). Time spectra were then simultaneously measured along axes both parallel and perpendicular to $\hat{\mathbf{c}}$. A schematic of the position of the counters and initial muon polarization axis relative to the crystal axes for this experiment is shown in Fig. 3.3.

The evolution of a single muon spin in the presence of a local field, $\mathbf{B_{loc}}$ is given by

$$S_z(t) = \cos^2(\theta) + \sin^2(\theta)\cos(\gamma_\mu B_{loc} t), \tag{3.1}$$

where θ is the angle between the local field and initial spin direction, and γ_μ=0.0852$\mu s^{-1} G^{-1}$. The μSR asymmetry spectrum is built from an ensemble of such muons, and represents a convolution of Eq. 3.1 with the local distribution of magnetic fields.

Our unusual choice for initial muon polarization direction was designed to avoid the exceptional case where $sin^2(\theta)$=0 in Eq. 3.1. Muons are known to lie in one of eight positions, related to each other through reflections in x=0, y=0 and z=0 for a unit cell centered on the copper ion[286]. Since the proposed magnetic order does not satisfy all of these reflections, we can say with certainty that the local field does not lie along the initial (low symmetry) spin direction for every muon site. Some muons will always precess in the presence of such order, which might not have been the case if the initial muon polarization lay along a high symmetry direction, like $\hat{\mathbf{c}}$.

Alternatively, we could have performed two sets of ZF measurements, with the initial polarization direction along two orthogonal axes. This is the approach we take for measurements presented in the addendum to this chapter.

3.3 Results

In a long-range ordered state, the distribution of local fields is very close to a delta-function, and μSR should see coherent precession at a frequency set by the average magnetic field at the muon site. The black line in Fig. 3.4 demonstrates such precession in the presence of a $41G$ field, which was (as described in the next section) the numerically estimated mean field at the muon site from the current pattern of Fig. 1 with a moment of $0.05\mu_{\mathrm{B}}$. The red line in Fig. 3.4 is the expected spectra for a Gaussian distribution of fields with a half-width of $41G$, as might be expected for an ordered state in the presence of local disorder. This is discussed later.

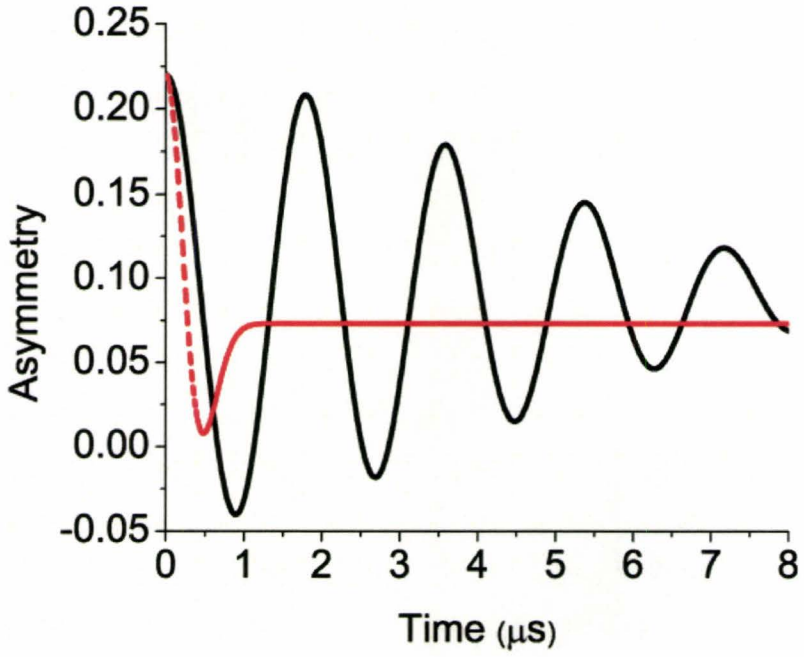

Figure 3.4: The expected μSR spectra for a material with the long-range-ordered current pattern seen in Fig. 3.1 (black) and for a material with a local distribution of fields of similar size (red).

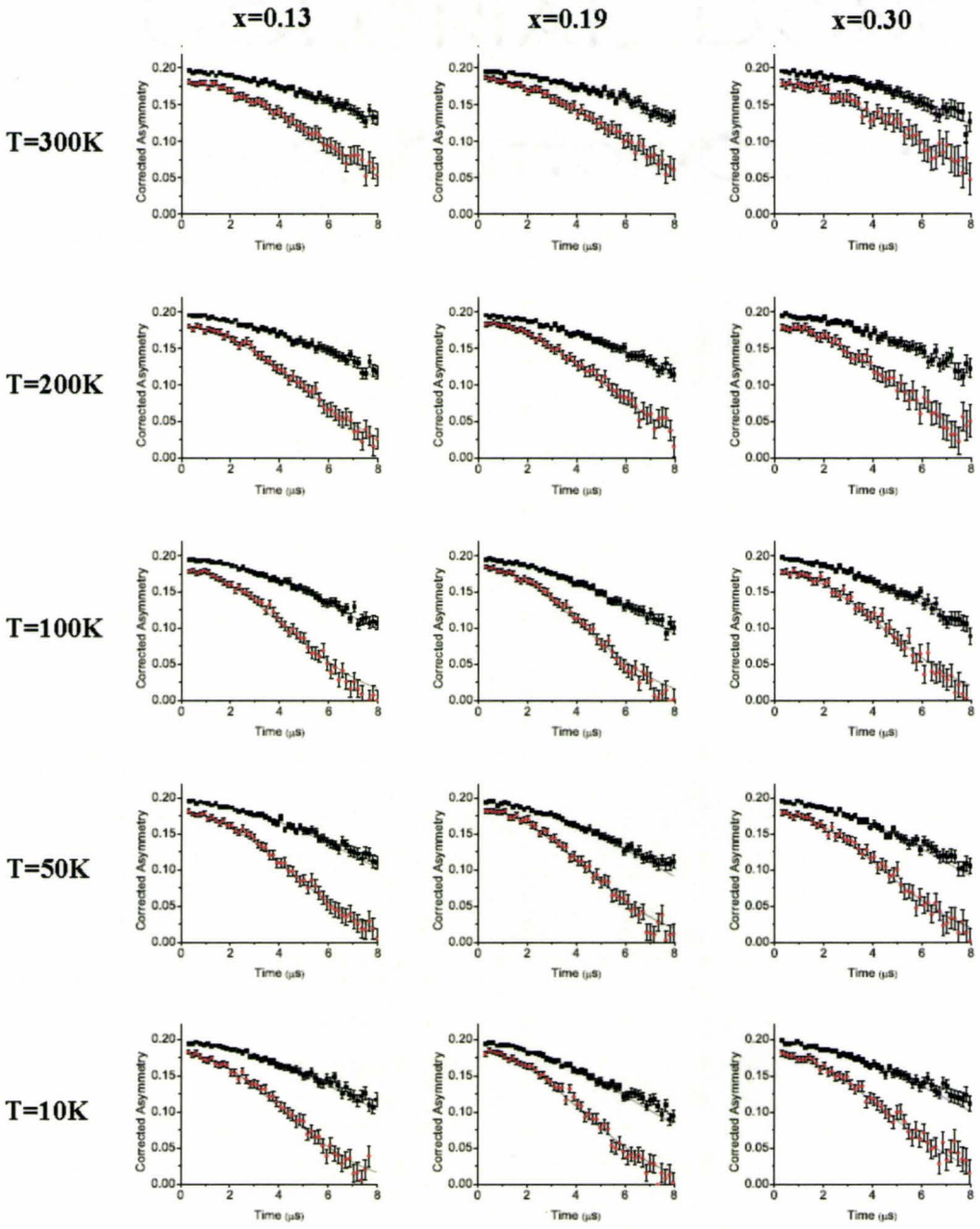

Figure 3.5: The measured μSR spectra observed in three crystals of $La_{2-x}Sr_xCuO_4$ with different amounts of Sr at temperatures below and above T^*. The top (bottom) curves represent spectra taken with counters oriented in (out of) the copper-oxide planes. Solid lines represent fits to Eq. 3.2.

Fig. 3.5 shows several ZF-μSR spectra, corrected for relative counter efficiency, for the three LSCO crystals at temperatures ranging from $300K$ to $10K$. In each plot, the asymmetry for counters oriented in (top) and out (bottom) of the copper-oxide planes is plotted. In neither set of counters is there any sign of the predicted precession at any temperature, and spectra below and above the respective pseudo-gap transition temperatures look strikingly similar. Indeed, the spectra are more indicative of a local field distribution dominated by randomly oriented nuclear dipole moments, which are orders of magnitude smaller than typical magnetic moments. More importantly, there is no obvious difference in the spectra for the underdoped and overdoped crystals, despite the samples being on opposite sides of the pseudo-gap transition line.

Each spectrum was fit to the standard Kubo-Toyabe form expected for a Gaussian distribution of random fields:

$$A(t) = \frac{A_0}{3} + \frac{2A_0}{3}(1 - \Delta^2 t^2)\exp(-\frac{1}{2}\Delta^2 t^2), \tag{3.2}$$

where Δ/γ_μ is the width of the magnetic field distribution. For $\Delta \cdot t \ll 1$, this equation reduces to a Gaussian function, with Δ equal to the rate of relaxation.

The results of these fits are summarized in Fig. 3.6. There is clearly no strong temperature dependence of the μSR spectra in any of the three crystals. At low temperatures, the rate of relaxation is constant, again consistent with what one would expect for a field distribution dominated by randomly oriented nuclear dipoles. There is a slight reduction in Δ above $175K$ in each of the crystals, but no dramatic change in the system at T^*. In these materials, $175K$

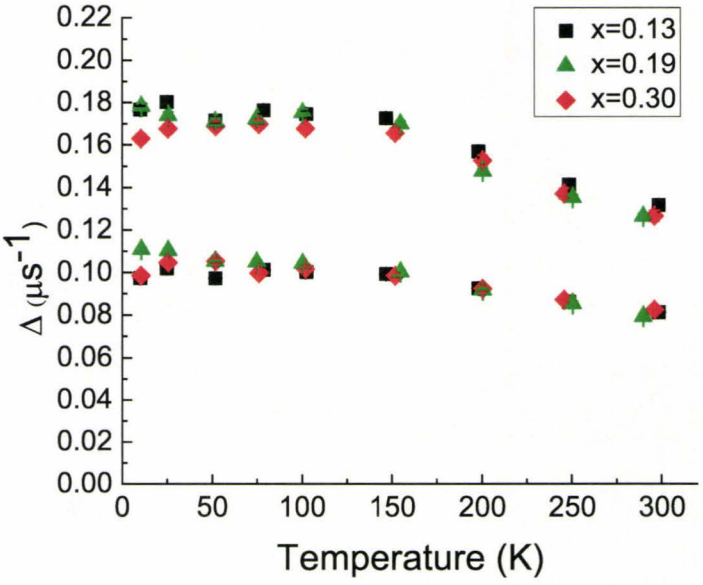

Figure 3.6: The results of fits to the ZF-μSR spectra to Eq. 3.2. Points on the upper (lower) curve represent fits from spectra with counters in (out of) the copper-oxide planes. Error bars are comparable to the plot symbol sizes.

marks the onset of muon diffusion[287], which acts to motionally narrow the dipolar relaxation; the slight decrease in Δ above this temperature reflects this effect. The relaxation rate of the spectra from counters perpendicular to $\hat{\mathbf{c}}$ were larger than those from spectra with counters parallel to $\hat{\mathbf{c}}$ due to particulars of the distribution of dipoles in relation to the known muon site.

Again, more important than the temperature dependence of the local field distribution is its independence from the Sr concentration. The gradual increase of pseudo-gap properties makes it difficult to correlate material properties via temperature. However, it is known that the pseudo-gap is strong in the underdoped materials and absent by x=0.30[72, 73, 3, 2]. Consequently, the observation that the three crystals investigated here have identical μSR spectra at every temperature puts tight restrictions on any TRSB fields which might be associated with the pseudo-gap state. Specifically, the average scatter of points in Fig. 3.6 is $0.003\mu s^{-1}$, which puts an upper limit of $\sim 0.05G$ on such fields at the muon site.

3.4 Numerical Simulations

The above experimental limit is quite restrictive for any magnetic order which is observable by neutron scattering. (For example, antiferromagnetic alignment of $0.5\mu_B$ moments in the parent compound, La_2CuO_4, manifests itself as a $300G$ field at the muon site.) However, since both the proposed current pattern (Fig. 3.1) and the muon site[286] are known, we are able to make a more quantitative theoretical prediction.

Table 3.1: Local Fields versus Sum over $2N \times 2N \times 2N\frac{a}{c}$ Unit Cells

N	B_x	B_y	B_z	$\|\vec{\mathbf{B}}\|$
one butterfly	64.5116989	136.051754	-161.073228	1145.23194
0	59.6537503	135.782646	-143.385036	1071.46021
1	-3.50360009	98.2419773	-117.457183	795.54637
2	-4.87975588	98.9212	-122.469233	818.08268
3	-5.02529238	99.2098362	-123.713081	824.07637
4	-5.02965052	99.2768267	-123.903776	824.07637
5	-5.00533302	99.3116447	-123.909448	825.19907
7	-4.88344179	99.437668	-123.815938	825.21013
10	-4.84219021	99.4790183	-123.781901	825.20027
25	-4.80768881	99.5135351	-123.753814	825.19345
50	-4.80115275	99.520074	-123.748552	825.19241
75	-4.79987396	99.5213529	-123.747524	825.19221
100	-4.79939182	99.5218351	-123.747136	825.19214
200	-4.79896723	99.5222597	-123.746795	825.19207
300	-4.79888464	99.5223423	-123.746729	825.19206

Previous studies[281, 282, 288] have modelled the current pattern in Fig. 3.1 as a series of aligned dipole moments, with one dipole in the center of each triangular current loop. However, a dipole approximation for the current loops is a very poor one for μSR, where muons sit inside the unit cell. Instead, we model the predicted current pattern by a series of infinitesimally thin wires, and sum the contribution from pairs of triangular loops, or 'butterflies'. Each butterfly has zero net dipole moment, and thus such a sum converges quickly. Table 3.1 demonstrates this fact by showing the result of finite sum estimates of the local magnetic field at the muon site as a function of N, where each sum is performed over $2N \times 2N \times 2N\frac{a}{c}$ unit cells.

In this way, we estimate that the expected local field at the muon site is approximately $825G/\mu_B$. This corresponds to a field of $41G$-$82G$ for the

range of moments ($0.05\mu_B$-$0.1\mu_B$) reported to exist in the pseudo-gap state of YBCO[281, 282].

3.5 Discussion

The results of the last two sections reveal a more than two order of magnitude discrepancy between the theoretically predicted local field and the upper bound provided by our measurements. This difference is much greater than can be reconciled by more accurately modelling the orbital order.

Moreover, it is difficult to conceive of a mechanism by which μSR might miss such order, should it exist. As discussed earlier, symmetry considerations and the simultaneous use of two sets of orthogonal counters with an initial 45° spin rotation preclude the possibility that we placed the initial muon spin direction parallel to the local field direction at every muon site. Nor does the exact muon site much matter. A map of the local fields throughout the entire unit cell shows comparably sized fields nearly everywhere in the presence of the proposed order. The few sites where the local field is zero by symmetry are already occupied by atoms, or have been explicitly eliminated as possible muon sites by previous analysis[286].

The observed spectra are also inconsistent with short-range-order. It is well known that LSCO has significant cation disorder, which in principle could destroy long-range current order in favour of a state with many small domains. However, μSR is a local probe. Even in the most extreme case where such disorder reduces the average magnetic field to zero, the local field environment would still be dominated by a distribution of fields of similar size. This would

manifest itself as a fast depolarization of the μSR asymmetry function, which would be indistinguishable from a long-range-ordered state at early times. This is demonstrated in Fig. 3.5, in which we have plotted (red) the expected asymmetry spectrum for a Gaussian distribution of local fields with a half-width of $41G$. Such a time dependence is not seen by us.

There is a real concern that the presence of the poorly screened muon charge might perturb the local system and destroy the current ordered state. Shekhter et al.[288] estimate, based on correlation effects, that the local order should be suppressed within a radius of $\sim$3 unit cells in the nearest two planes. Specific modelling by us suggests that one would still be left with a local field of $0.5G$-$1G$ at the muon site for the range of moments reported previously in YBCO. This more than ten times our experimental limit for the *smallest* reported moment. Thus, it is our opinion that muon perturbation does not reconcile our null result with theory. On this topic, we further note that STM has long observed poorly screened atomic ions directly beneath the copper-oxide planes of Bi-2212[129, 130, 289], and a corresponding suppression of superconductivity but not the pseudo-gap at these sites. Thus, the idea of a fragile pseudo-gap state which is strongly affected by electrostatic charges does not seem to be consistent with what is currently known about these systems.

Sonier et al. have reported seeing a small TRSB field in the pseudo-gap state of two YBCO crystals with μSR[290]. Recent polar Kerr effect measurements on YBCO see the onset of weak ferromagnetism at similar temperatures[291], implying a common mechanism is at work. However, the latter observation is inconsistent with the proposed circulating current pat-

tern, which has no net moment. In addition, both papers comment on the persistence of weak magnetism well above the pseudo-gap temperature.

The fields seen by Sonier et al. are comparable to the size of the error bars in the present study. Thus, we cannot comment on the presence or absence of similarly sized fields in LSCO, and this remains an open question. However, in neither case is the μSR data consistent with the current ordered state inferred from neutron scattering and ARPES measurements. Although the present study examines a different material and doping range than previous experiments, if the current pattern shown in Fig. 3.1 is a feature of a universal theory of the cuprates, it should be seen here.

It is important to note that the μSR results are not inconsistent with the more general conclusion that the pseudo-gap terminates at a QCP inside the superconducting dome. Indeed, for YBCO at least, a preponderance of evidence strongly supports such a conclusion[290, 281, 291, 282]. μSR does put tight restrictions on the form of possible pseudo-gap order parameters for LSCO. Yet, several QCP scenarios are still viable. For example, current patterns which have reflection symmetry across the Cu-O-Cu bonds would have a greatly reduced local field at the known muon site and might reconcile the μSR and neutron scattering results. Examples include the Θ_I state of Varma[163] and the 'd-density wave' state of Chakravarty[159].

Another possible route to reconcile the two experiments would be if the current pattern fluctuated between different equivalent arrangements. If the fluctuations were sufficiently rapid, the local field distribution would be motionally narrowed. With a static Gaussian distribution of $41G$ fields, a fluc-

tuation rate larger than $400MHz$ would lower the relaxation rate below our detection limit. Such a fluctuation rate could still look static on neutron scattering timescales.

It is also conceivable that slight differences in crystal structure and material parameters in different families of superconductors stabilize different current patterns. Alternatively, the magnetic order seen by neutron scattering may be secondary to an alternate pseudo-gap order parameter, and only appear in a certain subset of cuprate materials. Such questions can only be answered by further study of different materials with multiple techniques.

The present results show that any time reversal symmetry breaking fields for $La_{2-x}Sr_xCuO_4$ must be less than about $0.05G$. Any universal theory of the cuprates must take this into account.

3.6 Addendum: $HgBa_2CuO_{4+\delta}$ and $La_{1.875}Ba_{0.125}CuO_4$

In an effort to expand upon these initial results, we also explored single-crystals of two related materials: $HgBa_2CuO_{4+\delta}$ (Hg-1201) and $La_{1.875}Ba_{0.125}CuO_4$. Hg-1201 is a mono-layer cuprate system, in which time-reversal symmetry breaking order in the pseudo-gap has already been observed[18]. $La_{2-x}Ba_xCuO_4$ (LBCO) is an iso-structural compound with LSCO, but has stronger magnetic signatures than the Sr system[292]. The presence of the pseudo-gap has been confirmed in crystals of Hg-1201 with resistivity[18] and $La_{1.875}Ba_{0.125}CuO_4$ with ARPES[147].

3.6.1 $HgBa_2CuO_{4+\delta}$

A crystal of Hg-1201 with T_c=61K (p ~0.10) was grown by the group of M. Greven at Stanford University, using an encapsulated melt-growth method. Details of crystal growth and sample characterization have been previously published by that group[293, 294]. Greven et al. then performed spin-polarized neutron scattering on this crystal at the Laboratoire Leon Brillouin in Saclay, France, where they observed magnetic peaks similar to those mentioned in the introduction of this chapter below a reported T^*=372K±13K[18]. The estimated size of the ordered moment was 0.05μ_B.

ZF-μSR spectra were taken in the same apparatus as described in Section 3.2, and fields were similarly zeroed. Two successive sets of measurements were performed with the initial spin direction of the muons parallel and perpendicular to the beam direction, respectively, as illustrated in Fig. 3.7. These two sets of measurements give the same information as the experimental method laid out in Section 3.2, where four positron counters were used and the initial muon spin direction was 45° from the beam direction. Temperature was varied between 300K and 2K. We were prevented from exploring temperatures closer to T^* by the presence of epoxy seals the exterior wall of the cryostat and the dominance of muon diffusion effects in this higher temperature range.

Fig. 3.8(a) displays spectra in the B-F counters (Fig. 3.7(a)) at 290K, 100K and 2K. As with LSCO, there is no obvious precession at any temperature, but instead a weak relaxation of the muon polarization. Unlike LSCO, spectra are described by a weak exponential rather than Gaussian relaxation at all temperatures. This implies either a Lorentzian distribution of fields, typically

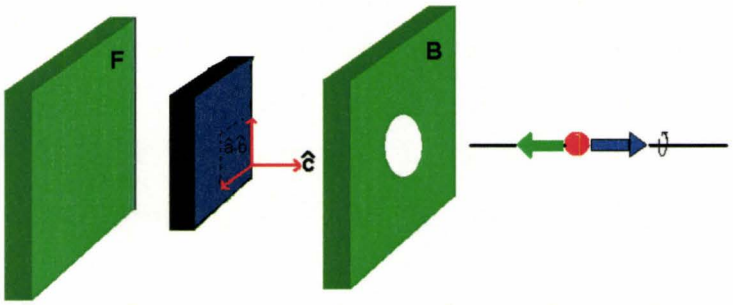

(a)

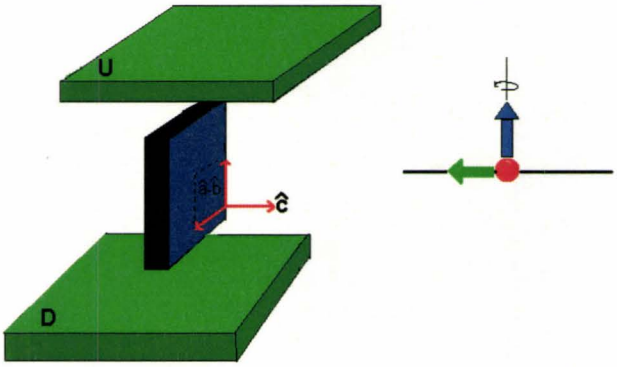

(b)

Figure 3.7: A schematic demonstrating the relative orientation of the initial spin polarization, positron detectors and crystalline axes for the ZF-μSR experiments with spin initially (a)parallel and (b)perpendicular to the beam direction.

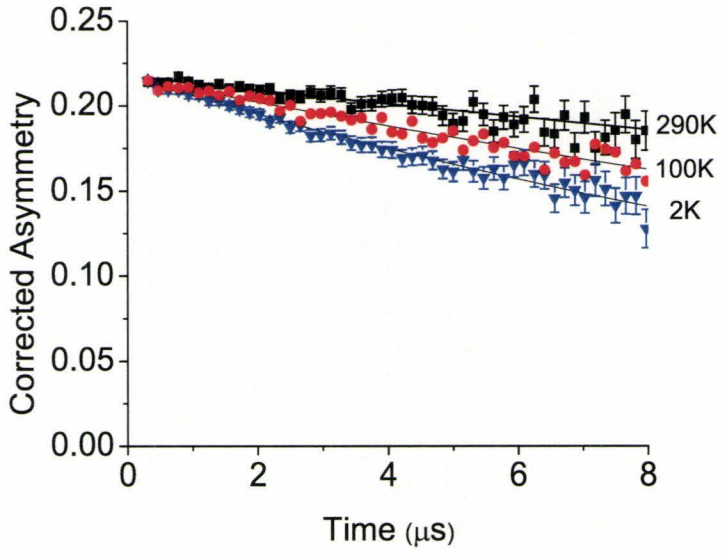

(a)

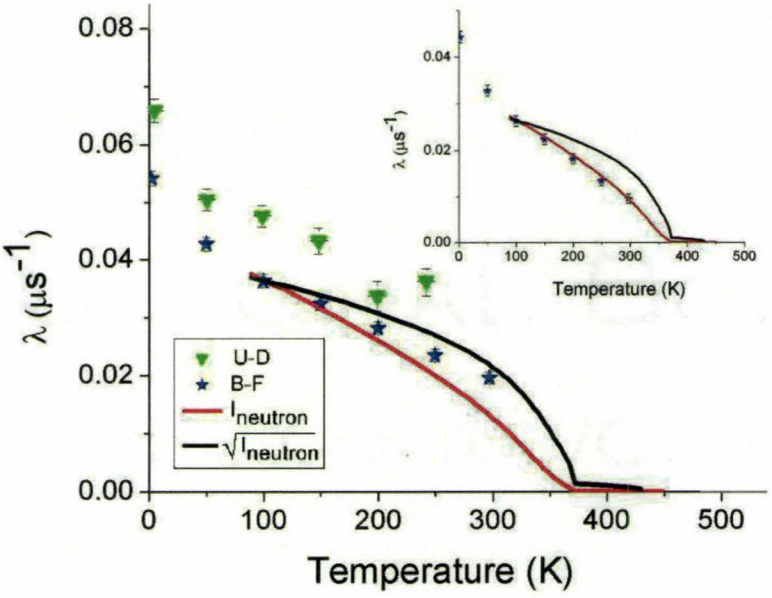

(b)

Figure 3.8: ZF-μSR data on Hg-1201 with T_c=61K. (a)Raw spectra in B-F counters at three select temperatures. Solid lines are fits to a pure exponential decay. (b)Relaxation rates of all available data. The red (black) line represents the neutron intensity (square root of neutron intensity) from Ref. [18], scaled to match the μSR relaxation rate at $100K$. (Inset)The same data as (b), but with an assumed $0.01\mu s^{-1}$ background relaxation subtracted.

seen in dilute moment systems, or a dynamic relaxation mechanism. In further contrast to LSCO, the rates of relaxation increase as temperature is decreased over the entire temperature range. Spectra from the U-D counters (Fig. 3.7(b)) look similar.

Relaxation rates were extracted by fitting to a simple exponential function:

$$A(t) = A_0 \times \exp(-\lambda t), \tag{3.3}$$

where λ is the rate of exponential relaxation. The results of these fits are plotted in Fig. 3.8(b) as a function of temperature. The rates are small, corresponding to local fields which are less than $1G$ at the muon site. The exact position of the muon site is not known for this material, and so it is not possible to make a precise estimate of the expected mean field due to the pattern shown in Fig. 3.1. However, it is reasonable to assume that such order would lead to local fields of 10-$100G$ for $0.05\mu_B$ moments, in accord with the results for LSCO. The current data is clearly inconsistent with such a prediction.

Of note is the clear linear increase of relaxation rate in Fig. 3.8(b) with decreasing temperature over the entire temperature range. The increase between $300K$ and $2K$ is $\sim 0.035\mu s^{-1}$, which corresponds to an increase of $0.4G$ in local field at the muon site. An increase in relaxation equivalent to $\sim 0.7G$ was seen in LSCO, and associated with muon diffusion. A similar mechanism may be at play here. However, we note that muon diffusion is a thermally activated process, and activation energies in other cuprates are $\sim 175K$[287]. If muons in Hg-1201 behave similarly, as seems reasonable, temperature dependent relaxation down to $2K$ is difficult to explain via diffusion alone. This suggests

another source of the temperature dependence in relaxation, perhaps related to the magnetic order which is known to exist in this crystal from neutron scattering[18].

To explore this possibility, I also plot the intensity of the magnetic neutron scattering(red line) and its square root(black line) in Fig. 3.8(b), with both lines scaled to match the B-F rate at $100K$. The μSR relaxation rate is proportional to the size of the local magnetic moment[13], whereas neutron scattering intensity of N dipoles with moment m is given by:

$$I_{neutron} \propto N \cdot m^2. \tag{3.4}$$

Thus, if both signals are the result of the same static, homogeneous ordered state, it is expected that the μSR relaxation rate should be proportional to the square root of the neutron scattering intensity. At first glance, the agreement between the relaxation rate and the black line in Fig. 3.8(b) seems reasonable for the range of temperatures where the two experiments overlap. However, the reader should note that the μSR relaxation rates are systematically lower than the black line by more than two standard deviations, and the disagreement is even greater when the neutron curve is extrapolated to low temperatures. It is also important to remember that the relaxation rates plotted in Fig. 3.8(b) contain some contribution from the randomly oriented dipoles of host nuclei. Any correction for this background will only increase the disparity. To emphasize this point, the inset of Fig. 3.8(b) shows the same data as the main panel, but corrected for an arbitrarily chosen $0.01\mu s^{-1}$ background relaxation. In this plot, the μSR relaxation rates seem to be directly proportional to the neutron scattering intensity, rather than to its square root. If confirmed, this

proportionality between μSR relaxation rate and neutron scattering intensity is significant, and difficult to justify in the context of static, homogenous order.

One possible explanation is that the magnetic order is confined to a small (<5%) fraction of the sample, and it is the volume which increases as temperature is decreased rather than the moment size. Neutron intensity depends linearly on the number of moments, which is proportional to volume, and μSR can easily mistake an increasing volume fraction for an increasing relaxation rate, if the relaxation rates and volumes were small. This is consistent with very recent reports[295] that analogous magnetic order seen in a crystal of YBCO[282] is confined to $\sim$10% of volume of that sample.

An alternate explanation is that the magnetic order is fluctuating rather than static. For example, within the narrowing limit of the strong-collision model (Section 2.1.4), the μSR asymmetry function will be purely exponential with a rate given by Eq. 2.19. If the fluctuation rate is constant, this relaxation rate is proportional to magnetic moment squared (through Δ^2), and thus neutron scattering intensity. In addition, fluctuations would also explain the smallness of the μSR relaxation rate in the presence of magnetic order. Regardless of the specific pattern, one would expect $\sim 0.1\mu_B$ moments to give local fields of 10's of Gauss. According to Eq. 2.19, a $10G$ distribution of fields can be motionally narrowed to $0.06\mu s^{-1}$ by a fluctuation rate of $4MHz$, and a $100G$ distribution of fields can be motionally narrowed to $0.06\mu s^{-1}$ by a fluctuation rate of $400MHz$. This entire range of fluctuation rates could appear static on neutron scattering timescales. This prediction can and should be tested directly by performing a LF-μSR experiment.

Much of this discussion has been speculative, and future experiments are planned to further investigate this system. In particular, we plan to monitor the ZF-μSR signal as a function of doping, in an attempt to disentangle effects of muon diffusion and pseudo-gap magnetism. Performing ZF-μSR on a crystal with T^* <300K will also allow us to quantitatively estimate relaxation in these systems due to randomly oriented nuclear dipoles, and properly correct for background. Lastly, LF-μSR experiments will allow us to test directly whether any observed magnetism is static or fluctuating on the μSR timescale.

3.6.2 $La_{1.875}Ba_{0.125}CuO_4$

A crystal of $La_{1.875}Ba_{0.125}CuO_4$ was grown via the travelling solvent floating zone furnace by G. Gu at Brookhaven National Laboratory, and cut into a thin plate with the $\hat{\mathbf{c}}$-axis perpendicular to the large face. Previous ZF-μSR measurements on this same crystal revealed an incommensurate magnetic ground state with T_N=40K[20], consistent with neutron scattering results[292].

Measurements of LBCO were taken with the setup shown in Fig. 3.7(a) at five temperatures. (Data taken in the configuration in Fig. 3.7(b) are not available.) Raw spectra for three of these temperatures are shown in Fig. 3.9(a). As with LSCO, the asymmetries are well described by a Kubo-Toyabe function, and were fit using Eq. 3.2. The resulting relaxation rates are displayed in Fig. 3.9(b), alongside those of $La_{1.87}Sr_{0.13}CuO_4$ from Section 3.3.

The high temperature relaxation rate is quite a bit smaller than that seen in LSCO. Below 250K, there is an increase in relaxation which is not seen in the Sr compound. This increase is intriguing, and it is tempting to asso-

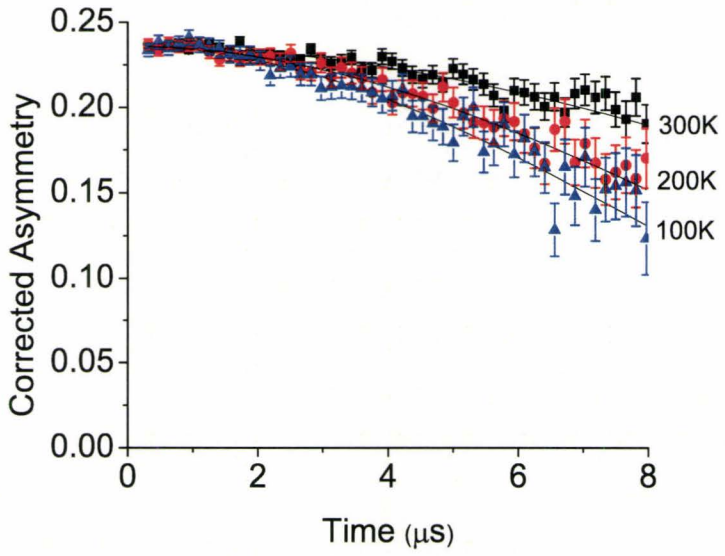

(a)

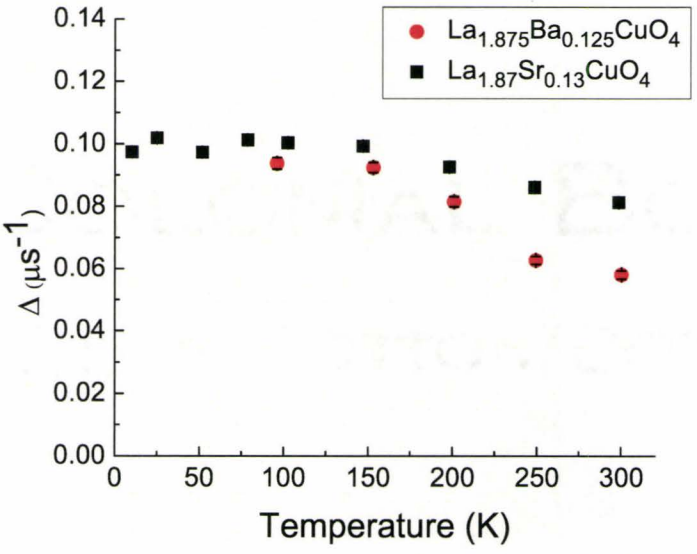

(b)

Figure 3.9: ZF-μSR data on $La_{1.875}Ba_{0.125}CuO_4$. (a)Raw spectra in B-F counters at three select temperatures. Solid lines are fits to Eq. 3.2. (b)Extracted Gaussian relaxation rates of all available data.

ciate it with pseudo-gap phenomena. Naively associating this increase with static magnetism gives a spontaneous field of $\sim 1.2G$. However, there are two significant material properties that should be mentioned.

The first is a known tetragonal-to-orthorhombic structural phase transition in this crystal, which occurs at exactly the same temperature as the increase in relaxation in Fig. 3.9(b)[296, 297, 298]. Physically, this structural phase transition corresponds to a tilting of the tetrahedra of oxygens which surround the planar copper ion. Muons in this crystal are expected to bond to the apical oxygens in these tetrahedra. An increase in μSR relaxation rate is then expected as the muons are brought closer to the copper nuclear moments in the plane. However, LSCO undergoes a similar structural phase transition at similar temperatures and with a similar magnitude of the tilt of the tetrahedra[70]. Yet, LSCO exhibits no noticeable increase in relaxation. We postulate that the muon may behave slightly differently in the two materials as a result of the dramatically different radius of Ba^{2+} (r=1.35$\mathring{A}$) and Sr^{2+} (r=1.18$\mathring{A}$) ions.

Also of note is the magnetic phase transition at T_N=40K. The increased relaxation at low temperatures could be due to the softening of magnetic fluctuations above this transition. The magnetic properties of LSCO at this doping are much weaker (e.g. see Section 3.3). As with Hg-1201, future work on this material should include μSR studies on similar materials with different numbers of carriers, as the doping dependences of T_N and the structural phase transition (or T^*) are dramatically different. Again, LF-μSR measurements should also be performed to differentiate between static and dynamic relaxation mechanisms.

3.7 Conclusions

Three separate materials have now been examined as part of an extensive effort to locate TRSB fields associated with the pseudo-gap. In none of these crystals did we find strong evidence for the long-range magnetic ordering of $\sim 0.1\mu_B$ moments below T^*, as inferred from recent neutron scattering results on YBCO and Hg-1201. This fact is the main result of the chapter.

Alone amongst the cuprates families, there exist high-quality single crystals of LSCO well-inside and well-outside the pseudo-gap state. By comparing the ZF-μSR spectra from crystals in each of these areas of the phase diagram, one circumvents debates about the definition and exact doping dependence of T^*. We observe that the ZF-μSR spectra from three crystals of LSCO are nearly identical at every temperature. This restricts TRSB fields associated with the pseudo-gap in LSCO to less than $\sim 0.05G$. The reader should compare this to the predicted field of 41-82G for the orbital current pattern in Fig. 3.1.

Additional measurements on LBCO and Hg-1201 confirm that there are no TRSB fields greater than $\sim$1-2G at any temperature. However, for each of these crystals, suggestive features in the temperature dependence of the relaxation rates warrant further investigation. In particular, future work on these materials involves comparing samples at different hole dopings, in order to clarify signal origin.

We note that, when discussing each of these materials, the possibility arose that the magnetic order was fluctuating on the μSR timescale. Future work also includes testing for magnetic dynamics explicitly using LF-μSR.

Chapter 4

Signatures of Heterogeneous Magnetism in Overdoped $La_{2-x}Sr_xCuO_4$ from μSR

This chapter incorporates the article "Signatures of Heterogeneous Magnetism in Overdoped $La_{2-x}Sr_xCuO_4$ from μSR", which has been prepared for publication in Physical Review Letters.

Signatures of Heterogeneous Magnetism in Overdoped $La_{2-x}Sr_xCuO_4$ from μSR

G. J. MacDougall,[1] A.A. Aczel,[1] R.J. Birgeneau,[2] T. Ito,[3] H. Kim,[4] S.-J. Kim,[1] J. Rodriguez,[1] P.L. Russo,[3] A.T. Savici,[3] Y.J. Uemura,[3] S. Wakimoto,[4,5] C.R. Wiebe,[1,3] and G.M. Luke[1,6]

[1]*Department of Physics and Astronomy, McMaster University, Hamilton, ON, Canada, L8S-4N3*

[2]*Department of Physics and Lawrence Berkeley Laboratory, University of California, Berkeley, CA 94720*

[3]*Department of Physics, Columbia University, New York, NY, USA, 10027*

[4]*Department of Physics, University of Toronto, Toronto, ON, Canada, M5S-1A7*

[5]*Quantum Beam Science Directorate, Japan Atomic Energy Agency, Tokai, Ibaraki, Japan 319-1195*

[6]*Canadian Institute for Advanced Research, Toronto, Ontario, Canada, M5G 1Z8*

Abstract

We present TF-μSR data on heavily overdoped LSCO, which show a large broadening of the local magnetic field distribution in response to applied magnetic field. This broadening persists up to high temperatures, well above T_c. The doping dependence is contrary to what one would expect for superconducting diamagnetism, but instead points to heterogeneous spin magnetism in these systems. This study adds to the growing list of unconventional properties in the overdoped cuprates.

4.1 Introduction

Muon spin rotation (μSR) and other local probes have now presented several examples of atomic length-scale heterogeneity in the high-T_c cuprate superconductors. Scanning Tunneling Microscopy (STM) regularly sees variations of the density of states and superconducting gap in Bi-2212 over distances of a few lattice parameters[130, 131, 135, 299, 300]. Zero-field μSR (ZF-μSR) measurements on $La_{1.88}Sr_{0.12}CuO_4$ and $La_2CuO_{4.11}$ suggest that the stripe order in these systems is fragmented and exists in 30$\AA$ islands[301]. Similar experiments on $La_{1.85-y}Eu_ySr_{0.15}CuO_4$ and $La_{2-x}Sr_xCuO_{4+y}$ observe a trade-off between static magnetism and the superconducting volume with doping[302, 303], suggesting local competition between these states.

A similar competition of states is demonstrated by the 'Swiss-cheese model' for superconductivity in Zn-doped LSCO and YBCO. This state was first discovered when TF-μSR observed a decrease in superfluid density as non-magnetic Zn ions were substituted on the planar Cu sites. This decrease was consistent with a suppression of superconductivity in an extended area around the substitution site[304], and STM studies later confirmed this interpretation[305]. Independently, several NMR studies observed a symmetric Curie-Weiss-like broadening of the local field distribution in Zn-doped YBCO, and interpreted this as a local enhancement of the staggered spin susceptibility around the dopant ions[306, 307, 308, 309, 310, 311, 312, 313, 314]. The extracted magnetic correlation length from NMR agreed well with the size of the 'holes' in the superconducting 'Swiss-cheese'. Impurity-induced moments are now well

established, and in fact are a central prediction of several theoretical studies of the cuprates[315, 316, 317, 318, 319, 320, 321, 322, 323, 324, 325, 326, 327].

Savici et al.[20] have presented TF-μSR data on crystals with fragmented stripe order, which also show a Curie-Weiss-like broadening of the local field distribution at temperatures above the ordering transition. The broadening is linear in field and, analogous to the Zn-doped systems, was associated with the staggered susceptibility of the heterogeneous spin systems. Shortly afterwards, our preliminary measurements of heavily overdoped cuprate crystals suggested that similar physics was at play in that region of the phase diagram[328]. More recently, Sonier et al. [329] observed an analogous response to applied field in a number of underdoped YBCO and LSCO crystals which correlate closely with superconducting T_c. Sonier et al. concluded that the broadening was originating from local regions of superconducting diamagnetism persisting to high temperatures. This conflict in interpretation remains unresolved, but microscopic heterogeneity is central to both pictures.

The current study expands upon the previous μSR work on LSCO[20, 328], and more carefully maps out the sample response to applied field in a series of crystals ranging from optimally to heavily overdoped. As discussed in Sec. 1.4.4, heterogeneity has been inferred from a number of studies on overdoped systems[5, 182, 183, 4, 184, 187, 114, 188, 165, 19, 65], but never observed directly. Below, we present TF-μSR data on single crystals of overdoped LSCO, which demonstrate a spatially heterogeneous local magnetic response to applied field, just as seen in the underdoped systems. The response evolves smoothly as a function of doping, suggesting that a common field-broadening

mechanism is at play across the phase diagram, and seems to grow as the system becomes progressively overdoped. This effectively eliminates any mechanism which requires superconductivity or the pseudo-gap. We conclude that the observed broadening likely originates from magnetism of a heterogenous spin system.

4.2 Experimental Details and Results

The crystals examined were grown via the travelling solvent floating zone method. LSCO crystals with x=0.15 and x=0.19 were grown at AIST in Tsukuba, and crystals with x=0.25 and x=0.30 were grown at the University of Toronto. Samples at each doping were cut into thin slabs with the $\hat{\mathbf{c}}$-axis perpendicular to the large face. Additionally, a single plate of the x=0.30 crystal was cut in the $\hat{\mathbf{a}}$-$\hat{\mathbf{c}}$ plane for tests of signal anisotropy. Details of the growth are discussed elsewhere[165, 20].

4.2.1 Bulk Susceptibility

Bulk magnetization was measured on a Quantum Design MPMS magnetometer in the two most heavily doped crystals with a field of H=5T along $\hat{\mathbf{c}}$. The results are shown in Fig. 4.1(a). As seen previously in powders[180, 90, 19], there is a small Curie component which gets larger for the higher doping. A fit of $\chi_c(x$=0.30)-$\chi_c(x$=0.25) to a Curie-Weiss temperature dependence gives a Curie constant equivalent to $0.52\mu_B$ per extra hole, which agrees with a previous estimate from powder measurements[19]. Measurements were also

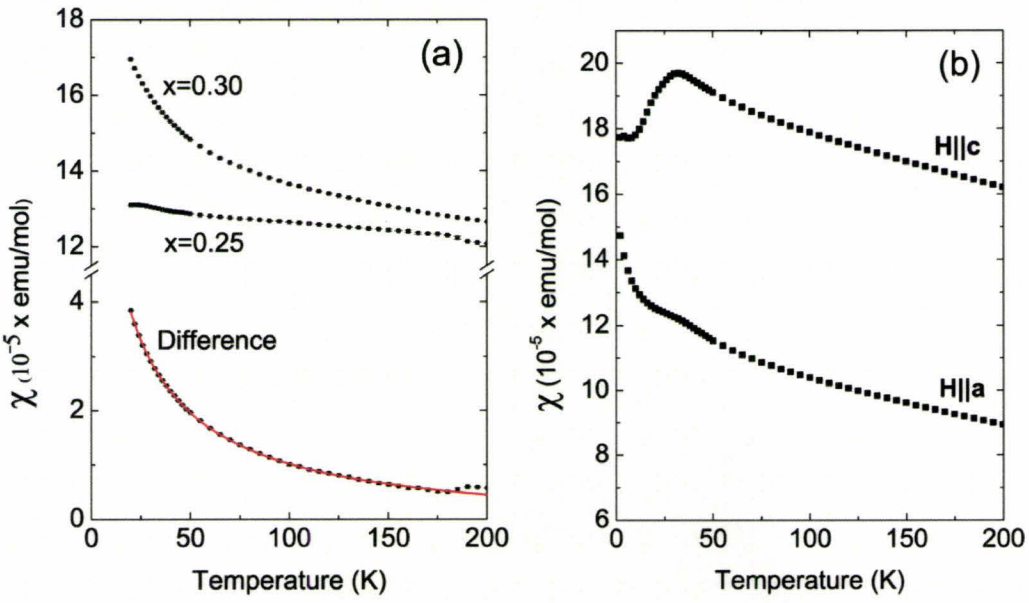

Figure 4.1: (a)Comparison of the susceptibility perpendicular to the CuO_2 planes for $La_{1.75}Sr_{0.25}CuO_4$ and $La_{1.7}Sr_{0.3}CuO_4$. The difference is fit to a Curie-Weiss temperature dependence as per Ref. [19]. (b)Magnetic susceptibility parallel and perpendicular to the CuO_2 planes in a single crystal of $La_{1.7}Sr_{0.3}CuO_4$. The signature at $30K$ is due to a superconducting impurity in a small fraction of the sample volume.

taken on the $\hat{\mathbf{a}}$-$\hat{\mathbf{c}}$ plane crystal to check for anisotropy, as shown in Fig. 4.1(b). Susceptibility χ is significantly larger for the field parallel to the $\hat{\mathbf{c}}$-axis. This can be understood to arise from the anisotropy in the Van-Vleck term of the susceptibility, as reported previously by NMR measurements of YBCO[330]. The downturn seen at 30K is due to a previously identified superconducting impurity phase, which occupies only a small fraction of the sample[165].

4.2.2 μSR

TF-μSR measurements were taken in a He-flow cryostat mounted on the HI-Time spectrometer at TRIUMF in Vancouver, Canada. Fields from $0.2T$ to $7T$ were applied perpendicular to the copper-oxide planes, and the spectra represent muon precession signals around the same axis. Applied fields were measured independently by simultaneously observing the precession of muons landing in a separate crystal of non-magnetic $Ca(CO_3)$.

The inset of Fig. 4.2 shows sample μSR spectra of $La_{1.7}Sr_{0.3}CuO_4$ in an applied field of $3T$ at one high temperature and one low temperature. One can see a dramatic increase of the relaxation of our signal with decreasing temperature. Separate measurements, discussed later, confirm that this relaxation is due to a static broadening of the local internal magnetic field distribution. The increase in relaxation rate ($\propto$ field-width) with decreasing temperature is gradual, and present in every magnetic field investigated. No analogous relaxation or any sign of order is seen in the absence of applied field.

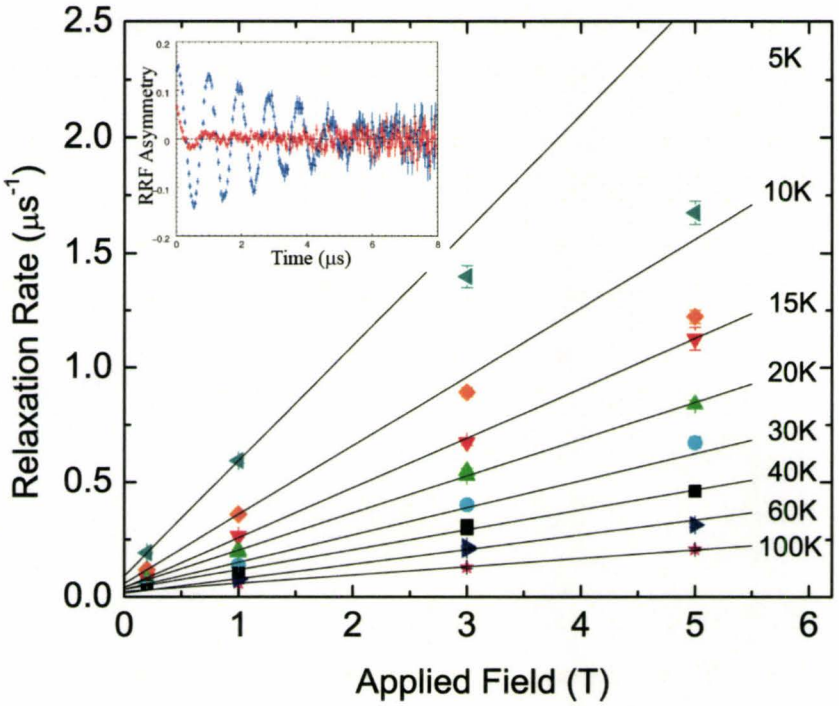

Figure 4.2: The relaxation rates in $La_{1.7}Sr_{0.3}CuO_4$ as a function of applied magnetic field. The black lines represent fits to a linear field dependence. Saturation at high fields is seen for the lowest temperatures. *Inset*: Sample spectra taken on $La_{1.7}Sr_{0.3}CuO_4$ in a field of $3T$ at $100K$ and $2K$, respectively.

In order to quantify this magnetic response, we fit all spectra to the form:

$$A(t) = A_0 \cos(\omega_\mu t + \phi) e^{-\sigma^2 t^2} e^{-\lambda t}, \tag{4.1}$$

where ω_μ is the mean precession frequency of the muons, and λ is the rate of the relaxation generated in response to the applied magnetic field. The Gaussian term in Eq. (4.1) is present to account for field broadening due to randomly oriented nuclear dipole moments. It is temperature independent, and was held constant during the fits at a value set by the high-temperature data.

The extracted values of λ are shown in Fig. 4.2 for the x=0.30 crystal. At high temperatures, the rates are roughly linear in field over the four investigated fields. The solid black curves represent fits to straight lines. The slope of these lines, dλ/dH, is analogous to the μSR 'susceptibility counterpart' as defined by Savici et al.[20], and we will argue that they represent a real measure of local spin susceptibility. Consistent with the susceptibility of polarized local moments, the relaxation rates are seen to saturate at high fields for the lowest temperatures. A similar field-reponse was seen in each of the other three crystals investigated, for all temperatures above T_c.

Fig. 4.3 plots dλ/dH as a function of temperature for LSCO crystals with x=0.30, 0.25 and 0.19. Data for the x=0.15 crystal were omitted for clarity. The temperature dependence of each is well described by:

$$\frac{d\lambda}{dH} = \frac{C}{T - \Theta} + B, \tag{4.2}$$

where C and Θ are the μSR counterparts of the Curie and Weiss constants, respectively. Inspection of the spectra for the $Ca(CO_3)$ reference crystal reveals

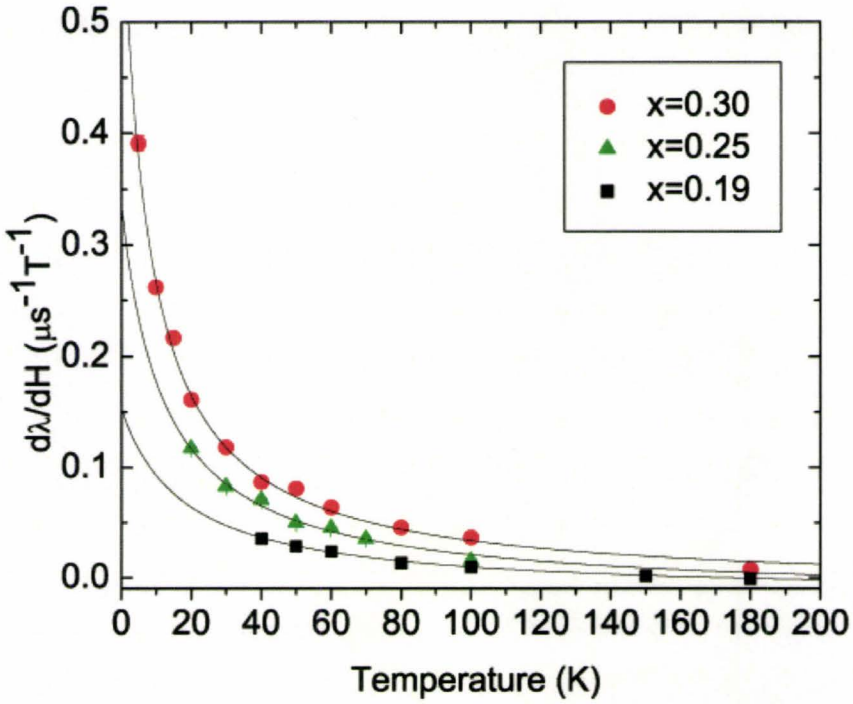

Figure 4.3: Slopes of the λ vs. H curves for the x=0.30, 0.25 and 0.19 crystals. The solid curves represents a fits to Eq. 4.2.

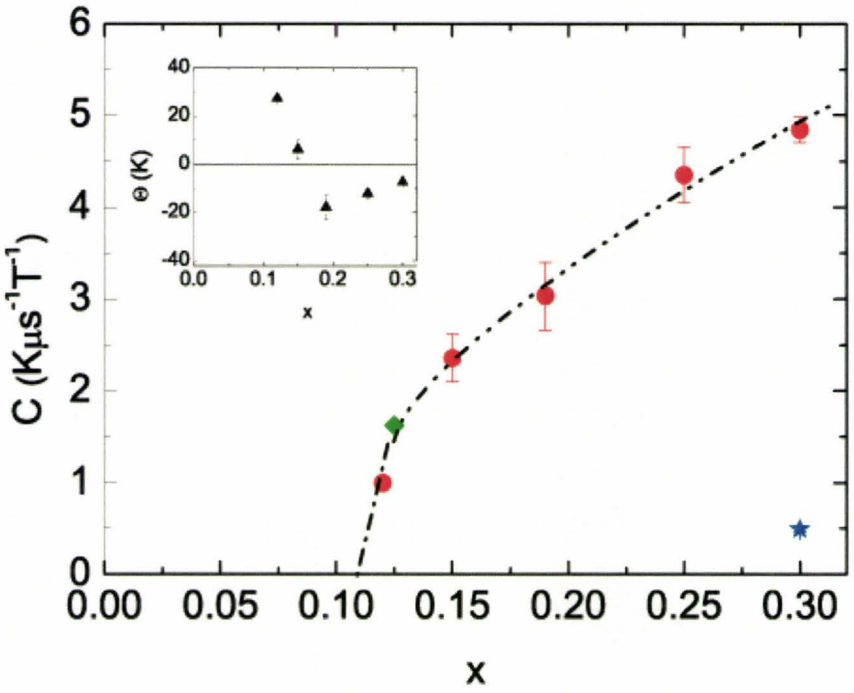

Figure 4.4: The μSR Curie constant counterpart for LSCO with $\mathbf{H}\|\hat{\mathbf{c}}$ (circles) and $La_{1.7}Sr_{0.30}CuO_4$ with $\mathbf{H}\|\hat{\mathbf{a}}$ (star), as defined in the text. Also included is the result for $La_{1.875}Ba_{0.125}CuO_4$ (diamond) first presented in Ref.[20]. The dotted line is a guide to the eye. *Inset*: The Weiss constant counterpart for LSCO.

a small, temperature-independent relaxation associated with applied-field heterogeneity. The constant, B, was included in Eq. 4.2 to account for this effect and temperature independent contributions to the local susceptibility.

The end result of the above fits is summarized in Fig. 4.4. Also included is the result for $La_{1.88}Sr_{0.12}CuO_4$ and $La_{1.875}Ba_{0.125}CuO_4$, originally reported by Savici et al[20]. The main panel shows C from Eq. 4.2 as a function of Sr concentration. One can see that the values lie on a smooth curve, and grow as the system becomes progressively overdoped. Measurements on a crystal with x=0.30 and $\mathbf{H}\|\hat{\mathbf{b}}$ reveal that the field-response is also highly anisotropic. Similar anisotropy was observed in $La_{1.875}Ba_{0.125}CuO_4$[20]. The

inset of Fig. 4.4 shows Θ from Eq. 4.2 changing sign around optimal doping and approaching zero as Sr content gets large.

4.3 Discussion

Given this collective data, it seems natural to interpret the relaxation in applied field as a measure of a local spin susceptibility. The temperature, field and orientational dependence of the current relaxations are all reminiscent of the NMR studies of Zn-doped YBCO, as well as the previous μSR results on underdoped LSCO with fragmented stripe order. The smooth evolution of the magnetic properties across the phase diagram argues against these magnetic signatures being extrinsic in origin. The high temperatures and Sr concentrations involved in the current study allow us to eliminate superconductivity and pseudo-gap effects as possible origins for the relaxation mechanisms.

In addition to TF-μSR, we also took measurements on the x=0.25 sample in the longitudinal field μSR (LF-μSR) geometry, with applied fields parallel to the initial muon spin direction. In contrast to TF-μSR, the relaxation rates in the LF-μSR geometry were statistically indistinguishable from zero at every temperature. This allows us to conclude that the relaxation in applied field seen with TF-μSR is entirely due to the static broadening of the local field distribution, and not due to field-induced dynamics. A more detailed discussion of such LF-μSR measurements is presented by Savici et al[20].

In contrast to the large increase in field-width, the *average* shift remains less than $5G$ different in every crystal for every applied field. This is significant, as it restricts viable models to explain the phenomenon. For example, one can

not simply invoke a distribution of local hole densities to explain the line-broadening in applied field, as the largest relaxation rates observed in these materials correspond to field-widths on the order of $30G$, which are impossible to create by distributing average shifts on the order of a few Gauss. The large field-width with small average shift is also contrary to what one would expect for a uniform sample response or long-range ordered state, and emphasizes the prominence of atomic-scale heterogeneity in these systems.

In such a scenario involving localized sample response, one expects the relaxation rate to be roughly proportional to the local moment. Thus, the interpretation of $\mathrm{d}\lambda/\mathrm{dH}$ as a susceptibility is a natural one. More generally, since μSR is a local probe, one must integrate over the susceptibilities at every possible wave-vector to obtain a complete formula for the relaxation rate:

$$\lambda = \int A(\mathbf{q})\chi(\mathbf{q})\, d\mathbf{q}. \tag{4.3}$$

Eq. 4.3 allows one to account for staggered ($\mathbf{q}>0$) islands of spin in addition to spins which are uniformly aligned with the applied field. The change in sign in the μSR Θ in Fig. 4.4 likely represents a shift in spin susceptibility from a distribution dominated by a staggered contribution in the underdoped materials to a one dominated by a $\mathbf{q}=0$ contribution. This interpretation is supported by the disappearance of static magnetism[331] and the emergence of a Curie-Weiss term in bulk susceptibility[4, 180, 90, 19] near the same critical doping.

The origin of this local magnetism is yet to be determined. As already discussed, random magnetic impurities are an unlikely explanation for the current phenomenon. However, there are some grounds to expect that local

moments may emerge naturally in the overdoped cuprates. Long-standing studies on excitations of La_2CuO_4 predict the emergence of a triplet band involving the Cu $3d_{3z^2-r^2}$ orbital as the Zhang-Rice band fills or apical oxygen distance decreases[332, 333]. There are existing X-ray studies that support both a decreasing apical oxygen distance[334, 335], and increased occupation of the Cu $3d_{3z^2-r^2}$ orbital upon overdoping[336, 337]. In light of the current data, we strongly suggest that these early studies be revisited.

Alternatively, it is conceivable that structural distortions around doped cations are inducing local spins, in a way that parallels the effects of Zn-doping. Recent theoretical studies on the cuprates suggest that, even for overdoped metallic systems, one would expect regions of staggered magnetization around impurities due to correlation effects[327]. In this scenario, the increase of C in Fig. 4.4 reflects the increasing number of nucleation centers for impurity-induced magnetism. The change in sign of the Weiss constant counterpart could reflect a shrinking magnetic correlation length, ξ, which would enhance the $\mathbf{q}$=0 contribution from the induced staggered islands. Indeed, the same study predicts that for x=0.30, ξ is as low as one lattice constant. This is also consistent with neutron scattering studies of LSCO, which see inelastic scattering around $\mathbf{q}=(\pi,\pi)$ become less intense and ξ shrink from greater than 600Å to a few Angstroms as one traverses the doping range explored in this study[165, 331, 338].

We emphasize the role that heterogeneity must play in any explanation of the present data. This complements previous μSR reports of microscopic phase separation in the superconducting state of overdoped cuprates[5, 185, 186],

and suggests that this heterogeneous superconductivity may condense out of a metallic analogue of the Swiss cheese state.

The data on LSCO at doping levels x <0.176 presented by Sonier et al.[329] are also well described by the phenomenology laid out in Fig. 4.4. Yet, the current study clearly points to a relaxation mechanism associated with heterogeneous magnetism rather than superconductivity. It is then very interesting that Sonier saw the field-response track superconducting T_c in YBCO. We note that this effect may simply track the normal state carrier density, as superfluid density ($\propto x$) and T_c are known to be proportional on the underdoped side of the phase diagram[69]. Alternatively, this may reflect a deeper connection between magnetism and superconductivity in the cuprates. Further study is required.

4.4 Conclusions

The local magnetic response reported in this chapter is observed over a wide range of carrier concentrations, and is significantly different from what is expected for a conventional Fermi-liquid. This points to the highly correlated nature of the cuprates, even in the heavily-overdoped regime, and must be understood for a complete description of these materials.

Chapter 5

Measurements of the Linear and Non-Linear Susceptibility of URu_2Si_2 under Hydrostatic Pressure

5.1 Introduction

An enduring mystery which surrounds the heavy fermion compound URu_2Si_2 is the nature of the hidden order state which exists below $T_{H.O.}$=17.5K in ambient pressure. As laid out in Section 1.5, this problem has inspired twenty years of research and more than a dozen theoretical proposals, yet very little has been agreed upon. Section 1.5.3 details recent efforts to limit the number of viable theories of the hidden order through a careful determination of the pressure-temperature (P-T) phase diagram. In particular, the phase diagram is currently thought to be described by one of the two pictures presented in Fig. 1.10, depending on whether or not there is a linear coupling between the hidden order parameter and the large moment antiferromagnetism (LMAF) known to exist at high pressures.

Up to this point, experimental phase diagrams have been constructed using multiple probes and often separate samples to detect each of the separate ordering transitions[258, 9, 256, 261, 10, 253]. Antiferromagnetism is usually detected with elastic neutron scattering or μSR, neither of which strongly couples to the hidden order parameter. The hidden order transition is usually defined by the location of the jump in resistivity, which typically shows no further anomalies at the antiferromagnetic transition. Moreover, as both the nature of the hidden order parameter and its coupling to resistivity are not known, it is not clear whether this definition of the hidden order transition is a favourable one. The only counterexamples to the above discussion are two thermal expansion studies[262, 263], which locate the various transitions via jumps in crystal lattice parameters, but imprecisely determine the corresponding transition temperatures.

Of further concern is the role of uniaxial strain in these studies. Yokoyama et al.[256, 10] have shown that a variation of $\eta = \frac{c}{a}$ as small as 10^{-4} is sufficient to induce LMAF. As discussed in Section 2.3, clamp cells which use mineral oil as a pressure medium are known to have a significant uniaxial component to the local strain tensor. This effect is exacerbated in the large pressure cells required for neutron scattering and μSR studies, which often have difficulties maintaining a homogeneous pressure profile. Indeed, Amitsuka et al.[261] found qualitatively different neutron scattering results for crystals inside smaller pressure cells, and Bourdarot et al.[9] noted the appearance of LMAF in a piston clamp cell at pressures where no corresponding order was found in a helium cell. This could explain the large range of critical pressures (300-700MPa) reported in the literature[258, 9, 256, 261, 10, 251, 253].

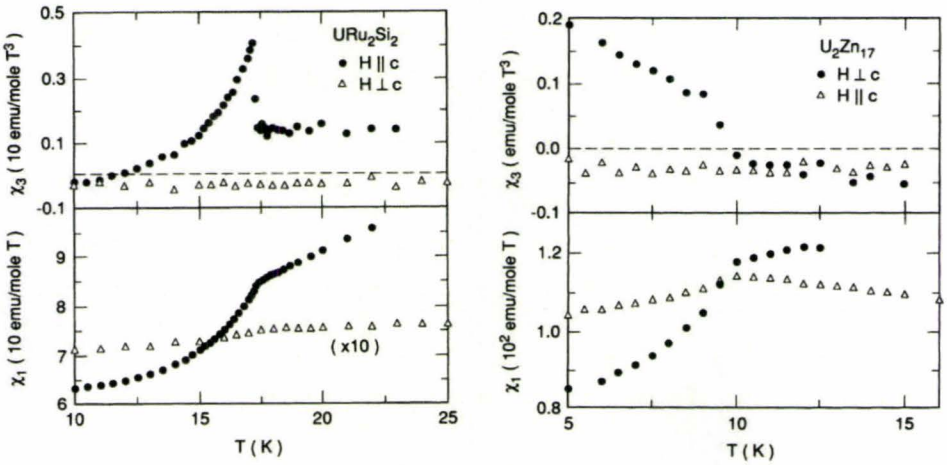

(a) (b)

Figure 5.1: The linear and cubic magnetic susceptibility of (a)URu_2Si_2 and (b)U_2Zn_{17}. From [21].

In the following pages, I develop a method of determining the P-T phase diagram of URu_2Si_2 by monitoring the pressure evolution of the linear (χ_1) and non-linear (χ_3) magnetic susceptibility. Ramirez et al. have shown that the cubic susceptibility displays a discontinuous jump at the hidden order transition[21], coincident with the kink in the linear susceptibility[224, 7]. This data is shown in Fig. 5.1(a). For comparison, Ramirez et al. also provide non-linear susceptibility data on other heavy fermion materials. Of particular interest to this present study are the measurements performed on U_2Zn_{17}, which undergoes a transition at T_N=9.7K to a collinear antiferromagnetic state with ordered moment size $m = 0.8\mu_B$[339]. As shown in Fig. 5.1(b), the linear susceptibility of this compound also exhibits a kink at T_N, but instead of a discontinuous jump, the cubic susceptibility increases smoothly with decreasing temperature, changing sign just above the transition. Building on previous

work[272], this increase was argued to represent an induced quadrupole moment driven via coupling to the ordered electronic dipoles[21].

Below, we measure the linear and non-linear magnetic susceptibility of URu_2Si_2 at several different applied pressures. At low and high pressures, we see features strongly resembling those in Fig. 5.1(a) and 5.1(b), respectively. By analogy, we argue that these features are associated with respective transitions into the hidden order and LMAF states, and use the data at all pressures to construct a P-T phase diagram. This ultimately allows us to comment on the nature of the hidden order in ambient pressure. At lower pressures, we use a helium pressure cell, in an attempt to avoid strain and pressure homogeneity concerns. At higher pressures, we use a small clamp cell, which based on previous studies[261], is expected to greatly reduce the role of strain compared to larger cells. To our knowledge, these are the first measurements of the non-linear susceptibility of URu_2Si_2 under pressure.

5.2 Experimental Methods

A single crystal of URu_2Si_2 was grown using the Czochralski method, as described elsewhere[340]. A $\sim 2mm \times 2mm \times 1mm$ piece was cut from this crystal using a specially designed spark cutting tool[341]. Magnetization, M, was measured with a Quantum Design MPMS SQUID magnetometer in 40 fields between H=0.2T and 5T, applied along the $\hat{\mathbf{c}}$-axis. The linear and cubic terms of the magnetic susceptibility were extracted by fitting the field dependence of M to Eq. 2.28, truncated at the cubic term. Attempts to include the quintic term in Eq. 2.28 did not significantly alter our conclusions.

Hydrostatic pressure was first applied using a GC10/3 Unipress Gas Pressure Cell, in conjunction with a U11 Unipress Gas Compressor assembly and using helium as the pressure medium. These components are described in more detail in Section 2.3.2. The crystal was sandwiched between two pieces of cigarette filter to maintain crystal orientation and then held in place with a thin Kapton straw. Measurements in this cell were made with applied pressures of P=14, 300, 500 and $645MPa$ over a period of two weeks. The pressure was measured as it was being applied using a resistive Mn gauge mounted on the compressor assembly. Helium solidifies at temperatures up to $50K$ for pressures up to $700MPa$; in order to ensure that the output pressure displayed on the Mn gauge reflected the true sample environment, all pressures were set at $80K$.

Higher pressures were later applied using a piston clamp cell. A detailed discussion of the exact cell design and pressurization procedure is given in Section 2.3.1. To accommodate the smaller inner diameter of this cell, a smaller piece of URu_2Si_2 was cut from the same crystal mentioned previously. Data were taken with P=$810MPa$ and $1080MPa$. Pressure was determined independently by monitoring the superconducting transition of a piece of high-purity tin, placed $\sim 17mm$ below the sample site, and employing the relation

$$T_c(P) = T_c(0) - 0.4823P + 0.0207P^2, \tag{5.1}$$

where $T_c(P)$ is the midpoint of the transition at pressure P, as per Ref. [342]. Uncertainties in the applied pressure were likewise determined by considering the width of superconducting transition.

For the latter apparatus, it was necessary to correct the raw data for the presence of the piston and other cell components near to the sample. At P=1080MPa, this was done by measuring the voltage versus position curves (See Section 2.2.2) of the empty pressure cell at a subset of fields and temperatures, linearly interpolating these data, and subtracting the resulting values from curves for the composite sample-cell system. Due to time constraints, this procedure was not repeated at P=810MPa. Instead, susceptibilities were measured only relative to values at T=10K, which assumes that the properties of the pressure cell do not change over the relevant temperature range and doubles the measurement uncertainty.

5.3 Results

Figs. 5.2 and 5.3 show data taken with P=14MPa, which is the pressure of the helium in a standard compressed gas cylinder and represents the lowest achievable pressure for the current system. P=14MPa is far from the first order transition to the LMAF phase, and data taken at this pressure is expected to be equivalent to that at ambient pressure.

Fig. 5.2 shows raw Mvs.H curves at three sample temperatures: above, slightly-below and well-below $T_{H.O.}$=17.4K. At all temperatures, the linear term in $M(H)$ dominates, and the slopes of the lines monotonically decrease with decreasing temperature. Subtracting the linear susceptibility term from M reveals a statistically significant non-linear component, which increases between high and intermediate temperatures before decreasing again at lower

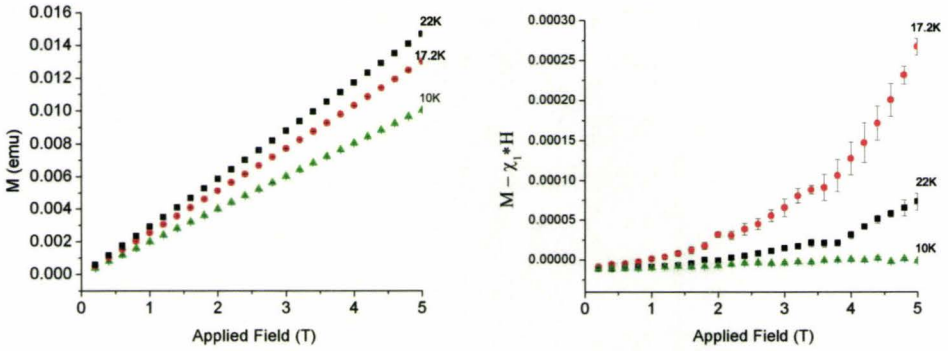

(a) (b)

Figure 5.2: (a)The magnetization versus field curves of URu_2Si_2 for three different temperatures. (b)The same curves with the linear component subtracted.

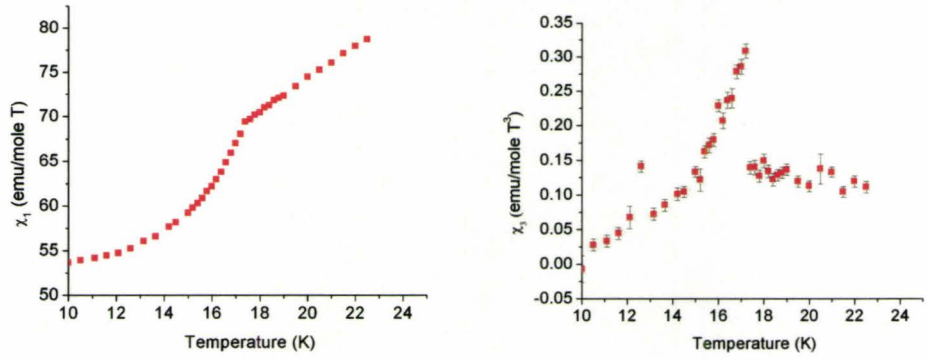

(a) (b)

Figure 5.3: The (a)linear and (b)cubic magnetic susceptibility of URu_2Si_2 as a function of temperature at a pressure P=14MPa.

temperatures. Each of these observations is consistent with the data presented by Ramirez et al. for this compound in ambient pressure[21].

Fig. 5.3 displays the extracted linear and cubic susceptibilities as a function of temperature. The values of $\chi_1(T)$ are about 15-20% smaller than those displayed in Fig. 5.1, but within the range of values reported in the literature[224, 222, 7, 21, 343]. The temperature dependence is nearly identical, with a clear kink at $T_{H.O.}$=17.4K. The values of $\chi_3(T)$ are an order of magnitude smaller than those reported by Ramirez et al.[21], but on par with those reported by others[228]. We believe discrepancy may be due to a typographical error in Ref. [21], but it could also reflect a slight misalignment of the crystalline $\hat{\mathbf{c}}$-axis with respect to the applied field, as the jump in non-linear susceptibility is highly anisotropic[21]. Again, the temperature dependence of χ_3 closely resembles that shown in Fig. 5.1, being nearly constant at high temperatures and having a clear jump at $T_{H.O.}$.

In contrast, Fig. 5.4 shows the linear and cubic susceptibility with P=1080MPa. Similar to the behaviour in ambient pressure, $\chi_1(T)$ shows a clear kink, signifying a transition at T=19.0K. Unlike in ambient pressure, $\chi_3(T)$ smoothly and continuously increases at the same temperature (noted by a purple arrow), and strongly resembles the antiferromagnetic transition of U_2Zn_{17} (Fig. 5.1(b)). Combining this fact with what is known about URu_2Si_2, we identify this transition with the onset of LMAF. For direct comparison between data in the two distinct phases, Fig. 5.4(b) also includes the values of $\chi_3(T)$ at P=14MPa, shifted such that the high temperature values of the two data sets are the same. Of particular note here is the *lack* of a discontinuous jump in the P=1080MPa

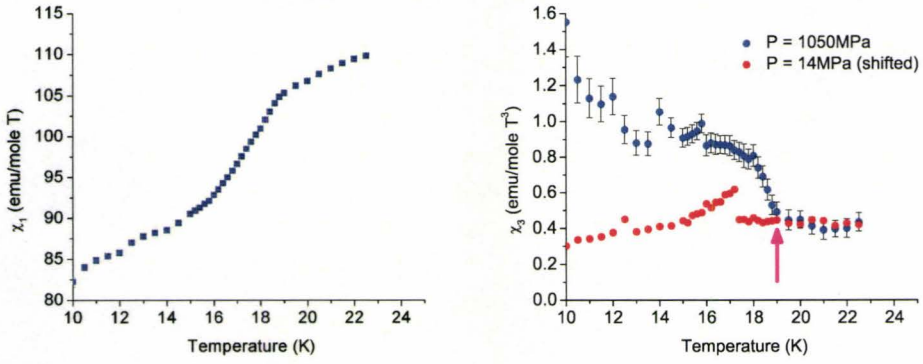

(a) (b)

Figure 5.4: The (a)linear and (b)cubic magnetic susceptibility of URu_2Si_2 as a function of temperature at a pressure P=1080MPa. Also included for comparison are cubic susceptibility data at P=14MPa. The purple arrow indicates the location of the kink in $\chi_1(T)$.

data, suggesting not only the presence of LMAF, but the *absence* of the hidden order parameter. This is discussed in more detail later.

Fig. 5.5 shows susceptibilities at P=810MPa, relative to the values at 10K. Though the error bars at this pressure are larger than for others, two successive transitions are apparent. At the upper temperature transition, there is a kink in $\chi_1(T)$ and a discontinuous jump in $\chi_3(T)$. Both are of similar magnitude to the corresponding features at P=14MPa, and are associated with the onset of hidden order. At the lower temperature transition, there is a smaller reduction in $\chi_1(T)$ and a smooth increase of $\chi_3(T)$ which is comparable to, but larger than that observed at P=1080MPa. By analogy with the higher pressure, we associate the onset of this increase with the T_N of LMAF. The suppression of $\chi_3(T)$ at the lowest temperatures is not clearly understood, but we note that the absolute size of the relative magnetization is smallest for these data.

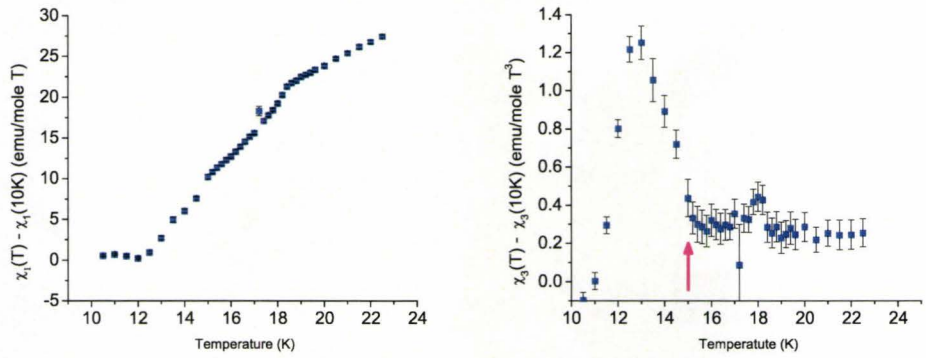

(a) (b)

Figure 5.5: The (a)linear and (b)cubic magnetic susceptibility of URu_2Si_2 as a function of temperature at a pressure P=810MPa. The purple arrow indicates the inferred LMAF transition temperature.

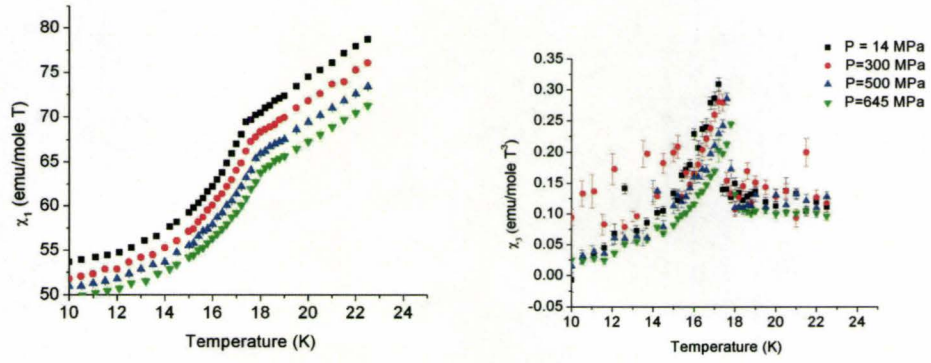

(a) (b)

Figure 5.6: The (a)linear and (b)cubic magnetic susceptibility of URu_2Si_2 as a function of temperature for four different pressures in the helium gas pressure apparatus.

The linear and cubic susceptibilities for the four lowest applied pressures is presented in Fig. 5.6. For each of these pressures, the phenomenology in this temperature range is the same as for P=14MPa. A jump in $\chi_3(T)$ is observed at the same temperature as a kink in $\chi_1(T)$, and these features are associated with a hidden order transition. The change of slope in $\chi_1(T)$ decreased slightly with pressure, while the size of the jump in $\chi_3(T)$ remains roughly constant. The transition temperature increases with increasing pressure, consistent with previous results from resistivity[344, 264]. The high temperature values of both $\chi_1(T)$, and to a lesser extent $\chi_3(T)$, slightly decrease. There is no sign of a second transition above $10K$ in any of the pressures presented in Fig. 5.6, already in contrast to all but one reported P-T phase diagram[258, 9, 256, 10, 251, 253].

The scatter in the P=300MPa data reflects the extreme sensitivity of the $\chi_3(T)$ measurements, and is suspected to be associated with the thermal inertia of the apparatus, turbulent warming of the gas during pressurization, and other non-equilibrium effects which might lead to sample conditions changing as a function of time. Similar scatter was also seen in other pressures when the cell was first pressurized and cooled. For data retaken after waiting a period of up to 8 hours after initial cooldown, the evolution of $\chi_3(T)$ was smooth and continuous at all temperatures away from the hidden order transition.

In order to test the reproducibility of our results, we repeated the measurements at P=650MPa on the same sample, remounted at a later time in the same pressure cell. To search for signs of an antiferromagnetic transition at lower temperatures, we extended our measurement range down to $4K$. The re-

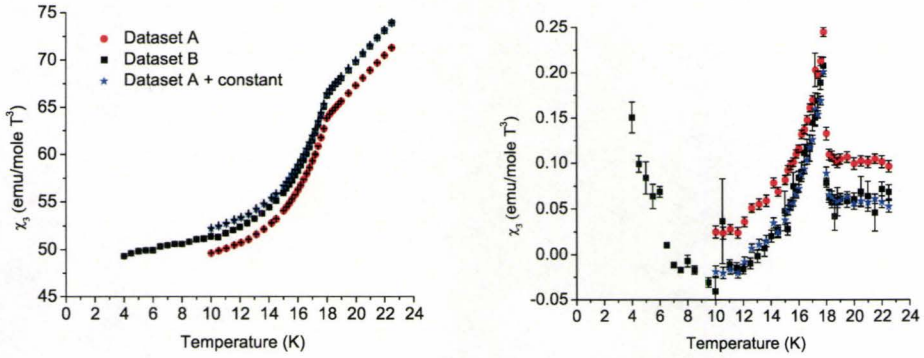

(a) (b)

Figure 5.7: A comparison of the (a)linear and (b)cubic magnetic susceptibility of URu_2Si_2 for two different datasets (shown in red and black) at P=650MPa, taken three months apart. Blue data points are the same as the red, with an added shift, such that the two data sets match perfectly at 22.5K.

sults are plotted in Fig. 5.7, alongside the initial measurements at this pressure. Though the two data sets do not perfectly match, a quick inspection reveals that they are merely offset by a temperature-independent shift. This implies that the absolute values of the linear and non-linear susceptibilities are subtly affected by crystal mounting conditions, such as the amount of dielectric material included to secure the sample position. Accordingly, my discussion below will mainly concentrate on relative features in the temperature dependence, which were reproducible.

Also of note in Fig. 5.7 is the rise in $\chi_3(T)$ at low temperatures, crossing zero at $\sim$6.5K. Although there are not enough low temperature data points to see a clear order-parameter-like temperature dependence as observed for P=1080MPa, we tentatively associate this feature with a transition into the

LMAF state. If confirmed, this is the first reported experimental evidence for LMAF in a helium pressure cell to our knowledge.

5.4 Discussion

There are several aspects of the above data that merit discussion. The first and most obvious is the dramatically different behaviour of the non-linear susceptibility upon entering the hidden order or LMAF states, as clearly demonstrated in Fig. 5.4. Although somewhat expected from the behaviour of conventional antiferromagnets, the observation of such a striking change with pressure in URu_2Si_2 is significant in itself and provides a powerful tool for exploring this system. Specifically, one gains not only the ability to track the hidden order and antiferromagnetic transition temperatures with a single probe, but an independent measure of the two order parameters in various regions of the phase diagram.

This is demonstrated in Fig. 5.8. Fig. 5.8(a) plots the pressure dependence of the jump in $\chi_3(T)$ at the upper transition, and shows that it remains roughly constant, until falling precipitously to zero between P=810MPa and 1080MPa. Conversely, the smooth increase in $\chi_3(T)$ that we associate with the onset of LMAF is seen at the upper transition line only for P=1080MPa. This is contrary to what one would expect for a system with a linear coupling between the hidden and AF order parameters (the '$\gamma \neq 0$ case'). In that case, the two regions of the P-T phase space are connected and the relative size of the two order parameters should evolve smoothly as one travels around a critical end point on the line of first order phase transitions. Instead, we see the

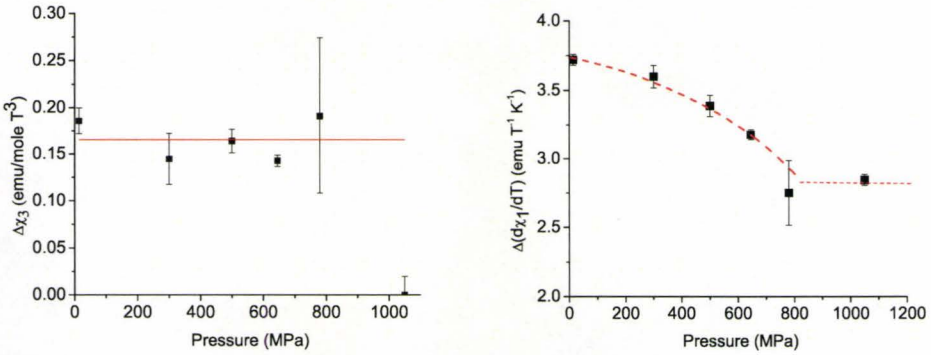

(a) (b)

Figure 5.8: (a)The size of the slope change in $\chi_1(T)$ at the upper transition of URu_2Si_2 as a function of pressure. (b)The size of the jump in $\chi_3(T)$ for transitions into the hidden order state as a function of pressure. Lines are a guide to the eye.

size of the $\chi_3(T)$ anomalies changing suddenly and dramatically. This is indicative of a bi-critical point at a pressure, P_{bc}, on the upper line of transitions, and is expected for the 'γ=0 case'.

Fig. 5.8(b) plots the change in slope of $\chi_1(T)$ at the upper transition as a function of pressure. In contrast to $\chi_3(T)$, this feature decreases in magnitude by $\sim$25% over the range of pressures examined in this study. As indicated in Fig. 5.8(b), the dependence of this quantity on pressure may also change above P_{bc}. Similar behaviour is seen in the resistivity anomaly at the upper transition[264], although a higher density of pressure points is needed to say much more.

From the collective susceptibility data, we can construct the preliminary phase diagram shown in Fig. 5.9. Here, the upper (red) data points correspond to the location of the 'kink' in $\chi_1(T)$, which for the lowest five pressures

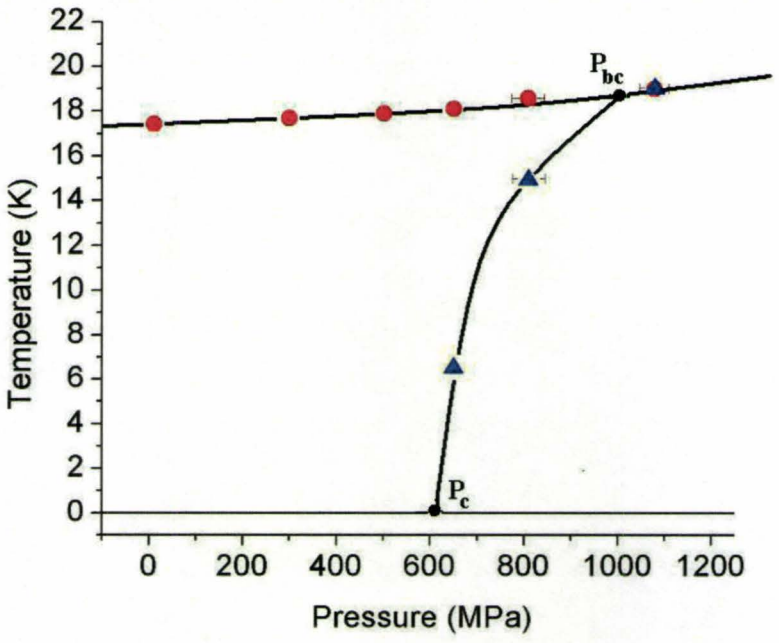

Figure 5.9: P-T phase diagram of URu_2Si_2 constructed from linear and non-linear susceptibility data.

coincides with the jump in $\chi_3(T)$. The lower (blue) data points correspond to the onset of the continuous increase in $\chi_3(T)$, which we associate with T_N. The solid lines are guides to the eye. In contrast to the phase diagram of Bourdarot et al.[9], which supported the $\gamma \neq 0$ case, we see no evidence that the lower line of transitions is continuing separately from the upper line, or ending at a critical end point. Instead, the two transitions at the highest applied pressure are coincident within our ability to resolve them, implying the existence of some $P_{bc} < 1080MPa$. Our phase diagram is then more consistent with studies which concluded γ=0 [256, 261, 10, 262, 263, 253], concurring with our findings from the pressure evolution of $\Delta\chi_3(T)$.

The bi-critical pressure in Fig. 5.9 is placed arbitrarily between $810MPa$ and $1080MPa$, as motivated by Fig. 5.8(a). However, this is significantly lower than the value of P_{bc}=$1.5GPa$ which is estimated from previous resistivity measurements[264]. The critical pressure at zero temperature, P_c, is estimated to be near $\sim 600MPa$ from the evolution of $T_N(P)$. This is quite a bit higher than most estimates of P_c[258, 9, 256, 10, 251, 253], but still smaller than the maximum value in the literature (P_c=$700MPa$)[261]. Given the small size of the pressure cells, and the smooth evolution of the data between different cells, we do not expect that uniaxial strain has played a large role in our measurements. However, Amato et al.[253] found that annealing their crystals shifted the critical and bi-critical pressure downwards by as much as $200MPa$. Thus, it is feasible that our lower critical pressures are the result of slight differences in sample preparation. The possible role of strain in the clamp cell measurements should be checked explicitly in the future by measuring susceptibility in both cells for several 'overlap pressures'.

The interpretation of the jump in $\chi_3(T)$ at $T_{H.O.}$ is still a matter of debate. The condition γ=0 restricts viable theories of the hidden order parameter to those which preserve time-reversal symmetry. The non-linear susceptibility of local moment systems can be shown to be negative in the paramagnetic state, reflecting the negative curvature of the Brillouin function, and vary as $\frac{1}{T^3}$ at high temperatures[272]. Thus, the constant, positive values of χ_3 above the respective transitions suggest that itinerant electrons supply the dominate contribution at these temperatures. Ramirez et al. also point out that the proportionality between $\chi_3(T)$ and C_V suggests that quadrupolar fluctuations are of central importance at the hidden order transition, and proposed an anisotropic spin-pairing wavefunction as the order parameter[21]. Their proposal breaks time-reversal symmetry, and is not consistent with the condition γ=0. However, our data is consistent with a proposal by Ohkawa and Shimizu[241], who suggest that the first order transition with pressure is between orderings of the quadrupolar and dipolar moments of itinerant $5f^2$ electrons. Other proposals for the hidden order parameter which are consistent with γ=0 are also possible, such as spin nematics[236] and helicity order[163].

5.5 Conclusions and Future Work

Though the data presented here are preliminary, we were able to show that the hidden order and LMAF states manifest themselves in distinctly different ways in the cubic susceptibility. By examining the pressure dependence of the transition temperatures and the magnitude of the anomalies in linear and cubic susceptibility, we were able to provide suggestive evidence that the hidden

order is the result of an order parameter which preserves time-reversal symmetry. This, in turn, implies that the small moment antiferromagnetism seen in ambient pressure is not central to the nature of the hidden order parameter, but is instead the result of pockets of the sample with large internal strain.

All the arguments presented here would benefit from an increase in point density on the pressure axis, and future work will include taking similar data for several other applied pressures. Specifically, smaller pressure steps between $500MPa$ and $1080MPa$ are desirable, both to more uniquely determine P_c and P_{bc}, and to eliminate the possibility of a critical end point on the lower transition line, which can be arbitrarily close to the upper transition. Given the concerns about uniaxial strain in piston clamp cells, it is also desirable to apply multiple pressures in both a piston clamp and a helium cell, and check for reproducibility.

Non-linear susceptibility has already proven to be a powerful tool in the quest to determine the hidden order parameter in URu_2Si_2. Future measurements of this quantity should be just as fruitful.

Chapter 6

Conclusions

Muon spin rotation/relaxation have been used to explore the normal state properties of the high-T_c cuprate superconductors $La_{2-x}Sr_xCuO_4$, and to a lesser extent, $HgBa_2CuO_{4+\delta}$ and $La_{1.875}Ba_{0.125}CuO_4$. Bulk magnetization has been used to explore the normal state of the heavy fermion superconductor URu_2Si_2. In each of these materials, the high temperature metallic state has shown unusual signatures in past measurements, particularly with probes of magnetism. Selectively tracking their magnetic properties as a function of a number of parameters (i.e. temperature, doping, applied field and pressure) has allowed us to more tightly constrain the number of viable theories to describe them. As a result, we have obtained a greater understanding of the metallic state in each system, and indirectly, the superconducting state.

In $La_{2-x}Sr_xCuO_4$, $La_{1.875}Ba_{0.125}CuO_4$ and $HgBa_2CuO_{4+\delta}$, careful ZF-μSR measurements have demonstrated that no TRSB fields greater than $\sim$1-2G can be associated with the pseudo-gap state. In particular, a careful study of the doping dependence of ZF-μSR spectra in $La_{2-x}Sr_xCuO_4$ put an upper limit of 0.05G on TRSB fields in this material. This was directly compared to the 41-82G fields, which were estimated to arise from a specific form of orbital

current order recently touted as an explanation of the pseudo-gap. Our results are clearly inconsistent with this prediction.

Related measurements on $La_{1.875}Ba_{0.125}CuO_4$ and $HgBa_2CuO_{4+\delta}$ were limited to a single doping each. The upper limit on possible TRSB fields came from the small absolute size of relaxation rates in these materials. However, in both cases, the temperature dependence of the relaxation rates was unusual, and raised the possibility that spectra were actually reflecting pseudo-gap magnetism. Of particular interest were the spectra of Hg-1201, which decayed exponentially with rates nearly proportional to neutron scattering intensity. These considerations led us to suggest that perhaps magnetism in these materials is fluctuating on the μSR timescale. Further experiments were suggested to explore this idea.

$La_{2-x}Sr_xCuO_4$ was further explored with TF-μSR as a function of applied field and doping. The resulting spectra demonstrated an anomalous, field-induced broadening of the distribution of local fields, similar to an effect which had been reported previously in underdoped cuprate systems. The present study demonstrated that this field-response persisted well into the overdoped side of $La_{2-x}Sr_xCuO_4$ phase diagram, and scaled onto simple field and temperature curves for every carrier concentration. The smooth evolution across the phase diagram implies a common field-broadening mechanism is at play, and makes it unlikely that it is a manifestation of high temperature superconducting fluctuations, as has been proposed previously. Moreover, the increase of this field-response with doping was entirely unexpected for materials which are believed by some to be approaching a canonical Fermi liquid

state, and implies at least the presence of strong electron-electron correlation effects. Particularly interesting is the extensive electronic heterogeneity in the overdoped systems, implied from a field-response in the width of local field distribution, rather than the mean field. This suggests that the heterogeneous superconductivity long suspected to exist at low temperatures has its origin in a heterogeneous metallic state at high temperatures.

Non-linear magnetization measurements were used to explore the nature of the hidden order state in URu_2Si_2. A qualitative change was seen in the temperature dependence of non-linear susceptibility, $\chi_3(T)$, between high and low pressures, which we argued by analogy reflected a transition between hidden order and antiferromagnetic ground states. By tracking certain features in $\chi_3(T)$ as a function of pressure, we were able to construct a pressure-temperature phase diagram and roughly map out the evolution of the hidden order parameter. These preliminary results support a picture where the hidden order parameter preserves time-reversal symmetry breaking, and the small moment antiferromagnetism often reported in ambient pressure is associated with regions of the sample with significant internal strain.

Bibliography

[1] M.R. Norman and C. Pepin. *Rep. Prog. Phys.*, 66:1547, 2003.

[2] M. Hashimoto, T. Yoshida, K. Tanaka, A. Fujimori, M. Okusawa, S. Wakimoto, K. Yamada, T. Kakeshita, H. Eisaki, and S. Uchida. *Phys. Rev. B*, 75:140503, 2007.

[3] M. R. Norman, D. Pines, and C. Kallin. *Adv. Phys.*, 54:715, 2005.

[4] Y. Kubo, Y. Shimakawa, T. Manako, and H. Igarashi. *Phys. Rev. B*, 43:7875, 1991.

[5] Y.J. Uemura, A. Keren, L.P Le, G.M. Luke, W.D. Wu, Y. Kubo, T. Manako, Y. Shimakawa, M. Subramanian, J.L. Cobb, and J.T. Markert. *Nature*, 364:605, 1993.

[6] C. Broholm, H. Lin, P.T. Matthews, T.E. Mason, W.J.L. Buyers, M.F. Collins, A.A. Menovsky, J.A. Mydosh, and J.K. Kjems. *Phys. Rev. B*, 43:12809, 1991.

[7] M.B. Maple, J.W. Chen, Y. Dalichaouch, T. Kohara, C. Rossel, M.S. Torikachvili, M.W. McElfresh, and J.D. Thompson. *Phys. Rev. Lett.*, 56:185, 1986.

[8] T.T.M. Palstra, A.A. Menovsky, and J.A. Mydosh. *Phys. Rev. B*, 33:R6527, 1991.

[9] F. Bourdarot, A. Bombardi, P. Burlet, M. Enderle, J. Flouquet, P. Lejay, N. Kernavanois, V.P. Mineev, L. Paolasini, M.E. Zhitomirsky, and B. Fk. *Physica B*, 359-361:986, 2005.

[10] M. Yokoyama and H. Amitsuka. *J. Phys. Soc. Jap.*, 76 Suppl. A:136, 2007.

[11] Andrei T. Savici. *Ph. D. Thesis.* Columbia University, 2004.

[12] Peter L. Russo. *Ph. D. Thesis.* Columbia University, 2005.

[13] S.L. Lee, S.H. Kilcoyne, and R. Cywinksi, editors. Scottish Universities Summer School in Physics and Institute of Physics Publishing, Bristol and Philadelphia, 1998.

[14] S.J. Blundell, P.A. Pattenden, F.L. Pratt, R.M. Valladares, T. Sugano, and W. Hayes. *Eurohys. Lett.*, 31:573, 1995.

[15] S.J. Blundell. *Contemporary Physics*, 40:175, 1999.

[16] R. Kadono, T. Matsuzaki, T. Yamazaki, S.R. Kreitzman, and J.H. Brewer. *Phys. Rev. B*, 42:6515, 1990.

[17] Mike McElfresh. *Fundamentals of Magnetism and Magnetic Measurements.* Quantum Design, 1994.

[18] Y. Li, V. Baldent, N. Barii, Y. Cho, B. Fauqu, Y. Sidis, G. Yu, X. Zhao, P. Bourges, and M. Greven. *arXiv:0805.2959*, 2008.

[19] S. Wakimoto, R.J. Birgeneau, A. Kagedan, Hyunkyung Kim, I. Swainson, K. Ymada, and H. Zhang. *Phys. Rev. B*, 72:064521, 2005.

[20] A. T. Savici, A. Fukaya, I. M. Gat-Malureau, T. Ito, P. L. Russo, Y. J. Uemura, C. R. Wiebe, P. P. Kryiakou, G. J. MacDougall, M. T. Rovers, G. M. Luke, M. Goto, S. Uchida, R. Kadono, K.Yamada, S. Takima, T. Masui, H. Eisaki, N. Kaneko, M. Greven, and G. D. Gu. *Phys. Rev. Lett.*, 95:157001, 2005.

[21] A.P. Ramirez, P. Coleman, P. Chandra, E. Brck, A.A. Menovsky, Z. Fisk, and E. Bucher. *Phys. Rev. Lett.*, 68:2680, 1992.

[22] Michael Tinkham. *Introduction to Superconductivity,* 2_{nd} *ed.* McGraw-Hill, Inc., 1996.

[23] J. Bardeen, L.N. Cooper, and J.R. Schrieffer. *Phys. Rev.*, 108:1175, 1957.

[24] F. Steglich, J. Aarts, C. D. Bredl, W. Lieke, D. Meschede, W. Franz, and H. Schfer. *Phys. Rev. Lett.*, 43:1892, 1979.

[25] J.G. Bednorz and K.A. Muller. *Z. Phys. B*, 64:189, 1986.

[26] H. Kamerlingh Onnes. *Leiden Comm.*, 120b, 122b, 124c, 1911.

[27] L.N. Cooper. *Phys. Rev.*, 104:1189, 1956.

[28] E. Maxwell. *Phys. Rev.*, 78:477, 1950.

[29] C.A. Reynolds, B. Serin, W.H. Wright, and L.B. Nesbitt. *Phys. Rev.*, 78:487, 1950.

[30] G.M. Eliashberg. *Sov. Phys.- JETP*, 11:696, 1960.

[31] L.D. Landau. *Sov. Phys. JETP*, 3:920, 1957.

[32] L.D. Landau. *Sov. Phys. JETP*, 5:101, 1957.

[33] L.D. Landau. *Sov. Phys. JETP*, 8:70, 1959.

[34] V.P. Silin. *Sov. Phys. JETP*, 6:387, 1958.

[35] J. Nozieres and L.M. Luttinger. *Phys. Rev.*, 127:1423, 1962.

[36] L.M. Luttinger and J. Nozieres. *Phys. Rev.*, 127:1431, 1962.

[37] N.F. Mott. *Proc. Phys. Soc. (London) A*, 62:416, 1949.

[38] Subir Sachdev. *Quantum Phase Transitions.* Cambridge University Press, 1999.

[39] M.R. Beasley and T.H. Geballe. *Phys. Today*, 36 (10), 1984.

[40] J. Muller. *Rep. Prog. Phys.*, 43:663, 1980.

[41] L. Gao, Y.Y. Xue, F. Chen, Q. Xiong, R.L. Meng, D. Ramirez, C.W. Chu, J.H. Eggert, and H.K. Mao. *Phys. Rev. B*, 50:4260, 1994.

[42] W.E. Pickett. *Rev. Mod. Phys.*, 61:433, 1989.

[43] P.W. Anderson. *Solid State Phys.*, 14:99, 1963.

[44] J. Rossat-Mignod, L.P. Regnault, P. Bourges, P. Burlet, C. Vettier, and J.Y. Henry. *Selected Topics Superconductivity (Frontiers in Solid State Physics 1).* Singapore: World Scientific, 1993.

[45] F.C. Zhang and T.M. Rice. *Phys. Rev. B*, 37:3759, 1988.

[46] J. Orenstein and A.J. Millis. *Science*, 288:468, 2000.

[47] P.A. Lee, N. Nagaosa, and X.-G. Wen. *Rev. Mod. Phys.*, 78:17, 2006.

[48] M. Gurvich and A.T. Fiory. *Phys. Rev. Lett.*, 59:1337, 1987.

[49] S. Martin, A.T. Fiory, R.M. Fleming, L.F. Schneemeyer, and J.V. Waszczak. *Phys. Rev. B*, 41:846, 1990.

[50] T.R. Chien Z. Wang and N. Ong. *Phys. Rev. Lett.*, 67:2088, 1991.

[51] David C. Johnston. *Phys. Rev. Lett.*, 62:957, 1989.

[52] N.E. Bickers, D.J. Scalapino, and R.T. Scalettar. *Int. J. Mod. Phys. B*, 1:687, 1987.

[53] G. Kotliar. *Phys. Rev. B*, 37:3664, 1988.

[54] G. Kotliar and J. Liu. *Phys. Rev. B*, 38:5142, 1988.

[55] F.C. Zhang, C. Gros, T.M. Rice, and H. Shiba. *Supercond. Sci. Technol.*, 1:36, 1988.

[56] W.N. Hardy, D.A. Bonn, D.C. Morgan, R. Liang, and K. Zhang. *Phys. Rev. Lett.*, 70:3999, 1994.

[57] Takashi Imai, Tadashi Shimizu, Toshinobu Tsuda, Hiroshi Yasuoka, Toshiro Takabatake, Yasuhiro Nakazawa, and Masayasu Ishikawa. *J. Phys. Soc. Jap.*, 57:1771, 1988.

[58] Z.-X. Shen, D.S. Dessau, B.O. Wells, D.M. King, W.E. Spicer, A.J. Arko, D. Marshall, L.W. Lombardo, A. Kapitulnik, P. Dickinson, S. Doniach, J. DiCarlo, T. Loeser, and C.H. Park. *Phys. Rev. Lett.*, 70:1553, 1993.

[59] R.J. Kelley, Jian Ma, C. Quitmann, G. Margaritondo, and M. Onellion. *Phys. Rev. B*, 50:590, 1994.

[60] H. Ding, J.C. Campuzano, A.F. Bellman, T. Yokoya, M.R. Norman, M. Randeria, T. Takahashi, H. Katayama-Yoshida, T. Mochiku, K. Kadowaki, and G. Jennings. *Phys. Rev. Lett.*, 74:2784, 1995.

[61] H. Ding, J.C. Campuzano, A.F. Bellman, T. Yokoya, M.R. Norman, M. Randeria, T. Takahashi, H. Katayama-Yoshida, T. Mochiku, K. Kadowaki, and G. Jennings. *Phys. Rev. Lett.*, 75:1425, 1995.

[62] D.A. Wollman, D.J. van Harlingen, W.C. Lee, D.M. Ginsberg, and A.J. Leggett. *Phys. Rev. Lett.*, 71:2134, 1993.

[63] C.C. Tsuei, J.R. Kirtley, C.C. Chi, L.S. Yu-Jahnes, A. Gupta, T. Shaw, J.Z. Sun, and M.B. Ketchen. *Phys. Rev. Lett.*, 73:593, 1994.

[64] C.C. Tsuei, J.R. Kirtley, M. Rupp, J.Z. Sun, A. Gupta, M.B. Ketchen, C.A. Wang, Z.F. Ren, J.H. Wang, and M. Bhushan. *Science*, 271:329, 1996.

[65] Yayu Wang, S. Ono, Y. Onose, G. Gu, Yoichi Ando, Y. Tokura, S. Uchida, and N.P. Ong. *Science*, 299:5603, 2003.

[66] Qijin Chen, Jelena Stajic, Shina Tan, and K. Levin. *Phys. Rep.*, 412:1, 2005.

[67] Warren E. Pickett. *arXiv:cond-mat/0603482*, 2006.

[68] Jun Nagamatsu, Norimasa Nakagawa, Takahiro Muranaka, Yuji Zenitani, and Jun Akimitsu. *Nature*, 410:63, 2001.

[69] Y.J. Uemura, G.M. Luke, B.J. Sternlieb, J.H. Brewer, J.F. Carolan, W.N. Hardy, R. Kadono, J.R. Kempton, R.F. Kiefl, S.R. Kreitzman, P. Mulhern, T.M. Riseman, D.Ll. Williams, B.X. Yang, S. Uchida, H. Takagi, J. Gopalakrishnan, A.W. Sleight, M.A. Subramanian, C.L. Chien, M.Z. Cieplak, Gang Xiao, V.Y. Lee, B.W. Statt, C.E. Stronach, W.J. Kossler, and X.H. Yu. *Phys. Rev. Lett.*, 62:2317, 1989.

[70] K. Yamada, C.H. Lee, K. Kurahashi, J. Wada, S. Wakimoto, S. Ueki, H. Kimura, Y. Endoh, S. Hosoya, G. Shirane, R.J. Birgeneau, M. Greven, M.A. Kastner, and Y.J. Kim. *Phys. Rev. B*, 57:6165, 1998.

[71] V.J. Emery, S.A. Kivelson, and O. Zachar. *Phys. Rev. B*, 56:6120, 1997.

[72] Tom Timusk and Bryan Statt. *Rep. Prog. Phys.*, 62:61, 1999.

[73] J. L. Tallon. *Physica C*, 349:53, 2001.

[74] M. Horvatic, P. Sgransan, C. Berthier, Y. Berthier, P. Butaud, J.Y. Henry, M. Couach, and J.P. Chaminade. *Phys. Rev. B*, 39:7332, 1989.

[75] W.W. Warren Jr., R.E. Walstedt, G.F. Brennert, R.J. Cava, R. Tycko, R. Bell, and G. Dabbagh. *Phys. Rev. Lett.*, 62:1193, 1989.

[76] Yohsuke Yoshinari, Hiroshi Yasuoka, Yutaka Ueda, Kei ichi Koga, and Koji Kosuge. *J. Phys. Soc. Jap.*, 59:3698, 1990.

[77] H. Alloul, T. Ohno, and P. Mendels. *Phys. Rev. Lett.*, 63:1700, 1989.

[78] R.E. Walstedt, W.W. Warren Jr., R.F. Bell, R.J. Cava, G.P. Espinosa, L.F. Schneemeyer, and J.V. Waszczak. *Phys. Rev. B*, 41:9574, 1990.

[79] R.E. Walstedt, R.F. Bell, and D.B. Mitzi. *Phys. Rev. B*, 44:7760, 1991.

[80] M. Takigawa, A.P. Reyes, P.C. Hammel, J.D. Thompson, R.H. Heffner, Z. Fisk, and K.C. Ott. *Phys. Rev. B*, 43:247, 1991.

[81] S. Ohsugi, Y. Kitaika, K. Ishida, and K. Asayama. *J. Phys. Soc. Jap.*, 60:2351, 1991.

[82] M. Bankay, M. Mali, J. Roos, and D. Brinkman. *Phys. Rev. B*, 52:6416, 1994.

[83] R. Stern, M. Mali, I. Mangelschots, J. Roos, D. Brinkman, J.-Y. Genoud, T. Graf, and J. Muller. *Phys. Rev. B*, 50:426, 1994.

[84] M.-H. Julien, P. Carretta, M. Horvatic, C. Berthier, Y. Berthier, P. Segransan, A. Carington, and D. Colson. *Phys. Rev. Lett.*, 76:4238, 1996.

[85] J.A. Martindale and P.C. Hammel. *Phil. Mag. B*, 74:573, 1996.

[86] Y. Itoh, T. Machi, A. Fukuoka, K. Tanabe, and H. Yasuoka. *J. Phys. Soc. Jap.*, 65:3751, 1996.

[87] J. Bobroff, H. Alloul, P. Mendels, V. Viallet, H.F. Marucco, and D. Colson. *Phys. Rev. Lett.*, 78:3757, 1997.

[88] Ya.-Wei Hsueh, B.W. Statt, M. Reedyk, J.S. Xue, and J.E. Greedan. *Phys. Rev. B*, 56:8511, 1997.

[89] Y. Itoh, T. Machi, N. Koshizuka, M. Murakami, H. Yamagata, and M. Matsumura. *Phys. Rev. B*, 69:184503, 2004.

[90] T. Nakano, M. Oda, C. Manabe, N. Momono, Y. Miura, and M. Ido. *Phys. Rev. B*, 49:16000, 1994.

[91] N. Curro, Z. Fisk, and D. Pines. *MRS Bulletin*, 30:442, 2005.

[92] J. Rossat-Mignod, L.P. Regnault, C. Vettier, P. Bourges, P. Burlet, J. Bossy, J.Y. Henry, and G. Lapertot. *Physica C*, 185-189:86, 1991.

[93] J.M. Tranquada, P.M. Gehring, G. Shirane, S. Shamato, and M. Sato. *Phys. Rev. B*, 46:5561, 1992.

[94] B.J. Sternlieb, J.M. Tranquada, G. Shirane, M. Sato, and S. Shamato. *Phys. Rev. B*, 50:12915, 1994.

[95] T.E. Mason, G. Aeppli, S.M. Hayden, A.P. Ramirez, and H. Mook. *Phys. Rev. Lett.*, 71:919, 1993.

[96] K. Yamada, S. Wakimoto, G. Shirane, C.H. Lee, M.A. Kastner, S. Hosoya, M. Greven, Y. Endoh, and R.J. Birgeneau. *Phys. Rev. Lett.*, 75:1626, 1995.

[97] S.M. Hayden, G. Aeppli, P. Dai, H.A. Mook, T.G. Perring, S.-W. Cheong, Z. Fisk, F. Dogan, and T. E. Mason. *Physica B*, 241-243:765, 1997.

[98] P. Bourges, L.P. Regnault, Y. Sidis, and C. Vettier. *Phys. Rev. B*, 53:876, 1996.

[99] H. Takagi, R.J. Cava, M. Marezio, B. Batlogg, J.J. Krajewski, W.F. Peck Jr., P. Bordet, and D.E. Cox. *Phys. Rev. Lett.*, 68:3777, 1992.

[100] B. Bucher, P. Steiner, J. Karpinski, E. Kaldis, and P. Wachter. *Phys. Rev. Lett.*, 70:2012, 1993.

[101] B. Batlogg, H.Y. Hwang, H. Takagi, R.J. Cava, H.L. Kao, and J. Kwo. *Physica C*, 235-240:130, 1994.

[102] T. Startseva, T. Timusk, A.V. Puchkov, D.N. Basov, H.A. Mook, M. Okuya, T. Kimura, and K. Kishio. *Phys. Rev. B*, 59:7184, 1999.

[103] T. Ito, K. Takenaka, and S. Uchida. *Phys. Rev. Lett.*, 70:3995, 1993.

[104] A. Carrington, D.J.C. Walker, A. Mackenzie, and J.R. Cooper. *Phys. Rev. B*, 48:130351, 1993.

[105] K. Takenaka, K. Mizuhashi, H. Takagi, and S. Uchida. *Phys. Rev. B*, 50:6534, 1994.

[106] A. Fukuoka, A. Tokiwa-Yamamoto, M. Itoh, R. Usami, S. Adachi, and K. Tanabe. *Phys. Rev. B*, 55:6612, 1997.

[107] T. Nakano, N. Momono, M. Oda, and M. Ido. *J. Phys. Soc. Jap.*, 67:2622, 1998.

[108] Y. Ando, S. Komiya, K. Segawa, S. Ono, and Y. Kurita. *Phys. Rev. Lett.*, 93:267001, 2004.

[109] C.C. Homes, T. TImusk, R. Liang, D.A. Bonn, and W.N. Hardy. *Phys. Rev. Lett.*, 71:1645, 1993.

[110] C.C. Home, T. Timusk, R. Liang, D.A. Bonn, and W.N. Hardy. *Physica C*, 265-280:265, 1995.

[111] S. Tajima, J. Schutzmann, and S. Miyamato. *Solid State Comm.*, 95:759, 1995.

[112] M. Reedyk, T. Timusk, J.S. Xue, and J.E. Greedan. *Phys. Rev. B*, 56:9134, 1997.

[113] D.N. Basov, H.A. Mook, B. Dabrowski, and T. Timusk. *Phys. Rev. B*, 52:R13141, 1995.

[114] S. Uchida, K. Tamasaki, and S. Tajima. *Phys. Rev. B*, 53:14558, 1996.

[115] A.V. Puchov, D.N. Basov, and T. Timusk. *J. Phys. Cond. Matt.*, 8:10049, 1996.

[116] D.N. Basov and T. Timusk. *Infrared properties of high-Tc superconductors: an experimental overview.* Amsterdam: North Holland, 1998.

[117] S.L. Cooper, G.A. Thomas, J. Orenstein, D.H. Rapkine, M. Capizzi, T. Timusk, A.J. Millis, L.F. Schneemeyer, and J.V. Waszczak. *Phys. Rev. B*, 40:11358, 1989.

[118] D.N. Basov, R. Liang, B. Dabrowski, D.A. Bonn, W.N. Hardy, and T. Timusk. *Phys. Rev. Lett.*, 77:4090, 1996.

[119] A.V. Puchkov, P. Fournier, D.N. Basov, T. Timusk, A. Kapitulnik, and N.N. Kolesnikov. *Phys. Rev. Lett.*, 77:3212, 1996.

[120] J.W. Loram, K.A. Mirza, and P.F. Freeman. *Physica C*, 171:243, 1990.

[121] J.W. Loram, K.A. Mirza, J.R. Cooper, and W.Y. Liang. *Phys. Rev. Lett.*, 71:1740, 1993.

[122] J.W. Loram, K.A. Mirza, J.R. Cooper, and W.Y. Liang anf J.M. Wade. *J. Supercond.*, 7:243, 1994.

[123] J.W. Loram, K.A. Mirza, J.R. Cooper, N. Athanassopoulou, and W.Y. Liang. Singapore: World Scientific, 1996.

[124] J.W. Loram, K.A. Mirza, J.R. Cooper, and J.L. Tallon. *Physica C*, 282-287:1405, 1997.

[125] J.W. Loram, J. Luo, J.R. Cooper, W.Y. Lianga, and J.L. Tallon. *J. Phys. Chem. Sol.*, 62:59, 2001.

[126] H.J. Tao, F. Lu, and E.J. Wolf. *Physica C*, 282-287:1507, 1997.

[127] Ch. Renner, B. Revaz, J.-Y. Genoud, K. Kadowaki, and O. Fischer. *Phys. Rev. Lett.*, 80:149, 1998.

[128] Ch. Renner, B. Revaz, K. Kadowaki, I. Maggio-Aprile, and O. Fischer. *Phys. Rev. Lett.*, 80:3606, 1998.

[129] S. H. Pan, J. P. O'Neal, R. L. Badzey, C. Chamon, H. Ding, J. R. Engelbrecht, Z. Wang, H. Eisaki, H. Eisaki, S. Uchida, A.K. Gupta, K.-W. Ng, E.W. Hudson, K.M. Lang, and J.C. Davis. *Nature*, 413:282, 2001.

[130] K. M. Lang, V. Madhavan, J. E. Hoffman, E. W. Hudson, E. Eisaki, S. Uchida, and J. C. Davis. *Nature*, 415:412, 2002.

[131] J.E. Hoffman, E.W. Hudson, K.M. Lang, V. Madhavan, H. Eisaki, S. Uchida, and J.C. Davis. *Science*, 295:466, 2002.

[132] J.E. Hoffman, K. McElroy, D.-H. Lee, K.M. Lang, H. Eisaki, S. Uchida, and J.C. Davis. *Science*, 297:1148, 2002.

[133] K. McElroy, R.W. Simmonds, J.E. Hoffman, D.-H. Lee, J. Orenstein, H. Eisaki, S. Uchida, and J.C. Davis. *Nature*, 422:592, 2003.

[134] M. Vershinin, S. Misra, S. Ono, Y. Abe, Y. Ando, and A. Yazdani. *Science*, 303:1995, 2004.

[135] K. McElroy, D.-H. Lee, J.E. Hoffman, K.M. Lang, J. Lee, E.W. Hudson, H. Eisaki, S. Uchida, and J.C. Davis. *Phys. Rev. Lett.*, 94:197005, 2005.

[136] A.G. Loesser, Z.-X. Shen, D.S. Dessau, D.S. Marshall, C.H. Park, P. Fournier, and A. Kapitulnik. *Science*, 273:325, 1996.

[137] H. Ding, T. Yokaya, J.C. Campuzano, T. Takahashi, M. Randeria, M.R. Norman, T. Mochiku, K. Kadowaki, and J. Giapinzakis. *Nature*, 382:51, 1996.

[138] J.M. Harris, A.G. Loesser, D.S. Marshall, M.C. Schabel, and Z.-X. Shen. *Phys. Rev. B*, 54:R15665, 1996.

[139] P.J. White, Z.-X. Shen, C. Kim, J.M. Harris, A.G. Loesser, P. Fournier, and A. Kapitulnik. *Phys. Rev. B*, 54:R15669, 1996.

[140] D.S. Marshall, D.S. Dessau, A.G. Loesser, C.H. Park, A.V¿ Matsuura, J.N. Eckstein, I. Boszovic, P. Fournier, A. Kapitulnik, W.E. Spicer, and Z.-X. Shen. *Phys. Rev. Lett.*, 76:4841, 1996.

[141] M.R. Norman, H. Ding, M. Randeria, J.C. Campuzano, T. Yokoya, T. Takeuchi, T. Takahashi, T. Mochiku, K. Kadowaki, P. Guptasarma, and D.G. Hinks. *Nature*, 392:157, 1998.

[142] A. Ino, C. Kim, T. Mizokawa, Z.-X. Shen, A. Fujimori, M. Takaba, K. Tamasaku, H. Eisaki, and S. Uchida. *J. Phys. Soc. Jap.*, 68:1496, 1999.

[143] T. Sato, Y. Naitoh, T. Kamiyama, T. Takahashi, T. Yokoya, K. Yamada, Y. Endoh, and K. Kadowaki. *Physica C*, 341-348:815, 2000.

[144] A. Ino, C. Kim, M. Nakamura, T. Yoshida, T. Mizokawa, A. Fujimori, Z.X. Shen, T. Kakeshita, H. Eisaki, and S. Uchida. *Phys. Rev. B*, 65:094502, 2002.

[145] J.C. Campuzano, H. Ding, M.R. Norman, H.M. Fretwell, M. Randeria, A. Kaminski, J. Mesot, T. Takeuchi, T. Sato, T. Yokoya, T. Takahashi, T. Mochiku, K. Kadowaki, P. Guptasarma, D.G. Hinks, Z. Konstantinovic, Z.Z. Li, and H. Raffy. *Phys. Rev. Lett.*, 83:3709, 1999.

[146] T. Yoshida, X.J. Zhou, K. Tanaka, W.L. Yang, Z. Hussain, Z.-X. Shen, A. Fujimori, S. Sahrakorpi, M. Lindroos, R.S. Markiewicz, A. Bansil, Seiki Komiya, Yoichi Ando, H. Eisaki, T. Kakeshita, and S. Uchida. *Phys. Rev. B*, 74:224510, 2006.

[147] T. Valla, A.V. Federov, Jinho Lee, J.C. Davis, and G.D. Gu. *Science*, 314:1914, 2006.

[148] V.J. Emery and S.A. Kivelson. *Nature*, 374:4347, 1995.

[149] M. Randeria. *Proceedings of the International School of Physics Enrico Fermi Course CXXXVI on High Temperature Superconductors.* Amsterdam, IOS Press, 1999.

[150] P.W. Anderson. *Science*, 235:1196, 1987.

[151] N. Nagaosa and P.A. Lee. *Phys. Rev. B*, 45:966, 1992.

[152] Y.S. Lee, F.C. Chou, A. Tewary, M.A. Kastner, S.H. Lee, and R.J. Birgeneau. *Phys. Rev. B*, 69:020502, 2004.

[153] A.V. Chubukov, D. Pines, and D.B. Stojkovic. *J. Phys.: Condens. Matter*, 8:10017, 1996.

[154] D. Pines. *Physica C*, 282-287:273, 1997.

[155] D. Pines. *Z. Phys. B*, 103:129, 1997.

[156] D. Pines. *arXiv:cond-mat/0002281*, 2000.

[157] D. Pines. *arXiv:cond-mat/0404151*, 2004.

[158] D. Senechal and A.-M.S. Tremblay. *Phys. Rev. Lett.*, 92:126401, 2004.

[159] Sudip Chakravarty, R. B. Laughlin, Dirk K. Morr, and Chetan Nayak. *Phys. Rev. B*, 63:094503, 2001.

[160] C. M. Varma. *Phys. Rev. B*, 55:14554, 1997.

[161] C. M. Varma. *Phys. Rev. Lett.*, 83:3538, 1999.

[162] M. E. Simon and C. M. Varma. *Phys. Rev. Lett.*, 89:247003, 2002.

[163] C. M. Varma. *Phys. Rev. B*, 73:155113, 2006.

[164] C. M. Varma and Lijun Zhu. *Phys. Rev. Lett.*, 98:177004, 2007.

[165] S. Wakimoto, H. Zhang, K. Yamada, I. Sawinson, Hyunkyung Kim, and R. J. Birgeneau. *Phys. Rev. Lett.*, 92:217004, 2004.

[166] D. Peets, J. Mottershead, B. Wu, I. Elfimov, R. Liang, W. Hardy, D. Bonn, M. Raudsepp, N. Ingle, and A. Damascelli. *New Journal of Physics*, 9:28, 2007.

[167] T. Manako, Y. Kubo, and Y. Shimakawa. *Phys. Rev. B*, 46:11019, 1992.

[168] H. L. Kao J. Kwo R. J. Cava J. J. Krajewski H. Takagi, B. Batlogg and Jr. W. F. Peck. *Phys. Rev. Lett.*, 69:2975, 1992.

[169] A.P. Mackenzie, S.R. Julian, D.C. Sinclair, and C.T. Lin. *Phys. Rev. B*, 53:5848, 1996.

[170] Cyril Proust, Etienne Boaknin, R.W. Hill, Louis Taillefer, and A.P. Mackenzie. *Phys. Rev. Lett.*, 89:147003, 2002.

[171] S.H. Naqib, J.R. Cooper, J.L. Tallon, and C. Panagopoulos. *Physica C*, 387C:365, 2003.

[172] S. Nakamae, K. Behnia, N. Mangkorntong, M. Nohara, H. Tagaki, S.J.C. Yates, and N.E. Hussey. *Phys. Rev. B*, 68:100502, 2003.

[173] A. Kaminski, S. Rosenkranz, H.M. Fretwell, Z.Z. Li, H. Raffy, M. Randeria, and M.R. Normanand J.C. Campuzano. *Phys. Rev. Lett.*, 90:207003, 2003.

[174] M. Plate, J.D.F. Mottershead, I.S. Elfimov, D.C. Peets, Ruixing Liang, D.A. Bonn, W.N. Hardy, S. Chiuzbaian, M. Falub, M. Shi, L. Patthey, and A. Damascelli. *Phys. Rev. Lett.*, 95:077001, 2005.

[175] N.E. Hussey, M. Abdel-Jawad, A. Carrington, A.P. Mackenzie, and L. Balicas. *Nature*, 425:814, 2003.

[176] Angela Kopp, Amit Ghosal, and Sudip Chakravarty. *Proc. Natl. Acad. Sci. USA*, 104:6123, 2007.

[177] H.Y. Hwang, B. Batlogg, H. Takagi, H.L. Kao, J. Kwo, R.J. Cava, J.J. Krajewski, and W.F. Peck Jr. *Phys. Rev. Lett.*, 72:2636, 1994.

[178] H. Castro and G. Deutscher. *Phys. Rev. B*, 70:174511, 2004.

[179] I. Tsukada and S. Ono. *Phys. Rev. B*, 74:134508, 2006.

[180] M. Oda, T. Nakano, Y. Kamada, and M. Ido. *Physica C*, 183:234, 1991.

[181] Takashi Kondo, Yoshimi Kubo andYuichi Shimakawa, and Takashi Manako. *Phys. Rev. B*, 50:1244, 1994.

[182] Ch. Niedermayer, C. Bernhard, U. Binninger, H. Gluckler, J.L. Tallon, E.J. Ansaldo, and J.I. Budnick. *Phys. Rev. Lett.*, 71:1764, 1993.

[183] C. Bernhard, J. L. Tallon, Th. Blasius, A. Golnik, and Ch. Niedermayer. *Phys. Rev. Lett.*, 86:1614, 2001.

[184] Y. Tanabe, T. Adachi, T. Noji, and Y. Koike. *J. Phys. Soc. Jap.*, 74:2893, 2005.

[185] Y.J. Uemura. *Solid State Comm.*, 120:347, 2001.

[186] Y.J. Uemura. *J. Phys.: Condens. Matter*, 16:S4515, 2004.

[187] J. Schutzmann, S. Tajima, S. Miyamoto, and S. Tanaka. *Phys. Rev. B*, 73:174, 1994.

[188] H.H. Wen, X.H. Chen, W.L. Yang, and Z.X. Zhao. *Phys. Rev. Lett.*, 85:2805, 2000.

[189] S. Kondo, D.C. Johnston, C.A. Swenson, F. Borsa, A.V. Mahajan, L.L. Miller, T. Gu, A.I. Goldman, M.B. Maple, D.A. Gajewski, E.J. Freeman, N.R. Dilley, R.P. Dickey, J. Merrin, K. Kojima, G.M. Luke, Y.J. Uemura, O. Chmaissem, and J.D. Jorgensen. *Phys. Rev. Lett.*, 78:3729, 1997.

[190] G.R. Stewart. *Rev. Mod. Phys.*, 56:755, 1984.

[191] Z. Fisk, D.W. Hess, C.J. Pethick, D. Pines, J.L. Smith, J.D. Thompson, and J.O. Willis. *Science*, 239:33, 1988.

[192] A.C. Hewson. Cambridge Univ. Press, Cambridge, 1993.

[193] Z. Fisk, J.L. Sarra, J.L. Smith, and J.D. Thompson. *Proc. Natl. Acad. Sci. USA*, 92:6663, 1995.

[194] G.R. Stewart. *Rev. Mod. Phys.*, 73:797, 2001.

[195] G.R. Stewart. *Rev. Mod. Phys.*, 78:743, 2006.

[196] Hilbert v. Lhneysen, Achim Rosch, Matthias Vojta, and Peter Wlfle. *Rev. Mod. Phys.*, 79:1015, 2007.

[197] C.J. Pethick and D. Pines. *Novel Superconductivity.* Plenum Press, New York, 1987.

[198] B.A. Jones, C.M. Varma, and J.W. Wilkins. *Phys. Rev. Lett.*, 61:125, 1988.

[199] I.E. Perakis, C.M. Varma, and A.E. Ruckenstein. 70:3467, 1993.

[200] G. Aeppli, E. Bucher, C. Broholm, J.K. Kjems, J. Baumann, and J. Hufnagl. *Phys. Rev. Lett.*, 60:615, 1988.

[201] R.H. Heffner, D.W. Cooke, A.L. Giorgi, R.L. Hutson, M.E. Schillaci, H.D. Rempp, J.L. Smith, J.O. Willis, D.E. MacLaughlin, C. Boekema, R.L. Lichti, J. Oostens, and A.B. Denison. *Phys. Rev. B*, 39:11345, 1989.

[202] C. Broholm, J.K. Kjems, W.J.L. Buyers, P. Matthews, T.T.M. Palstra, A.A. Menovsky, and J.A. Mydosh. *Phys. Rev. Lett.*, 58:1467, 1987.

[203] T.E. Mason, B.D. Gaulin, J.D. Garrett, Z. Tun, W.J.L. Buyers, and E.D. Isaacs. *Phys. Rev. Lett.*, 65:3189, 1990.

[204] J.D. Thompson, R. Movshovich, Z. Fisk, F. Bouquet, N.J. Curro, R.A. Fisher, P.C. Hammel, H. Hegger, M.F. Hundley, M. Jaime, P.G. Pagliuso, C. Petrovic, N.E. Phillips, and J.L. Sarrao. *J. Magn. Magn. Mater.*, 226-230:5, 2001.

[205] C. Broholm, J.K. Kjems, G. Aeppli, Z. Fisk, J.L. Smith, S.M. Shapiro, G. Shirane, and H.R. Ott. *Phys. Rev. Lett.*, 58:2003, 1987.

[206] G. Aeppli, A. Goldman, G. Shirane, E. Bucher, and M.-Ch. Lux-Steiner. *Phys. Rev. Lett.*, 58:808, 1987.

[207] G. Aeppli, H. Yoshizawa, Y. Endoh, E. Bucher, J. Hufnagl, Y. Onuki, and T. Komatsubara. *Phys. Rev. Lett.*, 57:122, 1986.

[208] H.R. Ott, H. Rudigier, Z. Fisk, and J.L. Smith. *Phys. Rev. Lett.*, 50:1595, 1983.

[209] G.R. Stewart, Z. Fisk, J.O. Willis, and J.L. Smith. *Phys. Rev. Lett.*, 52:679, 1984.

[210] B.S. Shivaram, J.J. Gannon, and D.G. Hinks. *Phys. Rev. Lett.*, 63:1723, 1989.

[211] G. Bruls, D. Weber, B. Wolf, B. Luthi, A.A. Menovsky, A. de Visser, and J.J.M. Franse. *Physica B*, 165-166:369, 1990.

[212] H.R. Ott, H. Rudigier, E. Felder, Z. Fisk, and J.L. Smith. *Phys. Rev. B*, 33:126, 1986.

[213] J.L. Smith, Z. Fisk, J.O. Willis, H.R. Ott, S.E. Lambert, Y. Dalichaouch, and M.B. Maple. *J. Magn. Magn. Mater.*, 63-64:464, 1987.

[214] R. H. Heffner, J. L. Smith, J. O. Willis, P. Birrer, C. Baines, B. Hitti F. N. Gygax, E. Lippelt, H. R. Ott, A. Schenck, E. A. Knetsch, J. A. Mydosh, and D. E. MacLaughlin. *Phys. Rev. Lett.*, 65:2816, 1990.

[215] G. M. Luke, A. Keren, L. P. Le, W. D. Wu, Y. J Uemura, D. A. Bonn, L. Taillefer, and J. D. Garrett. *Phys. Rev. Lett.*, 71:1466, 1993.

[216] Y. Aoki, A. Tsuchiya, T. Kanayama, S. R. Saha, H. Sugawara, H. Sato, W. Higemoto, A. Koda, K. Ohishi, K. Nishiyama, and R. Kadono. *Phys. Rev. Lett.*, 91:067003, 2003.

[217] D.J. Bishop, C.M. Varma, B. Batlogg, E. Bucher, Z. Fisk, and J.L. Smith. *Phys. Rev. Lett.*, 53:1009, 1984.

[218] D. Einzel, P.J. Hirschfeld, F. Gross, B.S. Chandrasekhar, K. Andres, H.R. Ott, J. Beuers, Z. Fisk, and J.L. Smith. *Phys. Rev. Lett.*, 56:2513, 1986.

[219] A. Sulpice, P. Gandit, J. Chaussy, J. Flouquet, D. Jaccard, P. Lejay, and J.L. Tholence. *J. Low Temp. Phys.*, 62:39, 1986.

[220] B.S. Shivaram, Y.H. Jeong, T.F. Rosenbaum, and D.G. Hinks. *Phys. Rev. Lett.*, 56:1078, 1986.

[221] R.H. Heffner and M.R. Norman. *Condensed Matter Physics*, 17:361, 1996.

[222] W. Schlabitz, J. Baumann, B. Pollit, U. Rauchschwalbe, H.M. Mayer, U. Ahlheim, and C.D. Bredl. *Z. Phys. B*, 62:171, 1986.

[223] Y. Kasahara, T. Iwasawa, H. Shishido, T. Shibauchi, K. Behnia, Y. Haga, T.D. Matsuda, Y. Onuki, M. Sigrist, and Y. Matsuda. *Phys. Rev. Lett.*, 99:116402, 2007.

[224] T.T.M. Palstra, A.A. Menovsky, J. van den Berg, A.J. Dirkmaat, P.H. Kes, G.J. Nieuwenhuys, and J.A. Mydosh. *Phys. Rev. Lett.*, 55:2727, 1985.

[225] A. de Visser, F.E. Kayzel, A.A. Menovsky, J.J.M. Franse, J. van den Berg, and G.J. Nieuwenhuys. *Phys. Rev. B*, 34:R8168, 1986.

[226] K. Behnia, R. Bel, Y. Kasahara, Y. Nakajima, H. Jin, H. Aubin, K. Izawa, Y. Matsuda, J. Flouquet, Y. Haga, Y. Onuki, and P. Lejay. *Phys. Rev. Lett.*, 94:156405, 2005.

[227] P.A. Sharma, N. Harrison, M. Jaime, Y.S. Oh, K.H. Kim, C.D. Batista, H. Amitsuka, and J.A. Mydosh. *Phys. Rev. Lett.*, 97:156401, 2006.

[228] Y. Miyako, S. Kawarazaki, H. Amitsuka, C.C. Paulsen, and K. Hasselbach. *J. Appl. Phys.*, 70:5791, 1991.

[229] E.D. Isaacs, D.B. McWhan, R.N. Kleiman, D.J. Bishop, G.E. Ice, P. Zschack, B.D. Gaulin, T.E. Mason, J.D. Garrett, and W.J.L. Buyers. *Phys. Rev. Lett.*, 65:3185, 1990.

[230] W.J.L. Buyers. *Physica B*, 223:9, 1996.

[231] O.O. Bernal, C. Rodrigues, A. Martinez, H.G. Lukefahr, D.E. MacLaughlin, A.A. Menovsky, and J.A. Mydosh. *Phys. Rev. Lett.*, 87:196402, 2001.

[232] D.E. MacLaughlin, D.W. Cooke, R.H. Heffner, R.L. Hutson, M.W. McElfresh, M.E. Schillaci, H.D. Rempp, J.L. Smith, J.O. Willis, E. Zirngiebl, C. Boekema, R.L. Lichti, and J. Oostens. *Phys. Rev. B*, 37:3153, 1988.

[233] U. Walter, C.-K. Loong, M. Loewenhaupt, and W. Schlabitz. *Phys. Rev. B*, 33:7875, 1986.

[234] C.R. Wiebe, G.M. Luke, Z. Yamani, A.A. Menovsky, and W.J.L. Buyers. *Phys. Rev. B*, 69:132418, 2004.

[235] C.R. Wiebe, J.A. Janik, G.J. MacDougall, G.M. Luke, J.D. Garrett, H.D. Zhou, Y.-J. Jo, L. Balicas, Y. Qiu, J.R.D. Copley, Z. Yamani, and W.J.L. Buyers. *Nature Physics*, 3:522, 2007.

[236] V. Barzykin and L.P. Gor'kov. *Phys. Rev. Lett.*, 70:2479, 1993.

[237] P. Chandra, P. Coleman, J.A. Mydosh, and V. Tripathi. *Nature*, 417:831, 2002.

[238] V. Tripathi, P. Chandra, and P. Coleman. *J. Phys.: Condens. Matter*, 17:5285, 2005.

[239] P. Santini and G. Amoretti. *Phys. Rev. Lett.*, 73:1027, 1994.

[240] P. Santini. *Phys. Rev. B*, 57:5191, 1998.

[241] Fusayoshi J. Ohkawa and Hirofumi Shimizu. *J. Phys.: Condens. Matter*, 11:L519, 1999.

[242] A. Kiss and P. Fazekas. *Phys. Rev. B*, 71:054415, 2005.

[243] L.P. Gor'kov and A. Sokol. *Phys. Rev. Lett.*, 69:2586, 1992.

[244] D.F. Agterberg and M.B. Walker. *Phys. Rev. B*, 50:563, 1994.

[245] Y. Okuno and K. Miyake. *J. Phys. Soc. Jap.*, 67:2469, 1998.

[246] A.E. Sikkema, W.J.L. Buyers, I. Affleck, and J. Gan. *Phys. Rev. B*, 54:9322, 1996.

[247] H. Ikeda and Y. Ohashi. *Phys. Rev. Lett.*, 81:3723, 1998.

[248] V.P. Mineev and M.E. Zhitomirsky. *Phys. Rev. B*, 72:014432, 2005.

[249] H. Amitsuka, M. Sato, N. Metoki, M. Yokoyama, K. Kuwahara, T. Sakakibara, H. Morimoto, S. Kawarazaki, Y. Miyako, and J.A. Mydosh. *Phys. Rev. Lett.*, 83:5114, 1999.

[250] K. Matsuda, Y. Kohori, T. Kohara, K. Kuwahara, and H. Amitsuka. *Phys. Rev. Lett.*, 87:087203, 2001.

[251] K Matsuda, Y Kohori, T Kohara, H Amitsuka, K Kuwahara, and T Matsumoto. *J. Phys.:Condens. Matter*, 15:2363, 2003.

[252] H. Amitsuka, K. Tenya, M. Yokoyama, A. Schenck, D. Andreica, F.N. Gygax, A. Amato, Y. Miyako, Ying Kai Huang, and J.A. Mydosh. *Physica B*, 326:418, 2003.

[253] A. Amato, M.J. Graf, A. de Visser, H. Amitsuka, D. Andreica, and A. Schenck. *J. Phys.: Condens. Matter*, 16:S4403, 2004.

[254] G.M. Luke et al. Private communication. 2002.

[255] P. Chandra, P. Coleman, and J.A. Mydosh. *cond-mat/0110048*, 2001.

[256] M. Yokoyama, H. Amitsuka, K. Tenya, K. Watanabe, S. Kawarazaki, H. Yoshizawa, and J.A. Mydosh. *Phys. Rev. B*, 72:214419, 2005.

[257] G.M. Luke, A. Keren, L.P. Le, Y.J. Uemura, W.D. Wu, D. Bonn, L. Taillefer, J.D. Garrett, and Y. O-nuki. *Hyperfine Int.*, 85:397, 1994.

[258] F. Bourdarot, B. Fk, V.P. Mineev, M.E. Zhitomirsky, N. Kernavanois, S. Raymond, F. Lapierre, P. Lejay, and J. Flouquet. *Physica B*, 350:179, 2004.

[259] N. Shah, P. Chandra, P. Coleman, and J.A. Mydosh. *Phys. Rev. B*, 61:564, 2000.

[260] F. Bourdarot, B. Fk, K. Habicht, and K. Proke. *Phys. Rev. Lett.*, 90:067203, 2003.

[261] H. Amitsuka, K. Matsuda, I. Kawasaki, K. Tenya, M. Yokoyama, C. Sekine, N. Tateiwa, T.C. Kobayashi, S. Kawarazaki, and H. Yoshizawa. *J. Magn. Magn. Mater.*, 310:214, 2007.

[262] Gaku Motoyama, Takashi Nishioka, and Noriaki K. Sato. *Phys. Rev. Lett.*, 90:166402, 2003.

[263] Shinji Uemura, Gaku Motoyama, Yasukage Oda, Takashi Nishioka, and Noriaki K. Sato. *J. Phys. Soc. Jap.*, 74:2667, 2005.

[264] J.R. Jeffries, N.P. Butch, B.T. Yukich, and M.B. Maple. *Phys. Rev. Lett.*, 99:217207, 2007.

[265] J. Chappert and R.I. Grynszpan, editors. *Muons and Pions in Materials Research.* North-Holland Physics Publishing, 1984.

[266] A. Schenck. *Muon Spin Rotation Spectroscopy: Principles and Applications in Solid State Physics.* Adam Hilger Ltd., Bristol and Boston, 1985.

[267] Tanya Maria Riseman. *Ph. D. Thesis.* The University of British Columbia, 1993.

[268] A. Abragam. *The Principles of Nuclear Magnetism.* Oxford University Press, Oxford, 1961.

[269] Charles Kittel. *Introduction to Solid State Physics,* 7^{th} *ed.* John Wiley and Sons, Inc., 1996.

[270] Neil W. Ashcroft and N. David Mermin. *Solid State Physics.* Thomas Learning, Inc., 1976.

[271] P. Morin and D. Schmitt. *Phys. Lett.*, 73A:67, 1979.

[272] P. Morin and D. Schmitt. *Phys. Rev. B*, 23:5936, 1981.

[273] A.P. Ramirez, P. Chandra, P. Coleman, Z. Fisk, J.L. Smith, and H.R. Ott. *Phys. Rev. Lett.*, 73:3018, 1994.

[274] D. Jaccard, K. Behnia, and J. Sierro. *Phys. Lett. A*, 163:475, 1992.

[275] S.S. Saxena, P. Agarwal, K. Ahilan, F.M. Grosche, R.K.W. Haselwimmer, M.J. Steiner, E. Pugh, I.R. Walker, S.R. Julian, P. Monthoux, G.G. Lonzarich, A. Huxley, I. Sheikin, D. Braithweite, and J. Flouquet. *J. Magn. Magn. Mater.*, 226-230:45, 2001.

[276] Y. Uwatoko, T. Hotta, E. Matsuoka, H. Mori, T. Ohki, J.L. Sarrao, J.D. Thompson, N. Mori, and G. Oomi. *Rev. High Pressure Sci. Technol.*, 7:1508, 1998.

[277] A. Kaminski, S. Rosenkranz, H. Fretwell, J. C. Campuzano, Z. Li, H. Raffy, W. G. Cullen, H. You, C. G. Olson, C. M. Varma, and H. Hoechst. *Nature*, 416:610, 2002.

[278] N. P. Armitage and Jiangping Hu. *arXiv:cond-mat/0303186*, 2003.

[279] J. P. Castellan, B. D. Gaulin, H. A. Dabkowska, A. Nabialek, G. Gu, X. Liu, and Z. Islam. *Phys. Rev. B*, 73:174505, 2006.

[280] S. V. Borisenko, A. A. Kordyuk, A. Koitzsch, T. H. Kim, K. A. Nenkov, M. Knupfer, J. Fink, C. Grazioli, S. Turchini, and H. Berger. *Phys. Rev. Lett.*, 92:207001, 2004.

[281] B. Fauque, Y. Sidis, V. Hinkov, S. Pailhes, C. T. Lin, X. Chaud, and P. Bourges. *Phys. Rev. Lett.*, 96:197001, 2006.

[282] H.A. Mook, Y. Sidis, B. Fauque, V. Baledent, and P. Bourges. *arXiv:0802.3620*, 2008.

[283] Y. Sidis, B. Fauque, V. Aji, and P. Bourges. *cond-mat/0610614*, 2006.

[284] Vivek Aji and C. M. Varma. *cond-mat/0605468*, 2007.

[285] G. M. Luke, Y. Fudamoto, K. M. Kojima, M. I. Larkin, J. Merrin, B. Nachumi, Y. J. Uemura, Y. Maeno, Z. Q. Mao, Y. Mori, H. Nakamura, and M. Sigrist. *Nature*, 394:558, 1998.

[286] B. Hitti, P. Birrer, K. Fischer, F. N. Gygax, E. Lippelt, H. Maletta, A. Schenck, and M. Weber. *Hyperfine Int.*, 63:287, 1990.

[287] J. E. Sonier, J. H. Brewer, R. F. Kiefl, R. H. Heffner, K. F. Poon, S. L. Stubbs, G. D. Morris, R. I. Miller, W. N. Hardy, R. Liang, D. A. Bonn, J. S. Gardner, C. E. Stronach, and N. J. Curro. *Phys. Rev. B*, 66:134501, 2002.

[288] Arkady Shekhter, Lei Shu, Vivek Aji, D. E. MacLaughlin, and C. M. Varma. *arXiv:0802.2972*, 2008.

[289] H. Mashima, N. Fukuo, Y. Matsumoto, G. Kinoda, T. Kondo, H. Ikuta, T. Hitosugi, and T. Hasegawa. *Phys. Rev. B*, 73:060502, 2006.

[290] J. E. Sonier, J. H. Brewer, R. F. Kiefl, R. I. Miller, G. D. Morris, C. E. Stronach, J. S. Gardner, S. R. Dunsiger, D. A. Bonn, W. N. Hardy, R. Liang, and R. H. Heffner. *Science*, 292:1692, 2001.

[291] J. Xia, E. Schemm, G. Deutscher, S. A. Kivelson, D. A. Bonn, W. N. Hardy, R. Liang, W. Siemons, G. Koster, M. M. Fejer, and A. Kapitulnik. *cond-mat/0711.2494v1*, 2007.

[292] J. M. Tranquada, H. Woo, T.G. Perring, H. Goka, G.D. Gu, G. Xu, M. Fujita, and K. Yamada. *Nature*, 429:534, 2002.

[293] X. Zhao, G. Yu, Y.-C. Cho, G. Chabot-Couture, N. Barii, P. Bourges, N. Kaneko, Y. Li, L. Lu, E. M. Motoyama, O. P. Vajk, and M. Greven. *Adv. Mat.*, 18:3243–3247, 2006.

[294] E. van Heumen, R. Lortz, A.B. Kuzmenko, F. Carbone, D. van der Marel, X. Zhao, G. Yu, Y. Cho, N. Barisic, M. Greven, C.C. Homes, and S.V. Dordevic. *Phys. Rev. B*, 75:054522, 2007.

[295] J.E. Sonier. Private communication. 2008.

[296] J.D. Axe, A.H. Moudden, D. Hohlwein, D.E. Cox, K.M. Mohanty, A.R. Moodenbaugh, and Youwen Xu. *Phys. Rev. Lett.*, 62:2751, 1989.

[297] T. Adachi, T. Noji, and Y. Koike. *Phys. Rev. B*, 64:144524, 2001.

[298] Y. Zhao, B.D. Gaulin, J.P. Castellan, J.P.C. Ruff, S.R. Dunsiger, G.D. Gu, and H.A. Dabkowska. *Phys. Rev. B*, 76:184121, 2007.

[299] K. McElroy, Jinho Lee, J.A. Slezak, D.-H. Lee, H. Eisaki, S. Uchida, and J.C. Davis. *Science*, 309:1049, 2005.

[300] Jinho Lee, James A. Slezak, and J.C. Davis. *J. Phys. Chem. Solids*, 66:1370, 2005.

[301] A. T. Savici, Y. Fudamoto, I.M. Gat, M.I. Larkin, Y.J. Uemura, G.M. Luke, K.M. Kojima, Y.S. Lee, M.A. Kastner, R.J. Birgeneau, and K. Yamada. *Phys. Rev. B*, 66:014524, 2002.

[302] K. M. Kojima, S. Uchida, Y. Fudamoto, I.M. Gat, M.I. Larkin, Y.J. Uemura, and G.M. Luke. *Physica B*, 326:316, 2003.

[303] Hashini E. Mohottala, Barrett O. Wells, Joseph I. Budnick, William A. Hines, Christof Niedermayer, Linda Udby, Christian Bernhard, Arnold R. Moodenbaugh, and Fang-Cheng Chou. *Nature Physics*, 5:377, 2006.

[304] B. Nachumi, A. Keren, K. Kojima, M. Larkin, G.M. Luke, J. Merrin, O. Tchernyshov, Y.J. Uemura, N. Ichikawa, M. Goto, and S. Uchida. *Phys. Rev. Lett.*, 77:5421, 1996.

[305] S.H. Pan, E.W. Hudson, K.M. Lang, H. Eisaki, S. Uchida, and J.C. Davis. *Nature*, 403:746, 2000.

[306] H. Alloul, P. Mendels, H. Casalta, J.F. Marucco, and J. Arabski. *Phys. Rev. Lett.*, 67:3140, 1991.

[307] R. E. Walstedt, R.F. Bell, L.F. Schneemeyer, J.V. Waszczak, W.W. Warren Jr., R. Dupree, and A. Gencten. *Phys. Rev. B*, 48:10646, 1993.

[308] A. V. Mahajan, H. Alloul, G. Collin, and J.F. Marucco. *Phys. Rev. Lett.*, 72:3100, 1994.

[309] G. V. M. Williams, J.L. Tallon, and R. Meinhold. *Phys. Rev. B*, 52:7034, 1995.

[310] G. V. M. Williams and J. L. Tallon. *Phys. Rev. B*, 57:10984, 1998.

[311] J. Bobroff, W.A. MacFarlane, H. Alloul, P. Mendels, N. Blanchard, G. Collin, and J.-F. Marucco. *Phys. Rev. Lett.*, 83:4381, 1999.

[312] M.-H. Julien, T. Feher, M. Horvatic, C. Berthier, O.N. Bakharev, P. Segransan, G. Collin, and J.-F. Marucco. *Phys. Rev. Lett.*, 84:3422, 2000.

[313] S. Ouazi, J. Bobroff, H. Alloul, and W.A. MacFarlane. *Phys. Rev. B*, 70:104515, 2004.

[314] S. Ouazi, J. Bobroff, H. Alloul, M. Le Tacon, N. Blanchard, G. Collin, M.H. Julien, M. Horvatic, and C. Berthier. *Phys. Rev. Lett.*, 96:127005, 2006.

[315] D. Poilblanc, D.J. Scalipino, and W. Hanke. *Phys. Rev. Lett.*, 72:884, 1994.

[316] D. Poilblanc, D.J. Scalipino, and W. Hanke. *Phys. Rev. B*, 50:13020, 1994.

[317] Noato Nagaosa and Tai-Kai Ng. *Phys. Rev. B*, 51:15588, 1995.

[318] W. Ziegler, D. Poilblanc, R. Preuss, W. Hanke, and D.J. Scalapino. *Phys. Rev. B*, 53:8704, 1996.

[319] Noato Nagaosa and Patrick A. Lee. *Phys. Rev. Lett.*, 79:3755, 1997.

[320] G. Khaliullin, S. Krivenko, R. Kilian, and P. Fulde. *Physica C*, 282-287:1749–1750, 1997.

[321] A.W. Sandvik, E. Dagotto, and D.J. Scalapino. *Phys. Rev. B*, 56:11701, 1997.

[322] N. Bulut. *Phys. Rev. B*, 61:9051, 2000.

[323] Yoji Ohashi. *J. Phys. Soc. Japan*, 70:2054–2060, 2001.

[324] Hiroki Tsuchiura, Yukio Tanaka, Masao Ogata, and Satoshi Kashiwaya. *Phys. Rev. B*, 64:140501, 2001.

[325] P. Prelovsek and I. Sega. *Phys. Rev. Lett.*, 93:207202, 2004.

[326] Hiroshi Kontani and Massanori Ohno. *Phys. Rev. B*, 74:014406, 2006.

[327] M. Gabay, E. Semel, P.J. Hirschfeld, and W. Chen. *Phys. Rev. B*, 77:165110, 2007.

[328] G.J. MacDougall, J. Rodriguez, C.R. Wiebe, G.M. Luke, A.T. Savici, P.L. Russo, Y.J. Uemura, S. Wakimoto, and R.J. Birgeneau. *Physica B*, 374-375:211, 2006.

[329] J.E. Sonier, M. Ilton, V. Pacradouni, C.V. Kaiser, S.A. Sabok-Sayr, Y. Ando, S. Komiya, W.N. Hardy, D.A. Bonn, R. Liang, and W.A. Atkinson. *arXiv:0801.3481*, 2008.

[330] F. Mila and T.M. Rice. *Physica C*, 157:561, 1989.

[331] R.J. Birgeneau, C. Stock, J.M. Tranquada, and K. Yamada. *J. Phys. Soc. Jap.*, 75:111003, 2006.

[332] H. Eskes and G.A Sawatzky. *Phys. Rev. Lett.*, 61:1415, 1988.

[333] H. Eskes and G.A. Sawatzky. *Phys. Rev. B*, 44:9656, 1991.

[334] A. Maignan, C. Martin, M. Huve, J. Provost, M. Hervieu, C. Michel, and B. Raveau. *Physica C*, 170:350, 1990.

[335] C. Martin, A. Maignan, Ph. Labbe, J. Chardon, J. Hejtmanek, and B. Raveau. *Chem. Mater.*, 7:1414, 1995.

[336] C.T. Chen, L.H. Tjeng, J. Kwo, H.L. Kao, P. Rudolf, F. Sette, and R.M. Fleming. *Phys. Rev. Lett.*, 68:2543, 1992.

[337] P. Srivastava, F. Studer, K.B. Garg, Ch. Gasser, H. Murray, and M. Pompa. *Phys. Rev. B*, 54:693, 1996.

[338] S. Wakimoto, K. Yamada, J.M. Tranquada, C.D. Frost, R.J. Birgeneau, and H. Zhang. *Phys. Rev. Lett.*, 98:247003, 2007.

[339] D.E. Cox, G. Shirane, S.M. Shapiro, G. Aeppli, Z. Fisk, J.L. Smith, J. Kjems, and H.R. Ott. *Phys. Rev. B*, 33:3614, 1986.

[340] D.A. Bonn, J.D. Garrett, and T. Timusk. *Phys. Rev. Lett.*, 61:1305, 1988.

[341] C. Verge and W.R. Datars. *J. Sci. Instriments*, 1:1239, 1968.

[342] A. Eiling and J.S. Schilling. *J. Phys. F:Metal Phys.*, 11:623, 1981.

[343] T. Inoue, K. Kindo, H. Okuni, K. Sugiyama, Y. Haga, E. Yamamoto, T.C. Kobayashi, Y. Uwatoko, and Y. Onuki. *Physica B*, 294-295:271, 2001.

[344] M.W. McElfresh, J.D. Thompson, J.O. Willis, M.B. Maple, T. Kohara, and M.S. Torikachvili. *Phys. Rev. B*, 35:43, 1987.